DESIGN, TESTING, AND PERFORMANCE OF A HYBRID MICRO VEHICLE - THE HOPPING ROTOCHUTE

A Thesis
Presented to
The Academic Faculty

by

Eric W. Beyer

In Partial Fulfillment
of the Requirements for the Degree
DOCTOR OF PHILOSOPHY in the
School of AEROSPACE ENGINEERING

Georgia Institute of Technology
AUGUST 2009

DESIGN, TESTING, AND PERFORMANCE OF A HYBRID MICRO VEHICLE - THE HOPPING ROTOCHUTE

Approved by:

Dr. Mark Costello, Advisor
School of Aerospace Engineering
Georgia Institute of Technology

Dr. Nathan Slegers
School of Mechanical and Aerospace Engineering
University of Alabama, Huntsville

Dr. Daniel Schrage
School of Aerospace Engineering
Georgia Institute of Technology

Dr. Stephen Wilkerson
Unmanned Vehicles Division (A)
Army Research Laboratory

Dr. Dimitri Mavris
School of Aerospace Engineering
Georgia Institute of Technology

Date Approved: April 28, 2009

To my Father, Mother, and Fiancé

ACKNOWLEDGEMENTS

I would like to express my deepest gratitude and appreciation to my advisor, Dr. Mark Costello, for his advice, guidance, and support throughout the last several years. He has created an excellent environment for research which challenges his students while increasing their knowledge in many different branches of the engineering field. I feel privileged to have worked with Dr. Costello whose ability and willingness to explain complex problems in an organized and constructive manner is truly exceptional. His patience and constant availability to answer my numerous questions are also greatly appreciated. I would like to thank the members of my examining committee, Dr. Daniel Schrage, Dr. Dimitri Mavris, Dr. Nathan Slegers, and Dr. Stephen (Drew) Wilkerson, for their patience and time during the course of this accomplishment. I am indebted to Dr. Schrage for expanding my knowledge of rotorcraft design and his unfailing support on this thesis topic. I would like to thank Dr. Mavris for all his useful suggestions and comments. I thank Dr. Slegers of the University of Alabama, Huntsville for all the advice and help over the years. I am grateful to Dr. Wilkerson of the Army Research Laboratory for his support on this project as well as others.

I am indebted to the mechanical specialists in the AE machine shop, Scott Elliot and Scott Moseley, for all their help during the fabrication process. The numerous conversations we had about machining procedures and life are appreciated. I am grateful to Adam Broughton for assisting me in the UAV Procurement Laboratory, lending me equipment, and providing useful suggestions. I thank the students in the "Costello Research Group" for all the engaging discussions and the help with this project, including

Michael Abraham, Lois Fairfax, Kyle French, Ryan Letniak, Emily Leylek, Vasu Manivannan, Jessica Newman, Jonathan Rogers, Jenna Stahl, Aaron Webb, James Wright, and Sam Zarovy. It has been a pleasure to work with Ryan Letniak over the years, whose motivational talks have kept me going throughout my graduate studies. I am thankful to Jonathan Rogers for all the interesting conversations, both on and off campus, and the help during this process. I thank Michael Abraham for helping me during flight testing and providing valuable suggestions. I also would like to thank Amit Lalloobhai for his willingness to help me when I needed "three arms" during the video-taping and experimental testing procedures.

My fiancé, Alicia, has stood by me through good times and bad. She has listened to my many technical issues, without knowing anything about the subject, and has always somehow helped me form a solution. Her constant love, patience, and support has allowed me to complete this work. I am grateful to my immediate and extended family who have encouraged and supported me throughout my academic career. I am especially thankful to my father and mother who, from a very early age, have instilled in me the qualities that define me. Their unconditional love and support throughout my life has allowed me to reach this point. To all those who I have inadvertently left out, I apologize for it is impossible to remember all.

TABLE OF CONTENTS

Page

ACKNOWLEDGEMENTS iv

LIST OF TABLES ix

LIST OF FIGURES x

LIST OF SYMBOLS xv

LIST OF ABBREVIATIONS xviii

SUMMARY xix

CHAPTER

1 INTRODUCTION 1

1.1 Objectives 1

1.2 Robot Locomotion Overview 2

1.3 Existing Hopper Designs 5

1.3.1 JPL Hoppers 5

1.3.2 Jumping Mini-Whegs™ 7

1.3.3 Scout 8

1.3.4 Jollbot 9

1.3.5 Glumper 10

1.3.6 Deformable Hoppers 11

1.3.7 Sandia Hoppers 12

1.3.8 Airhoppers 13

1.3.9 Pendulum-Type Hopper 14

1.4 Design Drivers and Rotor Locomotion Selection 16

1.5 Specific System Requirements 18

1.6 Hopping Robot Concept Selection 19
1.7 Contributions of the Thesis 20
1.8 Thesis Outline 20
2 DESIGN OF THE HOPPING ROTOCHUTE 22
2.1 Initial Hopping Rotochute Designs 22
2.2 Hopping Rotochute Components 27
2.2.1 Propulsion System 27
2.2.2 Electronics 31
2.2.3 Main Body 35
2.3 Final Design and Layout 42
3 TESTING OF THE HOPPING ROTOCHUTE PROTOTYPE 46
3.1 Rotor System Aerodynamic Analysis 46
3.2 Flight Testing of the Hopping Rotochute Prototype 52
3.3 Discussion 59
4 HOPPING ROTOCHUTE DYNAMIC MODEL 61
4.1 Equations of Motion 62
4.2 Body Forces and Moments 64
4.3 Discussion 73
5 VALIDATION OF THE DYNAMIC MODEL 74
5.1 Motion Measurement System 74
5.2 Ground Contact Validation 78
5.3 Flight Dynamic Validation 85
6 FLIGHT PERFORMANCE OF THE HOPPING ROTOCHUTE 94
6.1 Example Trajectories 94
6.2 Flight Performance Trade Studies 102

6.3 Atmospheric Wind Trade Studies 117

6.4 Trajectory Shaping 119

7 CONCLUSIONS AND FUTURE WORK 123

7.1 Conclusions 123

7.2 Recommended Future Works 125

APPENDIX A: HOPPING ROTOCHUTE PROTOTYPE FABRICATION 129

APPENDIX B: HOPPING ROTOCHUTE COMPONENT DRAWINGS 132

REFERENCES 137

VITA 147

LIST OF TABLES

	Page
Table 1.1: Existing hopper design details	15
Table 1.2: Robot locomotion decision matrix	17
Table 2.1: Properties of pre-built micro helicopters	29
Table 2.2: Properties of receivers	31
Table 2.3: Properties of electronic speed controllers	32
Table 2.4: Properties of servos	33
Table 2.5: Properties of batteries	35
Table 2.6: Cushion foam material properties	41
Table 2.7: Mass properties of components	45
Table 5.1: Material properties	80
Table 5.2: Aerodynamic properties	86
Table 6.1: Properties of system 1 and 2	95

LIST OF FIGURES

		Page
Figure 1.1:	First, second, and third generation JPL hoppers	7
Figure 1.2:	Jumping Mini-Whegs™	8
Figure 1.3:	Scout	9
Figure 1.4:	Jollbot	10
Figure 1.5:	Glumper	11
Figure 1.6:	Deformable hoppers	12
Figure 1.7:	Sandia hoppers	13
Figure 1.8:	Airhoppers	14
Figure 2.1:	First generation Hopping Rotochute conceptual design	23
Figure 2.2:	Second generation Hopping Rotochute conceptual design	24
Figure 2.3:	Third generation Hopping Rotochute conceptual design	26
Figure 2.4:	Fourth generation Hopping Rotochute conceptual design	26
Figure 2.5:	Bumble Bee, Leopard, and Reflex micro helicopters	28
Figure 2.6:	Modified Reflex rotor system and transmission	30
Figure 2.7:	Schematic of transmission	30
Figure 2.8:	CIRRUS Micro Joule, CIRRUS MRX-4, and HITEC Micro 05S receivers	31
Figure 2.9:	CIRRUS Micro Joule S5A1, CIRRUS Micro Joule S5A2, and Electrifly C-7 Nano electronic speed controllers	32
Figure 2.10:	CIRRUS CS101/STD Micro, HITEC HS-50 Feather, and HITEC HS-45HB Premium Feather servos	33
Figure 2.11:	Apache 250 mAh, Electrifly 300 mAh, and Thunder Power 400 mAh batteries	34
Figure 2.12:	Hopping Rotochute prototype main body	36

Figure 2.13: Foam cushion force versus deflection 38

Figure 2.14: Drop test stand and model of drop test stand 40

Figure 2.15: Altitude versus time associated with drop test stand 41

Figure 2.16: Hopping Rotochute prototype 43

Figure 2.17: Hopping Rotochute prototype layout 44

Figure 3.1: Rotor test stand 47

Figure 3.2: Rotor thrust versus rotor speed 48

Figure 3.3: Current versus rotor speed 49

Figure 3.4: Potential versus rotor speed 49

Figure 3.5: Power versus rotor speed 50

Figure 3.6: Altitude versus cross range versus range 53

Figure 3.7: Cross range versus range 54

Figure 3.8: Range versus time 54

Figure 3.9: Cross range versus time 55

Figure 3.10: Altitude versus time 55

Figure 3.11: Pitch angle versus time 56

Figure 3.12: Rotor speed versus time 57

Figure 3.13: Thrust versus time 57

Figure 3.14: Current versus time 58

Figure 3.15: Power versus time 58

Figure 4.1: Hopping Rotochute schematic 62

Figure 4.2: Example arrangement of body vertices and ground face for the soft contact model 68

Figure 4.3: Spring and damper schematic for the soft contact model 69

Figure 5.1: Indoor Flight Facility with VICON motion capture system 75

Figure 5.2: Hopping Rotochute prototype with VICON markers 76

Figure 5.3: Polyurethane and carpet spring constants versus vertex spacing 79
Figure 5.4: Altitude versus time associated with drop test stand 81
Figure 5.5: Friction test setup 82
Figure 5.6: Drop test altitude versus time 83
Figure 5.7: Drop test cross range versus range 84
Figure 5.8: Drop test roll angle versus time 84
Figure 5.9: Drop test pitch angle versus time 85
Figure 5.10: Flight test altitude versus cross range versus range 88
Figure 5.11: Flight test range versus time 89
Figure 5.12: Flight test cross range versus time 89
Figure 5.13: Flight test altitude versus time 90
Figure 5.14: Flight test pitch angle versus time 90
Figure 5.15: Flight test forward velocity versus time 91
Figure 5.16: Flight test vertical velocity versus time 91
Figure 5.17: Flight test rotor speed versus time 92
Figure 5.18: Flight test thrust versus time 92
Figure 5.19: Flight test power versus time 93
Figure 6.1: Altitude versus cross range versus range 97
Figure 6.2: Range versus time 98
Figure 6.3: Altitude versus time 98
Figure 6.4: Pitch angle versus time 99
Figure 6.5: Forward velocity versus time 99
Figure 6.6: Vertical velocity versus time 100
Figure 6.7: Rotor speed versus time 100
Figure 6.8: Thrust versus time 101

Figure 6.9: Power versus time 101

Figure 6.10: Current versus time 102

Figure 6.11: Rotor speed profile 103

Figure 6.12: Single hop range versus internal mass offset versus rotor speed using 250 mAh battery 105

Figure 6.13: Launch pitch angle versus internal mass offset using 250 mAh battery 106

Figure 6.14: Maximum altitude versus internal mass offset versus rotor speed using 250 mAh battery 106

Figure 6.15: Number of hops versus rotor speed using 250 mAh battery 107

Figure 6.16: Total range versus internal mass offset versus rotor speed using 250 mAh battery 107

Figure 6.17: Number of hops versus rotor speed using 250, 300, and 480 mAh battery 109

Figure 6.18: Total range versus internal mass offset versus rotor speed using 300 mAh battery 109

Figure 6.19: Maximum altitude versus internal mass offset versus rotor speed using 300 mAh battery 110

Figure 6.20: Total range versus internal mass offset versus rotor speed using 480 mAh battery 111

Figure 6.21: Maximum altitude versus internal mass offset versus rotor speed using 480 mAh battery 111

Figure 6.22: Total range versus internal mass offset versus rotor speed using 250 mAh battery 113

Figure 6.23: Maximum altitude versus internal mass offset versus rotor speed using 250 mAh battery 113

Figure 6.24: Number of hops versus pulse width versus rotor speed using 250 mAh battery 115

Figure 6.25: Total range versus pulse width versus rotor speed using 250 mAh battery 115

Figure 6.26: Maximum altitude versus pulse width versus rotor speed using 250 mAh battery 116

Figure 6.27: Total range versus maximum altitude with 2 s pulse width using 250 mAh battery 117

Figure 6.28: Range versus wind speed 118

Figure 6.29: Wind dispersion 119

Figure 6.30: Altitude versus cross range versus range during trajectory shaping 121

Figure 6.31: Rotor speed versus time during trajectory shaping 121

Figure 6.32: Internal mass angles versus time during trajectory shaping 122

Figure B.1: Main body core 132

Figure B.2: Mounting bracket plate 133

Figure B.3: Mounting bracket pin 133

Figure B.4: Star piece 134

Figure B.5: Lower shaft extension 134

Figure B.6: Transmission mount 135

Figure B.7: Internal mass bar 136

Figure B.8: Internal mass housing 136

LIST OF SYMBOLS

c_{1n}, c_{1t}	normal and tangential damping coefficients associated with body vertices
c_{2n}, c_{2t}	normal and tangential damping coefficients associated with ground face
C_D	aerodynamic drag coefficient
C_{lp}, C_{mq}, C_{nr}	aerodynamic damping moment coefficients in body reference frame
C_P	coefficient of power
C_T	coefficient of thrust
d_{IM}	internal mass offset distance
D	aerodynamic reference diameter
$\vec{F}_n, \vec{F}_t$	normal and tangential contact force vectors
g	acceleration of gravity
I	inertia matrix of Hopping Rotochute about mass center
k_{1n}, k_{1t}	normal and tangential spring constants associated with body vertices
k_{2n}, k_{2t}	normal and tangential spring constants associated with ground face
L, M, N	applied moment components about mass center in body reference frame
m	mass of Hopping Rotochute
$\vec{n}$	ground face normal
p, q, r	components of angular velocity vector in body reference frame
$\mathbf{R}_{A \to B}$	skew-symmetric matrix representation of position vector from a generic point A to another point B in body reference frame
$\vec{s}_{1n}, \vec{s}_{1t}$	normal and tangential spring distance vectors associated with body vertices

$\vec{s}_{2n}, \vec{s}_{2t}$	normal and tangential spring distance vectors associated with ground face
S	aerodynamic reference area
$SL_{A\to B}, BL_{A\to B}, WL_{A\to B}$	components of position vector from a generic point A to another point B in body reference frame along the stationline, buttline, and waterline
$\mathbf{T}_{BI}$	transformation matrix from inertial reference frame to body reference frame
$\mathbf{T}_{BR}$	transformation matrix from rotor reference frame to body reference frame
$\mathbf{T}_{IB}$	transformation matrix from body reference frame to inertial reference frame
$\mathbf{T}_{PB}$	transformation matrix from body reference frame to internal mass reference
T	rotor thrust
$\vec{u}$	absolute velocity of the contact point
u, v, w	components of mass center velocity vector in body reference frame
V_{MW}	mean atmospheric wind speed
$\vec{w}$	absolute velocity of the surface elements
x, y, z	components of mass center position vector in inertial reference frame
X, Y, Z	applied force components in body reference frame
ζ	damping ratio
θ_{IM}, ψ_{IM}	internal mass orientation parameters
μ	coefficient of friction
ρ	density of air
τ	rotor lag time constant

ϕ, θ, ψ	Euler roll, pitch, and yaw angles of Hopping Rotochute
ϕ_F, θ_F	filtered Euler roll and pitch angles
ϕ_R, θ_R	Euler roll and pitch angles of rotor tip path plane
ψ_{MW}	mean atmospheric wind azimuth angle
ω_n	natural frequency

LIST OF ABBREVIATIONS

BA	body aerodynamics
C	contact or contact point
CG	center of gravity
CP	center of pressure
DL	disc loading
EPP	expanded polypropylene
EPS	expanded polystyrene
ESC	electronic speed controller
FM	figure of merit
IFF	Indoor Flight Facility
IM	internal mass
MAV	micro air vehicle
MW	mean atmospheric wind
NC	number of contact points
RA	rotor aerodynamics
Rx	receiver
SE	surface element
SMA	shape memory alloy
SR	slow-recovery
W	weight

SUMMARY

The Hopping Rotochute is a new hybrid micro vehicle that has been developed to robustly explore environments with rough terrain while minimizing energy consumption over long periods of time. The device consists of a small coaxial rotor system housed inside a lightweight cage. The vehicle traverses an area by intermittently powering a small electric motor which drives the rotor system, allowing the vehicle to hop over obstacles of various shapes and sizes. A movable internal mass controls the direction of travel while the egg-like exterior shape and low mass center allows the vehicle to passively reorient itself to an upright attitude when in contact with the ground.

This dissertation presents the design, fabrication, and testing of a radio-controlled Hopping Rotochute prototype as well as an analytical study of the flight performance of the device. The conceptual design iterations are first outlined which were driven by the mission and system requirements assigned to the vehicle. The aerodynamic, mechanical, and electrical design of a prototype is then described, based on the final conceptual design, with particular emphasis on the fundamental trades that must be negotiated for this type of hopping vehicle. The fabrication and testing of this prototype is detailed as well as experimental results obtained from a motion capture system. Basic flight performance of the prototype are reported which demonstrates that the Hopping Rotochute satisfies all appointed system requirements.

A dynamic model of the Hopping Rotochute is also developed in this thesis and employed to predict the flight performance of the vehicle. The dynamic model includes aerodynamic loads from the body and rotor system as well as a soft contact model to

estimate the forces and moments during ground contact. The experimental methods used to estimate the dynamic model parameters are described while comparisons between measured and simulated motion are presented. Good correlation between these motions is shown to validate the dynamic model. Using the validated dynamic model, simulations were performed to better understand the dynamics of the device. In addition, key parameters such as system weight, rotor speed, internal mass weight and location, as well as battery capacity are varied to explore and optimize flight performance characteristics such as single hop height and range, number of hops, and total achievable range. The sensitivity of the Hopping Rotochute to atmospheric winds is also investigated as is the ability of the device to perform trajectory shaping.

CHAPTER 1

INTRODUCTION

Ground and air robots are playing an increasingly important role in many military and civilian systems. An important mission to be tackled by future micro robots is exploring small interior and exterior spaces such as caves, the inside of damaged buildings, and the exterior perimeter of buildings in cluttered urban settings. These environments are commonly characterized by very uneven terrain, highly variable walls, openings, and obstacles. In order to be successful in such rugged environments, the vehicle must be able to robustly traverse the rough terrain in a reliable manner. Besides being mission capable in these difficult environments, future robots will require operations over extended periods of time without being detected. This allows the robot and/or the machine's user to gather as much data as possible during surveillance or reconnaissance missions.

1.1 Objectives

The objective of this thesis was to design and develop a micro robot which can satisfy the mission requirements specified above, namely:

1. The ability to robustly negotiate through and/or over rugged terrain
2. The ability to operate over extended periods of time without being detected

In support of this design, a new hybrid micro robot was invented and a radio-controlled prototype was constructed and subsequently flight tested as a proof-of-concept. Furthermore, a combined flight and ground simulation model was developed to predict and optimize the flight performance of the vehicle.

1.2 Robot Locomotion Overview

Many different small and micro robot configurations have been designed, built, tested, and fielded throughout the last few decades including ground, air, and hopping vehicles. These robots, based on different locomotion techniques, possess certain strengths and weaknesses when considering the appointed mission requirements. An overview of these vehicle configurations is given below as well as a discussion of their associated advantages and disadvantages.

The most prevalent type of robot locomotion is based on a wheeled design. Many different types of ground vehicles utilizing wheels have been developed including the four-wheeled MARCbot and the two-wheeled Recon Scout [1, 2]. Although these robots are very efficient at traversing relatively smooth surfaces, they encounter great difficulties when trying to surmount obstacles greater than one-half the diameter of their wheels. Some wheeled robots, such as the Sojourner and Shrimp space rovers, have overcome this limitation by employing bogey systems. These six-wheeled devices are able to climb over obstacles 1.5 and 2 times their wheel diameter respectively [3, 4]. While these vehicles are able to surmount taller obstacles than traditional wheeled robots, they are still limited to overcoming obstruction much less than their overall body length and rely upon many power consuming actuators and complicated suspension systems. Robots of the wheeled type also typically exhibit good maneuverability characteristics allowing them to drive around and avoid challenging terrain. Unfortunately this progress is completely halted when deep gullies, high walls, or other steep terrain are encountered.

Ground vehicles based on a track-type design have also been developed to overcome rough terrain. Two examples are the PackBot and the TALON produced by the iRobot Corporation and Foster-Miller Inc., respectively. The PackBot is equipped with two main treads used for locomotion and two articulated flippers used to climb over obstacles [5]. The vehicle can be driven to speeds up to 2 m/s continuously for 8 hours and can climb up, down, and across surfaces inclined up to 60 deg [6]. The TALON also

consists of two tracks, can travel at speeds up to 2.3 m/s continuously for 4.5 hours, and can maneuver over stairs inclined at 43 deg and side slopes of 45 deg [7]. Although these vehicles can typically outperform similarly sized wheeled robots when traversing rugged terrain, they still possess limitations associated with the maximum obstacle height they can surmount. This maximum height is dependent on several factors including the size of the tracks, the position of the vehicle's mass center, and the friction characteristics between the tread of the track and the terrain. In general, a tracked robot is unlikely to pass over obstacles that are taller than half the vehicle's length unless the mass center is positioned sufficiently far from its geometric center.

Robots utilizing legged locomotion are also better suited for rugged terrain traversal than wheeled vehicles. While these ground vehicles can potentially clamber over very difficult terrain, they are mechanically complex and require numerous joints, actuators, and linkages. In addition, the control of the robot's multiple degrees of freedom requires great computational overhead and power consumption. One such small quadruped robot developed by Boston Dynamics, called LittleDog, is being used by a number of institutions to test control algorithms and has an endurance of 30 min [8, 9]. Some unique "legged" vehicles have been developed which require fewer actuators, such as the RHex and Whegs™ which combine the simplicity of wheels with the mobility and adaptability of legs [10 – 12]. Although robots based on a legged design have demonstrated the ability to overcome rugged terrain, it is improbable that they will be able to traverse obstacles taller than double the length of their legs.

The most effective method of traveling over rugged environments is to simply fly above it. Micro air vehicles (MAVs) based on fixed-, rotary-, and flapping-wing designs have been developed which completely avoid obstructions on the ground during the entire mission. The Black Widow developed by AeroVironment, is one such MAV based on a fixed-wing design which is palm-sized, flies at forward speeds of 14 m/s, and has an endurance of around 30 min [13, 14]. The Class I UAV from Honeywell is based on a

ducted fan configuration, is able to hover and fly at speeds of 22.4 m/s, and has an endurance of 50 min [15]. The smallest known autonomous helicopter, the Hornet Micro Helicopter from Adaptive Flight, has an endurance of about 20 min and a typical operating range of 1-3 km [16]. The Microbat developed by AeroVironment, the California Institute of Technology, and the University of California, Los Angeles was the first electrically powered palm-sized ornithopter which flew for about 1 min at a flight speed of 6 m/s while flapping its wings at 20 Hz [17]. Although these vehicles are not hindered by obstacle-ridden ground terrain, they are energetically expensive due to the fact that they must remain airborne during the majority of the mission to avoid the complexities of landing and taking-off again. In addition, complex control and obstacle avoidance algorithms must be implemented to maneuver the vehicles through confined spaces with overhead obstacles without incidence. Both these facts, limit the power-source life and hence the endurance of these aircraft. In addition, if the vehicle's wing contacts a wall or some other obstruction, the aircraft will most likely fall to the ground, unable to complete the mission.

To cope with the limitations of ground and air vehicle in traversing rugged terrain, researchers have developed hopping machines which have the potential to jump over obstacles much greater than their own size. These hopping robots are based on one of two different jumping strategies: "continuous" and "pause-and-leap". Continuous hopping mimics the motion of a kangaroo traveling across a plain, where energy is recovered during the landing of the device and subsequently used in the next jump. Continuous hopping requires a high level of sophistication in control for dynamic stability and active balancing which increases the power consumption and computational overhead. Pause-and-leap hopping motion, on the other hand, is characterized by a hop, a period of rest and reorientation, before another jump is executed. This jumping strategy, mimicking the motion of a frog, allows for minimal energy consumption during the "resting" period and the ability to navigate over difficult terrain assuming the vehicle can

survive the landing. In principle, hopping robots based on a pause-and-leap strategy have the potential to jump over obstacles much greater than themselves with simple construction and directional control.

1.3 Existing Hopper Designs

Many different types of pause-and-leap hoppers exist which utilize different energy storage methods including coil-spring, bending-spring, fluid-powered, and momentum-based designs. In this section, a number of pause-and-leap hoppers are described and the capabilities of each are outlined latter in Table 1.1. It is important to note that many different types of continuously hopping robots also exist, but are excluded in this discussion because of the different design problems associated with the dynamic stability and active balancing of the devices [18 – 21].

1.3.1 JPL Hoppers

A series of small hopping robots were developed by the researchers at NASA Jet Propulsion Laboratories (JPL) and the California Institute of Technology [22]. As shown in Figure 1.1 a), the first generation robot incorporated a clear polycarbonate outer shell which protected the internal workings during ground impact. To hop, a simple linear spring is compressed using a motor driven ball screw and released which drives a "foot" into the ground. Using this jumping mechanism, the vehicle was able to hop a vertical distance of about 80 cm while achieving a horizontal distance between 30 and 60 cm. To control the direction of travel, the vehicle was tilted prior to launch using an off-axis rotating camera. The batteries and other heavy components were located at the bottom of the hopper to create a low mass center, allowing the vehicle to passively upright itself after ground impact. Experiments were conducted which demonstrated that the vehicle was about 20% efficient in converting energy stored in the spring to motion. In addition

to this inefficiency, the first generation design also exhibited inadequate steering and self-righting ability.

To address the drawbacks of the first generation hopper, an active steering and self-righting mechanism were incorporated into a second generation, shown in Figure 1.1 b), as well as a six-bar linkage and coil spring mechanism. When released, the force-displacement profile of this leg system results in a nonlinear spring profile that is generated by a linear spring. The release force gradually increases to a peak before rapidly decreasing which substantially reduces the likelihood of the vehicle prematurely lifting-off before all the energy is released. The six-bar linkage and spring mechanism is compressed using a motor driven power screw which allows the vehicle to fit within a 15 $\times$ 15 $\times$ 15 cm^3 space. The compressed assembly was mounted at roughly 50 deg from the horizontal plane of the foot to maximize the horizontal hopping distance during flight. A single motor drives all the subsystems of this device and allows the 1.3 kg vehicle to reach horizontal distance of about 2.3-3 m and vertical distances of about 1.2 m. The vehicle is pointed in the desired direction of travel by employing a steering mechanism while in its uncompressed state with the foot acting as a wheel to steer the vehicle. The vehicle self-rights itself using an active two stage self-righting process. Flaps first open up to allow the vehicle to roll onto its back and then a larger flap rotates to push the vehicle to an upright configuration. The second generation hopper exhibited a mechanical energy conversion efficiency of about 70% and lacked the ability to adjust the take-off angle and fine mobility.

A third generation vehicle, shown in Figure 1.1 c), was designed to address these shortcomings while retaining the six-bar linkage and spring leg mechanism being compressed by winding a cable on a capstan. A four-bar linkage was incorporated into this prototype which allowed for an adjustable takeoff angle of between 0 and 85 deg from the foot's horizontal plane. This mechanism also lowered/elevated powered wheels during the compressed state which were used to drive the vehicle on relatively smooth

terrain and to steer the robot to the desired hopping direction prior to launch. The vehicle was able to drive over flat carpet and could jump over rocks approximately 30 cm high under remote control, but was designed without a self-righting feature.

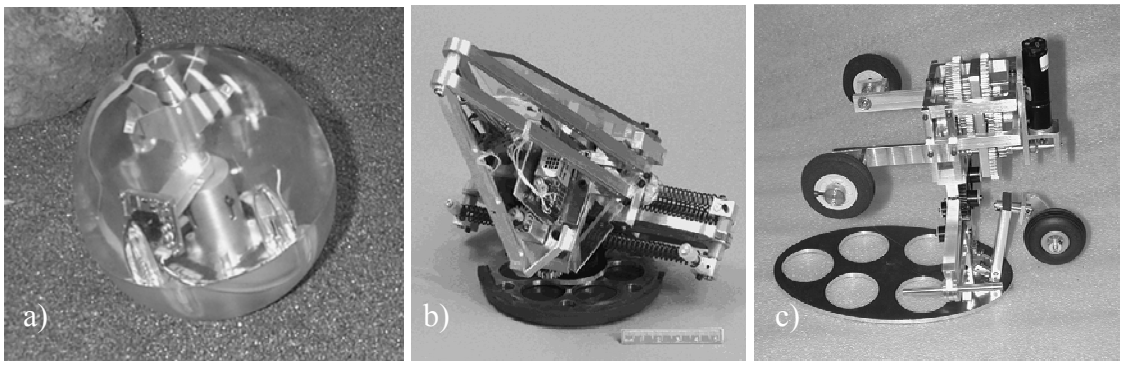

Figure 1.1: First, second, and third generation JPL hoppers (left to right)

1.3.2 Jumping Mini-Whegs™

Another jumping robot based on the coil spring design was developed by the Case Western Reserve University [23]. The original design of the Mini-Whegs™ did not jump at all, but was designed to "run" using three spoke wheel-like legs or "whegs" which "combine the speed and simplicity of a wheel with the high mobility of legs". The biologically inspired robot is propelled by a single motor which powers two axles, each having two 3.6 cm radius whegs. The radio controlled robot can run at speeds over 90 cm/s and was designed to negotiate difficult terrain. The vehicle had a weight of 146 g including batteries while being 9 cm long, 7 cm wide, and 2 cm thick. In order to navigate over larger obstacles, a version of the robot called Jumping Mini-Whegs™ was developed [24, 25]. As shown in Figure 1.2, this vehicle includes an additional jumping mechanism, but does not have the ability to be steered or radio controlled. Another transmission was added to the original single drive motor and transmission as well as a parallel four-bar linkage and coil spring which was attached to the frame with two axles.

As the motor runs, a slip-gear turns and rotates the four-bar mechanism while storing energy in the coil spring. Once released, the spiked lower bar or "foot" accelerates the robot forward and upward. Using this jumping mechanism, the vehicle was able to jump up to 22 cm high.

Figure 1.2: Jumping Mini-Whegs™

1.3.3 Scout

The Scout robots, developed by the University of Minnesota, were designed to work as a team forming a mobile sensor network and can be delivered to the target by a parent Ranger, launched, or thrown [26]. As shown in Figure 1.3, the remotely and/or autonomously controlled robot is cylindrical and is based on a two wheeled design. The robot has a length of 11 cm, a diameter of 4 cm, weighs 2 N, and can roll on smooth surfaces up to speeds of 0.31 m/s. In order to hop over obstacles, a steel spring foot is bent by a winch and cable which stores the required energy before a subsequent jump

[27]. The spring foot "jumping" mechanism allows the vehicle to jump as high as 30 cm with a strong spring and 10 cm with a weak spring. In quiescent mode, the vehicle has an endurance of 120 min, in full speed mode it can travel for 70 min, and it can jump up to 100 times when only jumping. The Scout includes simple sensory units including a color or black/white camera and can come in many different variations including actuating wheels, grappling hook, and infrared capabilities [28].

Figure 1.3: Scout

1.3.4 Jollbot

Jollbot, shown in Figure 1.4, is a biologically inspired jumping robot developed at the University of Bath which was designed to roll and hop [29]. This radio controlled robot consists of a main skeletal structure made from metal semicircular hoops attached at either end. The hoops act as springs when compressed together which provide the energy for jumping and also provide a spherical outer shape required for rolling. A

centrally mounted compression mechanism, consisting of a servo and gearboxes, pulls the upper and lower halves together to store energy within the outer structure. When this energy is released, the device jumps into the air. Directional control is achieved by adjusting the center of mass of the device prior to launch which leans the main jumping axis, allowing the Jollbot to make projectile type jumps. The 0.3 m diameter vehicle is able to raise its center of mass 0.22 m during a hop with a clearance of 0.184 m. Rolling is achieved by orienting the central axis parallel to the ground and adjusting the center of gravity of the sphere.

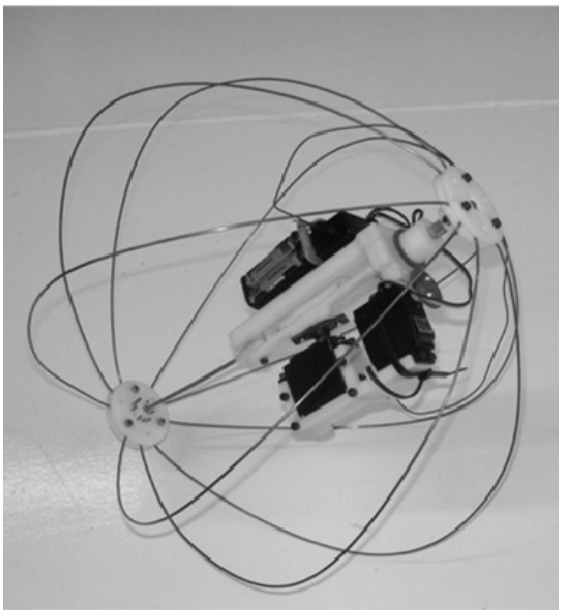

Figure 1.4: Jollbot

1.3.5 Glumper

Another robot developed at the University of Bath, called Glumper, was designed to jump into the air and then glide to simultaneously extend the range and to reduce the impact forces during ground impact [29]. As shown in Figure 1.5, Glumper consists of 4 long legs, each with a heavy duty torsional steel spring at their midpoint. In addition, a

triangular shaped membrane was mounted to each leg which acts as a gliding wing when airborne. The robot stores energy by compressing each of the torsional springs using a compression mechanism. When released, the legs extend and the 700 g robot jumps into the air, achieving a height of 1.6 m and a range of 2 m. Experimental results demonstrated that the wings actually reduce the total range of each jump as compared to the wingless system.

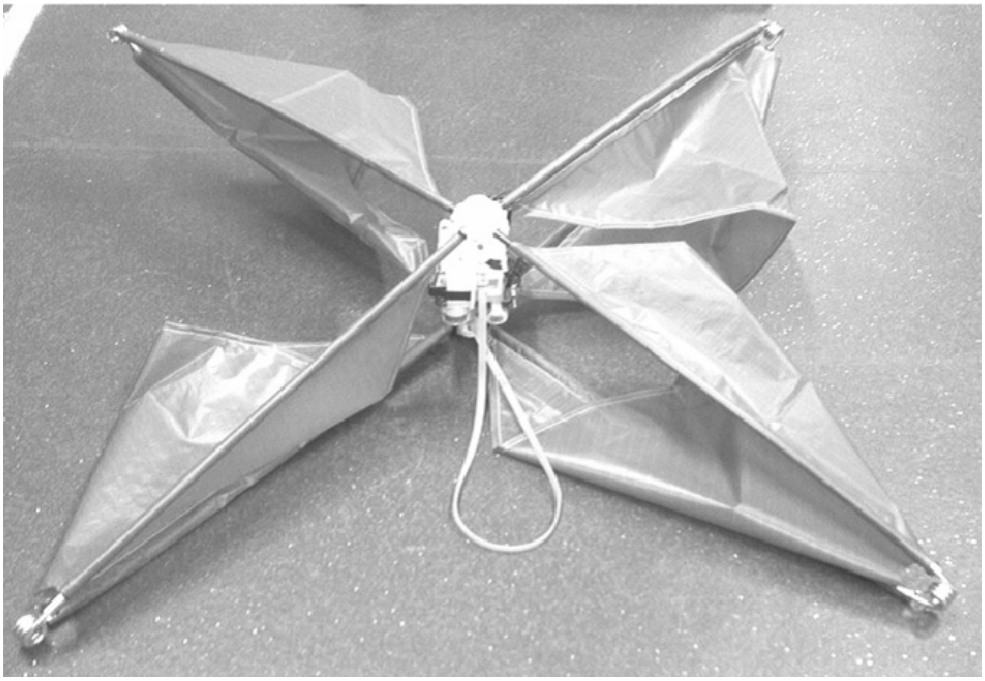

Figure 1.5: Glumper

1.3.6 Deformable Hoppers

A series of deformable robots were developed by the department of robotics at the Ritsumeikan University in Japan [30]. The tethered vehicles are able to roll and jump using shape memory alloy (SMA) spokes attached to an outer shell. When a voltage is applied to the SMA spokes, they contract causing the outer shell to deform. The self deformation of the robot can shift the center of mass, creating a moment that causes the

robot to roll along the ground. The deformation also allows elastic potential energy to be stored in the outer shell, which causes the robot to leap into the air when rapidly released. One of the prototypes, shown in Figure 1.6 a), consists of eight SMA coils and a spring steel shell having a diameter of 90 mm. The 3 g robot was able to hop 160 mm and 300 mm depending on the voltage pattern applied to the SMA spokes. A spherical shaped prototype was also developed consisting of three orthogonally intersecting spring metal circular shells as shown in Figure 1.6 b). The 90 mm diameter vehicle was able to crawl using 18 SMA coils and could jump by employing an additional 4 SMA coils attached to the inside of the circular shells. The 5 g vehicle was able to climb up slopes of 10 deg while jumping 70 mm and 180 mm depending on the applied voltage pattern.

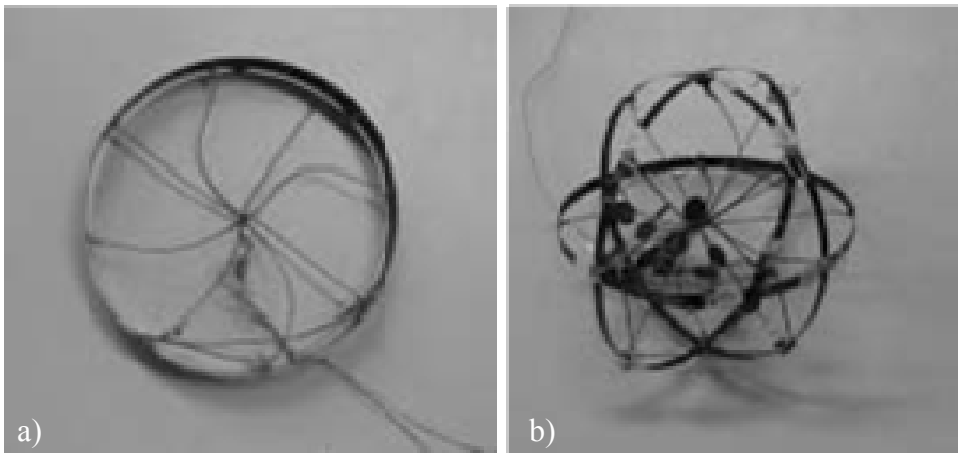

Figure 1.6: Deformable hoppers

1.3.7 Sandia Hoppers

Robot designers at the Sandia National Laboratories have developed two hoppers based on a fluid powered design [31, 32]. Each utilizes the combustion of liquid propane to drive a piston against the ground which hurls the vehicle into the air. The first hopper, shown in Figure 1.7 a), consists of a spherical plastic shell which protects the internal

workings and is about the size of a grapefruit. The piston-driving combustion chamber allows this vehicle to propel itself 1 m high and a couple of meters away from it starting point. Directional control is achieved by tilting the vehicle in the desired direction of travel prior to launch using a gimbal mechanism which rotates the offset-weighted internal components according to a built in compass. With a weight of 5 N including 20 g of fuel, the vehicle is able to hop thousands of times achieving a range of several kilometers before running out of fuel. The team has also developed a large 2.5 kg version of the robot, shown in Figure 1.7 b), capable of leaping 4 m high and 5 m away from its starting point.

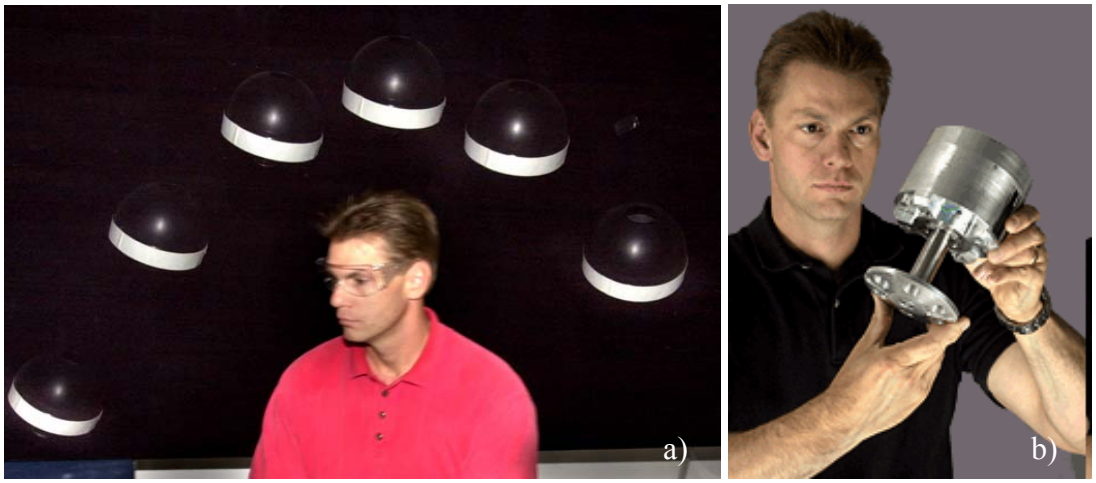

Figure 1.7: Sandia hoppers

1.3.8 Airhoppers

Another fluid-powered hopping robot, called the Airhopper, was developed by the Tokyo Institute of Technology. As shown in Figure 1.8 a), the vehicle consists of four widely-spaced legs attached to a tubular body. Each leg, based on a four-bar linkage design, is driven by a pair of pneumatic cylinders which can rapidly fill and extend [33]. The pneumatic cylinders allow the vehicle to walk and jump up to 0.82 m high [34]. The

pneumatic actuators are also used as dampers to absorb the shock impact during landing. To improve the mobility of the robot, active wheels have also been added at the end of the legs so the vehicle is able to drive on smooth surfaces. Using this added feature, the robot was able to roll on flat surfaces at speeds up to 1.8 m/s, could jump 0.65 m vertically, and 0.98 m horizontally [34].

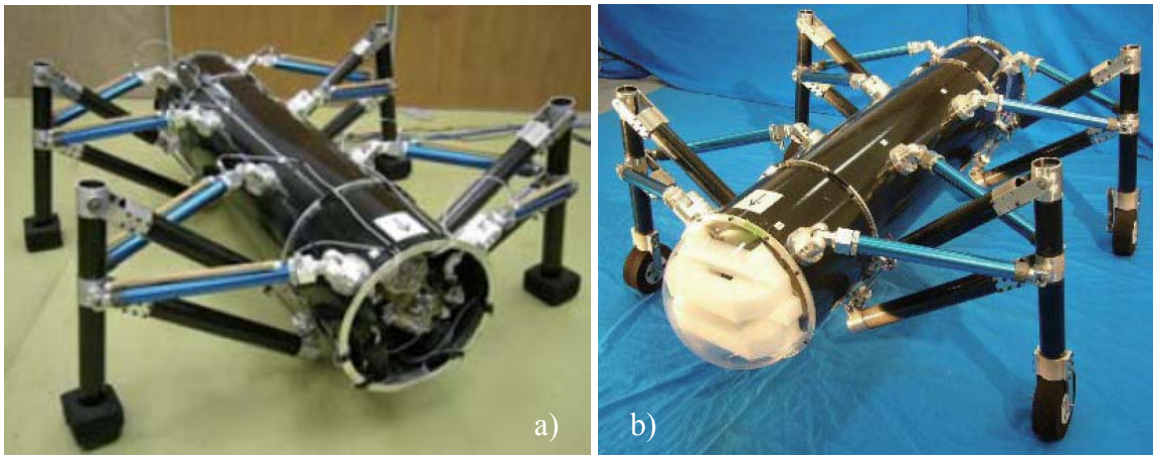

Figure 1.8: Airhoppers

1.3.9 Pendulum-Type Hopper

A team at the Kagoshima University in Japan has developed a hopping robot that uses the swinging of weighted arms to execute a jump, mimicking the way humans jump vertically [35]. This pendulum-type jumping machine consists of a "Y" shaped body with two servomotor actuated arms attached to it which have additional weight at their extremities. By swinging the arms in a harmonious manner, the centrifugal force of the arms exceeds the normal force against the ground causing the machine to make small leaps. The constructed prototype was able to jump on top of a 0.015 m high stair while achieving a height of 0.06 m.

Table 1.1: Existing hopper design details

Robot	Mass (kg)	Size $L \times W \times H$ (m)	Hop Height (m)	Hop Distance (m)	Energy Storage Method
JPL Hopper (2nd generation)	1.3	0.15 × 0.15 × 0.15	~1.2	2.3-3	Coil spring
Jumping Mini-Whegs™	0.146	0.16 × 0.08 × 0.08	0.22	N/A	Coil spring
Scout	0.2	0.11 × 0.08 × 0.04	0.30	0.25	Bending spring
Jollbot	0.465	0.3 × 0.3 × 0.3	0.22	0	Bending spring
Glumper	0.7	0.5 × 0.5 × 0.5	1.6	2	Bending spring
Deformable Hopper (cylindrical)	0.003	0.09 × 0.02 × 0.09	0.3	0	Bending spring
Deformable Hopper (spherical)	0.005	0.09 × 0.09 × 0.09	0.18	0	Bending spring
Sandia Hopper (V1)	0.5	0.13 × 0.13 × 0.13	~1	~2-3	Fluid powered
Sandia Hopper (V2)	2.5	0.1 × 0.1 × 0.2	4	5	Fluid powered
Airhopper	29.2	1.29 × 1.2 × 0.525	0.82	1	Fluid powered
Airhopper with wheels	34.6	1.29 × 1.2 × 0.6	0.65	0.98	Fluid powered
Pendulum-Type Hopper	0.98	0.2 × 0.2 × 0.24	~0.06	~0.09	Momentum

1.4 Design Drivers and Robot Locomotion Selection

In order to select a robot locomotion concept and to formulate a basis for design decisions, specific design drivers were identified to help evaluate different robot locomotion designs. The main sources which fed the design drivers were based on the designated mission requirements specified in Chapter 1.1. The specific design drivers include:

Traversability: The designated mission requires traversing rugged terrain. Therefore the vehicle should be able to travel over or through challenging environments.

Endurance: In order to gather/transmit as much information as possible to the operator, it is desirable that the vehicle minimize energy consumption over extended periods of time (capable of long endurance).

Survivability: The vehicle will be operating in complex, unpredictable environments and must be able to survive the inevitable collisions with obstacles.

Complexity: The mechanical complexity of the robot should be minimal to decrease the chance of failure while operating in complicated environments.

Detectability: To decrease the chance of being detected during surveillance or reconnaissance mission, the vehicle should be as small and quiet as possible.

Maneuverability: A maneuverable vehicle allows rugged terrain to be negotiated through and around.

Speed: Increased traversal speed minimizes the time required to get to the target area.

As described in Chapter 1.2, ground, air, and hopping vehicles possess certain advantages and disadvantages when considering missions involving the exploration of rugged terrain while minimizing energy consumption over extended periods of time. In order to evaluate how well these robot locomotion schemes satisfy the mission

requirements, a decision matrix (shown in Table 1.2) was formed based on the design drivers.

Table 1.2: Robot locomotion decision matrix

Weight	Criteria	Ground Vehicles	Air Vehicles	Hopping Vehicles
20 %	Traversability	1	5	3
20 %	Endurance	4	1	3
20 %	Survivability	4	1	5
15 %	Complexity	4	2	4
10 %	Detectability	4	2	4
10 %	Maneuverability	4	4	3
5 %	Speed	2	5	3
	Weighted Total	3.3	2.55	3.65

Criteria Values: 0 = Least Desirable, 5 = Most Desirable

As demonstrated by the robot locomotion decision matrix, ground vehicles are capable of long endurance and possess good survivability characteristics, but are limited by the size of the obstacle they can surmount. Micro air vehicles, on the other hand, can easily pass over rugged terrain, but have limited endurance and survivability characteristics. Hybrid vehicles offer a good mix of capability, demonstrating the ability to hop over difficult terrain to navigate and the ability to loiter for long periods of time with minimal energy consumption. In addition, hopping robots are designed for ground impact and hence have good survivability properties. Based on the observations made in Chapter 1.2 and the results of the robot locomotion decision matrix, a hopping robot is best suited to satisfy the designated mission requirements.

1.5 Specific System Requirements

With a hopping robot identified as the most promising robot locomotion concept, several specific system requirements were assigned to the vehicle which further drove the design of the device. These specific system requirements are listed below and are in addition to the typical engineering requirements, such as cost minimization and manufacturability.

1. The vehicle must be made as small, lightweight, and simple as possible using off-the-shelf components
2. The vehicle must possess some means of directional control
3. The vehicle must be able to passively upright itself no matter which orientation it lands
4. The vehicle must be able to carry small payload (at least 10 g) without it incurring any damage as the robot travels
5. The vehicle must be able to overcome at least 2 m high obstacles
6. The vehicle must be able to achieve a range of at least 200 m
7. The vehicle should posses the ability to shape a trajectory when airborne

The first requirement would allow the vehicle to negotiate through tight spaces which larger vehicles could not manage. In addition, being lightweight permits the vehicle to jump as high as possible with minimal energy consumption. This requirement also implies that mechanical complexities should be avoided which would increase the overall weight of the system. The use of off-the-shelf components would allow the vehicle to be easily reproduced allowing multiple proof-of-concepts to be tested. The second and third system requirements are extensions of the first mission requirement and are necessary in order for the vehicle to robustly traverse rugged terrain in a reliable manner. The third requirement also implies that an active self-righting mechanism should be avoided which would add mechanical complexity, weight, and consume power. The fourth system requirement is necessary in order for the vehicle to be useful; being

able to carry sensors into an area without damaging them. The fifth requirement would allow the vehicle to hop higher than most existing hopper designs, permitting the exploration of steeper, more rugged terrain. The sixth requirement stipulates that the vehicle travel a sufficient distance to and from the target while keeping the robot's operator out of harms way. The seventh requirement would allow the vehicle to navigate over and around objects with protrusions or overhangs while in the air.

1.6 Hopping Robot Concept Selection

As outlined in Chapter 1.3, many different hopping vehicle concepts exist which employ springs, fluid, or momentum to negotiate through rugged terrain. These existing hopping robot concepts fail to succeed in meeting all the specific system requirements outlined in Chapter 1.5. The majority of these hopping vehicles are unable to jump 2 m high and none have the ability to shape a trajectory when airborne.

In order to satisfy all the system requirements, a new type of hopping vehicle concept was proposed which conceptually had great potential. Rather than storing energy in a spring, using fluid to power the device, or swinging an arm to make the vehicle jump, a different approach was taken. The proposed hopping machine would be propelled upward by a motor driven rotor system powered in short bursts so the vehicle hops into the air before descending to the ground when unpowered. Using a low mass center and specially designed exterior, this hybrid air/ground vehicle would passively upright itself once on the ground in preparation for the next leap. Employing an off-axis movable internal mass, the direction of travel could be controlled by tilting the vehicle in the desired direction prior to launch and while the offset of the center of mass and thrust axis would provide a desirable pitching moment during flight. Using a pause-leap strategy in combination with the internal mass, the vehicle could potentially meander through rough

terrain and remain in a desirable area for a considerable amount of time while unpowered. In addition, using the movable internal mass as a steering mechanism when airborne is a viable solution for trajectory shaping [36-40].

The design and development of this new hybrid micro vehicle, called the Hopping Rotochute, is the focus of this thesis dissertation.

1.7 Contributions of the Thesis

This thesis substantially contributes to the micro robot literature with three main elements.

1. The creation of a new hybrid hopping vehicle called the Hopping Rotochute (provisional patent application submitted)
2. The development of a dynamic model of the Hopping Rotochute and the validation of this dynamic model using a motion capture system
3. Flight performance prediction and optimization of the Hopping Rotochute using the validated dynamic model

1.8 Thesis Outline

This thesis is composed of seven chapters. A brief description of each chapter follows:

Chapter 1: Introduction: A description of the problem statement, the previous work on the topic, and the contribution of the present work are presented.

Chapter 2: Design of the Hopping Rotochute: This chapter details the iterations involved in designing the Hopping Rotochute. The selected component properties are given and the final prototype is described.

Chapter 3: Testing of the Hopping Rotochute Prototype: The experimental setup and results of an aerodynamic analysis is presented. In addition, flight test results are reported which demonstrate the capabilities of the Hopping Rotochute prototype.

Chapter 4: Hopping Rotochute Dynamic Model: The mathematical model is derived and detailed as well as the derivation of the body forces and contact loads using a soft contact model.

Chapter 5: Validation of the Dynamic Model: This chapter describes how the developed dynamic model was verified. The motion capture system is described and used to predict unknown parameters of the dynamic model. The validation process and results are presented for both ground and flight dynamic validation.

Chapter 6: Flight Performance of the Hopping Rotochute: Using the validated dynamic model, trade studies are performed to better understand how key parameters influence the dynamics and flight performance of the vehicle. Additional trade study results demonstrate the wind sensitivity and trajectory shaping ability of the device.

Chapter 7: Conclusions and Future Work: Important conclusions are drawn from the presented results and lead to future work suggestions to improve the design of the Hopping Rotochute.

CHAPTER 2

DESIGN OF THE HOPPING ROTOCHUTE

This chapter is devoted to the design of the Hopping Rotochute hybrid micro vehicle. Through multiple conceptual design iterations and prototype builds/testing, the final Hopping Rotochute design was converged upon. Based on this final design, a prototype was constructed using off-the-shelf components. The properties of this Hopping Rotochute prototype are detailed at the end of the chapter and the fabrication of the device is outlined in Appendix A.

2.1 Initial Hopping Rotochute Designs

The initial conceptual design of the Hopping Rotochute is shown in Figure 2.1 a) which consists of a single main rotor mounted on top a body with canted fins to prevent the vehicle from spinning during powered flight. Although this anti-rotation is not explicitly stated in the system requirements, it was assumed that the vehicle would be much easier to radio control if the vehicle had minimal spin while airborne. The main body was initially designed with a pear shape to help reduce download (vertical drag) and the bottom was proposed to consist of some type of cushion material to help prevent damage to the electronics and/or payload during ground impact. The internal mass of this system was to be housed inside the main body and controlled by a motor driven power screw and servo as shown in Figure 2.1 b). This combination would allow the internal mass to move anywhere in the horizontal plane contained within the internal perimeter of the device.

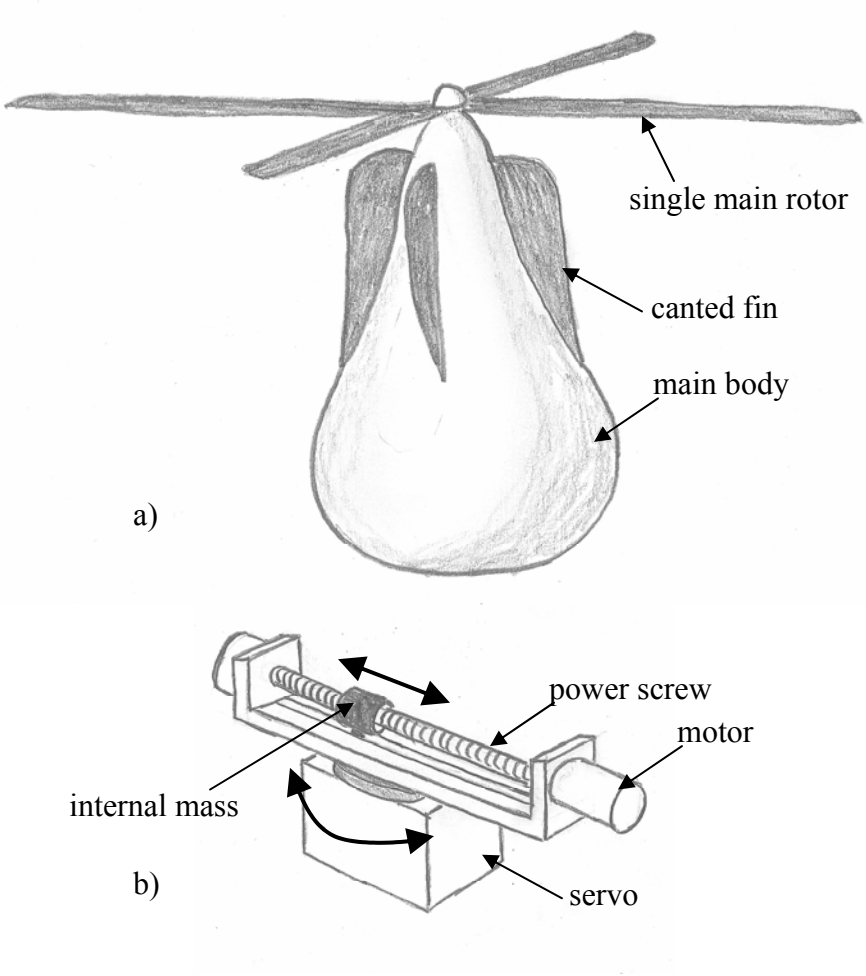

Figure 2.1: First generation Hopping Rotochute conceptual design

To prevent the main body from rotating during powered flight, canted fins were added to the first generation conceptual design in order to counteract the torque reaction from the shaft powered rotor. Although a fixed cant angle may work for a given inflow velocity, the speed of the inflow varies as the rotor system is activated. Hence, to cancel the torque during a hop, the canted fins would most likely need to be actively controlled which would require more actuators, complexity, and adds additional weight to the system. Based on this, a coaxial rotor system was proposed as shown in Figure 2.2 a).

The coaxial rotor system was also considered desirable due to the fact that rotor diameter would be reduced for a fixed sized vehicle resulting in a smaller sized device.

To further simplify the design and lower the weight, the internal mass was proposed to be controlled by a single servo as shown in Figure 2.2 b). Although this would prevent the vehicle from hovering, it would allow the vehicle to tilt in the desired direction of travel before executing a hop, thus producing a simple means for directional control.

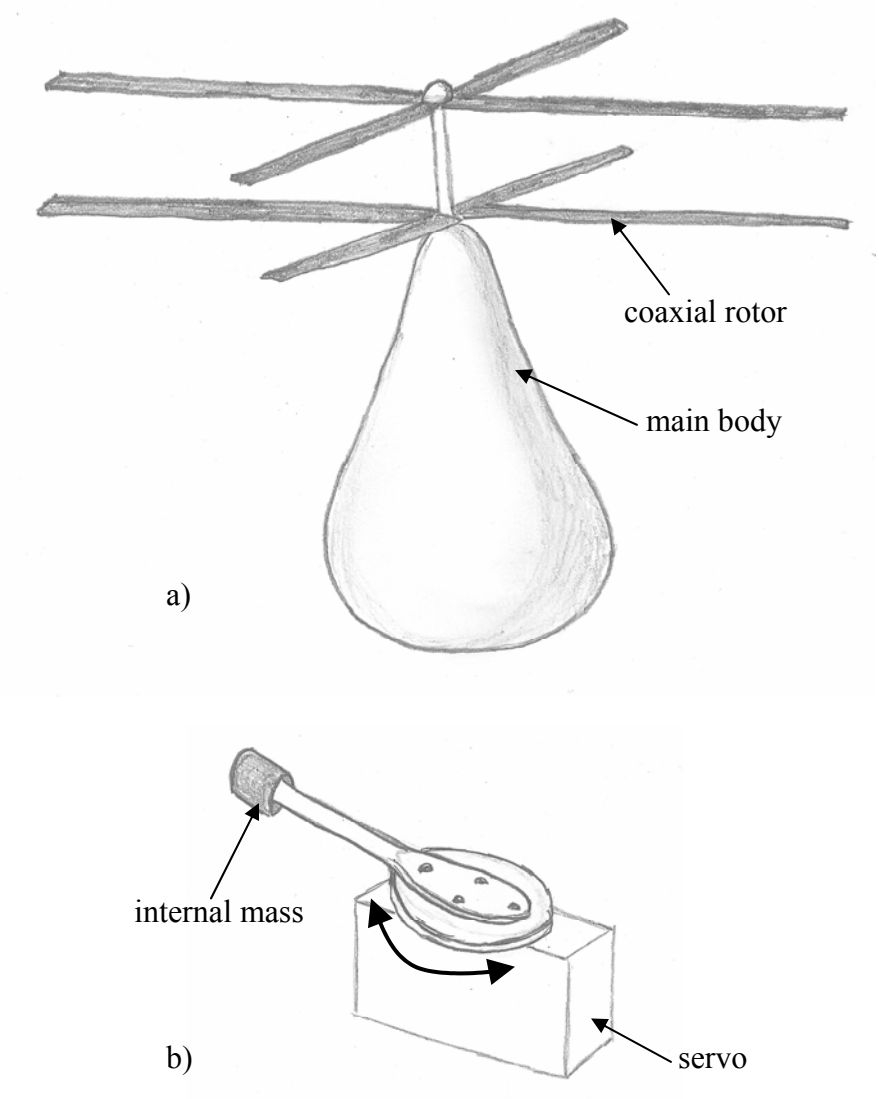

Figure 2.2: Second generation Hopping Rotochute conceptual design

Based on the second generation conceptual design, several different prototypes were constructed to test the proof-of-concept. Each prototype was powered using the propulsion system of the Air Hogs Reflex micro helicopter, incorporated an internal mass at a fixed location, but consisted of different body designs. The first prototype body was fabricated by cutting a 15.24 cm (6 in.) diameter Styrofoam ball in half and adhering carbon fiber to the outside surface. The carbon fiber skin provided much strength to the structure at the cost of additional weight. Other bodies were made out of 15.24 cm (6 in.) and 20.32 cm (8 in.) Styrofoam hemispheres with resin applied to the outer surface. The resin alone provided a stiff structure without adding additional weight with the carbon fiber cloth.

These prototypes were flown to assess the feasibility of the design. As expected, the lower weight systems were more responsive and hopped higher than their heavier counterparts with the fixed diameter rotor system. The smaller diameter based prototypes also performed better due to the decreased download (vertical drag) effects. Unfortunately during ground impact, the smaller diameter based prototypes would greatly pitch back and forth causing the rotor blades to contact the ground and typically break. This behavior was also demonstrated by the larger diameter based designs although the amplitude of the oscillations were not as severe.

Based on these observations, a third generation conceptual design was proposed as shown in Figure 2.3. The design consisted of a large diameter base to reduce the amplitude of oscillation during ground impact while the thickness of the base was made small to eliminate unnecessary material and to minimize weight. Another identically shaped top would be used to help reduce download. In addition, a roll cage would be incorporated to protect the rotor blades during ground and obstacle collisions. Although this proposed design would greatly eliminate the potential for rotor failure, the ability of the device to passively self-right itself has diminished. For example, if the device were to

land or rotate upside-down, the vehicle could potentially remain in this orientation and unable to complete the designated mission.

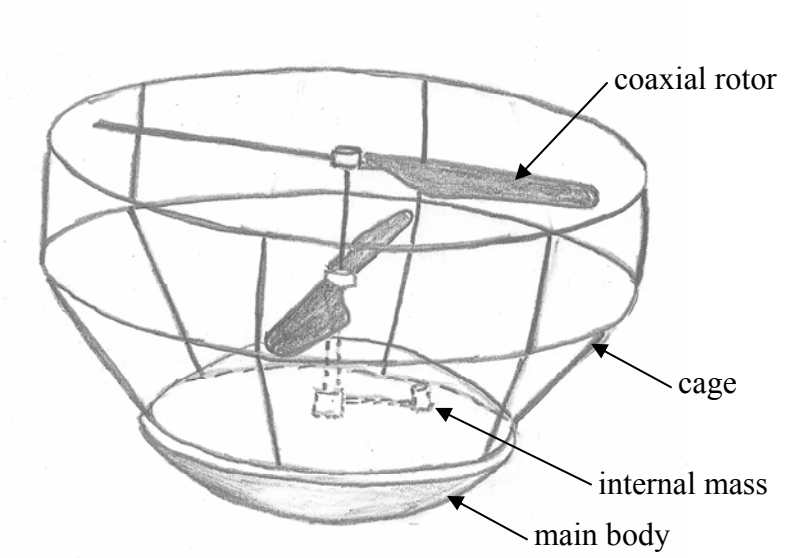

Figure 2.3: Third generation Hopping Rotochute conceptual design

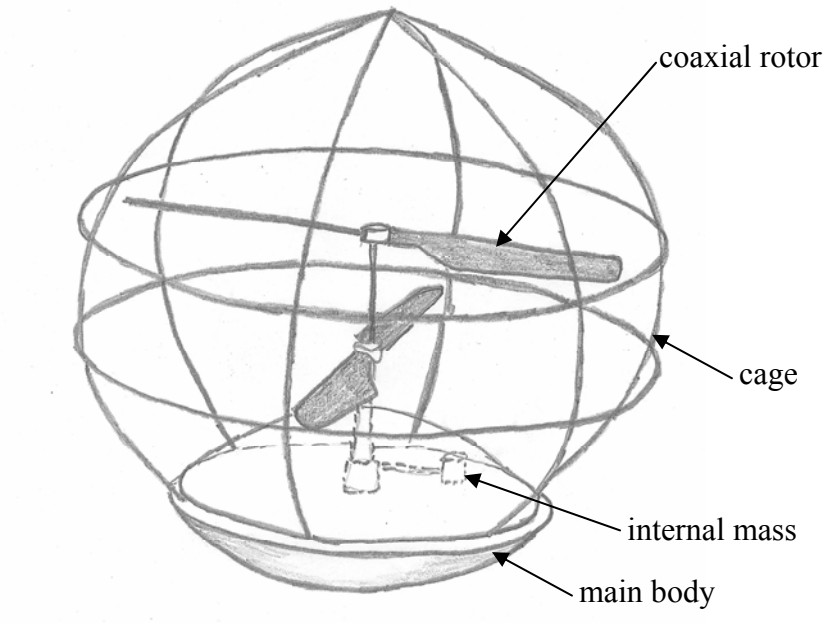

Figure 2.4: Fourth generation Hopping Rotochute conceptual design

To eliminate this shortcoming, a fourth generation conceptual design was proposed as shown in Figure 2.4. This design has many of the same characteristics as the third generation concept, but includes an egg-shaped roll cage. This exterior shape, in combination with the low mass center, would allow the vehicle to passively upright itself no matter what the landing orientation while protecting the rotating components. Based on this design concept, a Hopping Rotochute prototype was designed and fabricated as discussed below.

2.2 Hopping Rotochute Components

As with all hopping or flying vehicles, the design and layout of the system is critical for overall performance. This is especially true for the Hopping Rotochute, which requires a low mass center and a specially shaped body which in combination, passively reorients the body to an upright orientation once on the ground. The vehicle must also be lightweight and small so it can fit through tight spaces and increase the achievable jump height and total range. With these considerations in mind, the Hopping Rotochute prototype was split into three separate subsystems (the propulsion system, the electronics, and the main body) which were designed in an integrated fashion.

2.2.1 Propulsion System

In order to avoid the complexities associated with building a rotor system from scratch, pre-built rotor systems were investigated to incorporate into the Hopping Rotochute design. As mentioned above, several different rotor systems could be used to produce the thrust required to elevate the vehicle, but a coaxial rotor system was chosen due to its compactness and inherent ability to produce near zero torque on the body during powered flight. To assess the characteristics of off-the-shelf rotor systems, three

different coaxial micro helicopters were purchased including a Bumble Bee (FJ-707B), a Leopard (FJ-712D), and an Air Hogs Reflex micro helicopter as shown in Figure 2.5.

Figure 2.5: Bumble Bee, Leopard, and Reflex micro helicopters (from left to right)

As outlined in Table 2.1, each of these micro helicopters have similar rotor blade properties, but they incorporate stabilizer bars and directional control mechanisms of different designs. These helicopters were flown to characterize their stability and ease of use. The rotor system associated with both the Leopard and Bumble Bee were found to be fairly unstable when perturbations or wind gusts were applied to them. The Reflex, on the other hand, demonstrated favorable stability properties, ease of trimming, and use of only one electric motor. Based on these properties, the rotor system of the Reflex was chosen to power the Hopping Rotochute prototype.

Table 2.1: Properties of pre-built micro helicopters

Helicopter	Mass (g)	Rotor Radius (cm)	Mean Chord (cm)	Number of Motors
Bumble Bee	67.0	10.4	2.3	2
Leopard	58.3	10.4	2.3	2
Reflex	50.5	10.6	2.0	1

In order to incorporate the Reflex's propulsion system into the Hopping Rotochute design and to provide necessary rotor spacing, the upper and lower rotor shafts were extended. Figure 2.6 presents an exploded view of the modified rotor system, including the transmission used for the final design of the Hopping Rotochute. As shown in Figure 2.7, a small brushed DC electric motor drives a single shaft with a 1:5.4 gear ratio which drives the upper and lower rotor shafts in opposite directions with a 1:2.4 gear ratio.

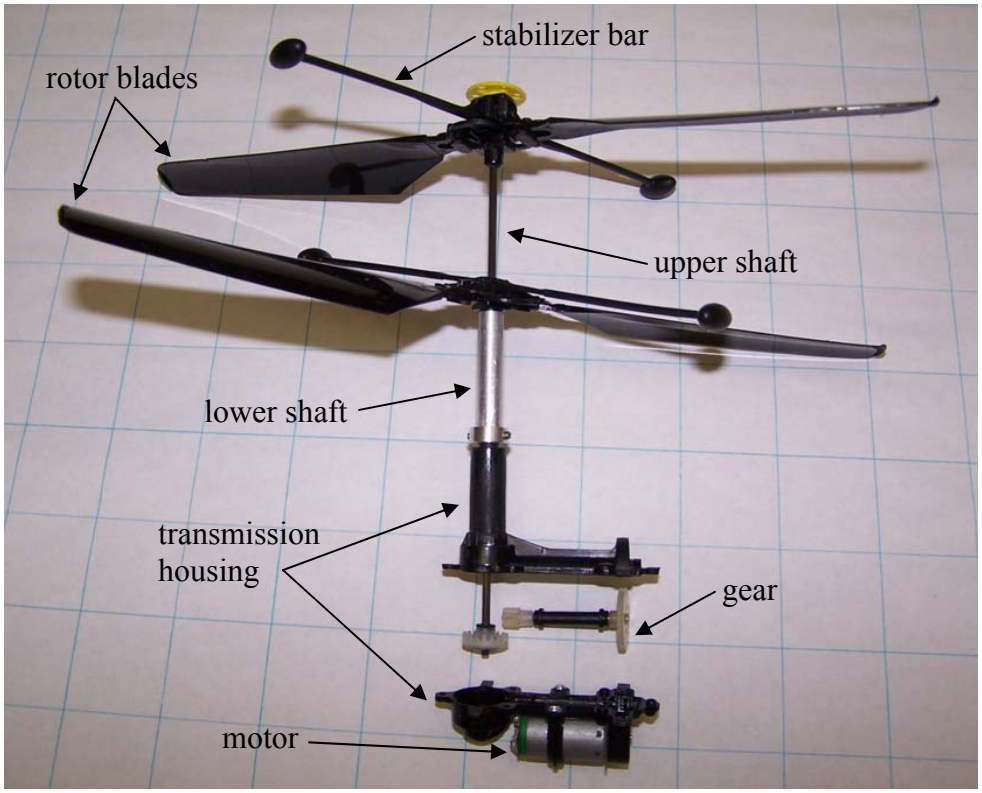

Figure 2.6: Modified Reflex rotor system and transmission

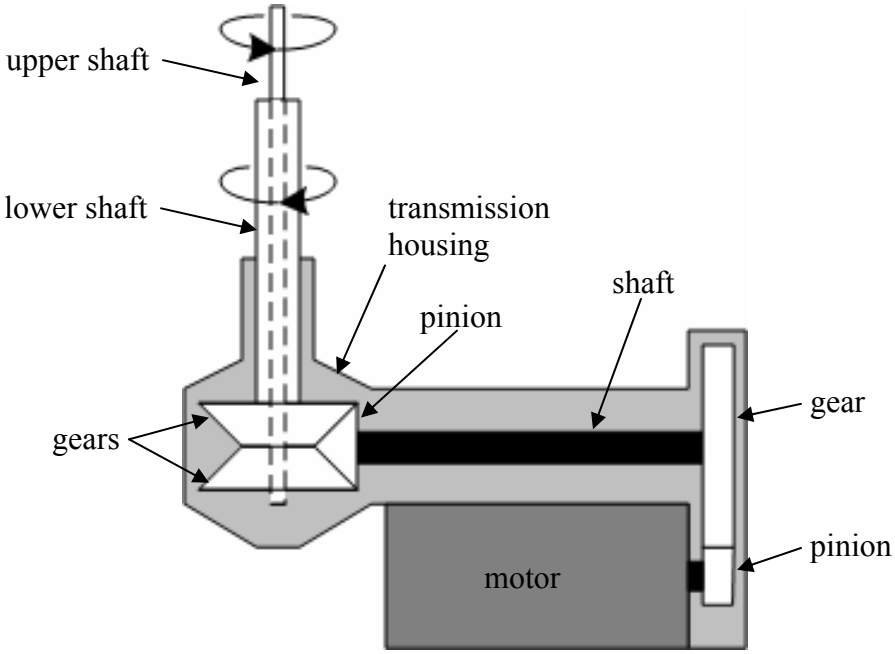

Figure 2.7: Schematic of transmission

2.2.2 Electronics

In order to radio control the Hopping Rotochute prototype, the signals from the radio must be received and processed by onboard electronics to power the device. To achieve this, many different off-the-shelf electronic devices were purchased and tested as described below.

Three different receivers were investigated including the CIRRUS Micro Joule, the CIRRUS MRX-4, and the HITEC Micro 05S as shown in Figure 2.8. The properties of these micro receivers are presented in Table 2.2.

Figure 2.8: CIRRUS Micro Joule, CIRRUS MRX-4, and HITEC Micro 05S receivers (left to right)

Table 2.2: Properties of receivers

Rx #	Receiver	Mass (g)	Size $L \times W \times H$ (mm)	Number of Channels
1	CIRRUS Micro	3.0	28.2 × 7.9 × 8.4	4
2	CIRRUS MRX-4	9.0	32 × 10 × 12	4
3	HITEC Micro 05S	8.6	37 × 19 × 10	5

To control the speed of the rotor blades, an electronic speed controller (ESC) was employed. Three different micro ESCs were investigated including the CIRRUS Micro Joule S5A1, CIRRUS Micro Joule S5A2, and the Electrifly C-7 Nano. A picture of each is given in Figure 2.9 whereas the properties are given in Table 2.3.

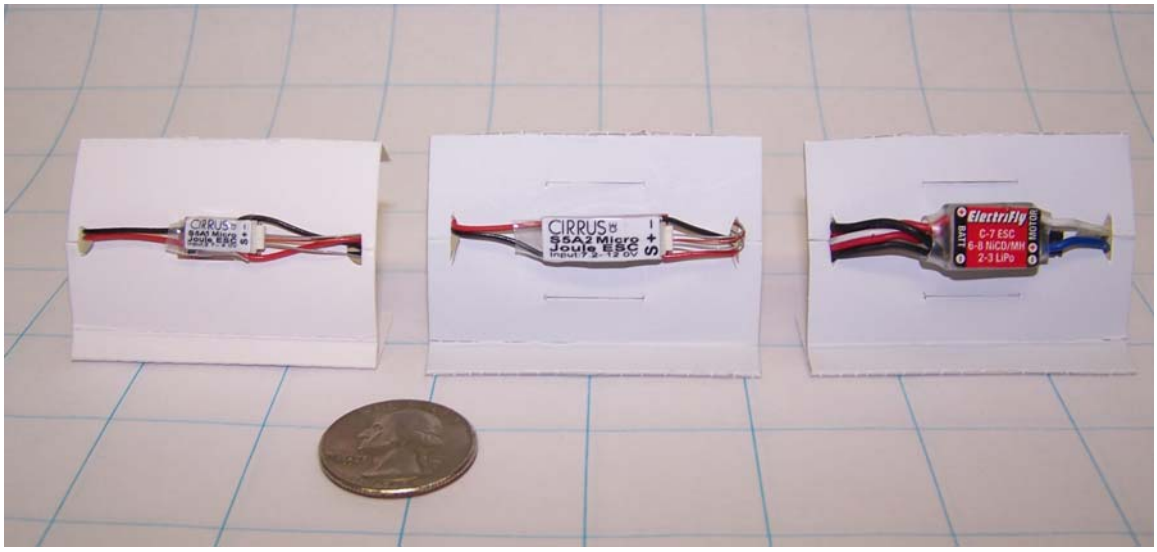

Figure 2.9: CIRRUS Micro Joule S5A1, CIRRUS Micro Joule S5A2, and Electrifly C-7 Nano electronic speed controllers (left to right)

Table 2.3: Properties of electronic speed controllers

ESC #	Electronic Speed Controller	Mass (g)	Size $L \times W \times H$ (mm)	Input Voltage (V)	Continuous Current (A)
1	CIRRUS Micro Joule S5A1	1.9	12.5 × 6.5 × 3.6	2.7 – 4	5
2	CIRRUS Micro Joule S5A2	2.8	18.8 × 8.0 × 6.3	7.2 – 12	5
3	Electrifly C-7 Nano	5.5	17 × 11 × 7	7.2 – 12	7

The position of the internal mass is controlled by a micro servo. Three different servos were investigated including the CIRRUS CS101/STD Micro, the HITEC HS-50 Feather, and the HITEC HS-45HB Premium Feather. A picture of these servos is given in Figure 2.10 and the properties are outlined in Table 2.4.

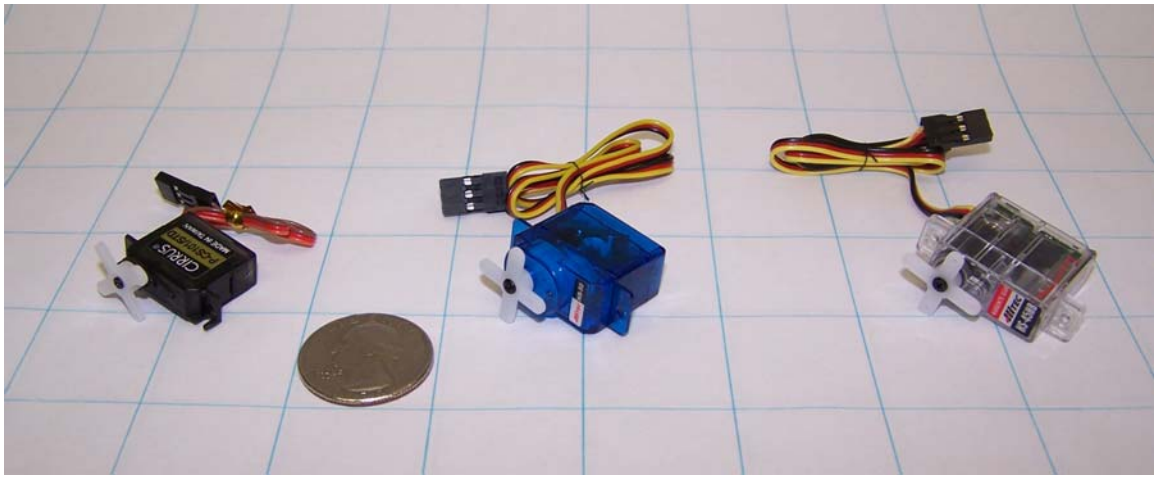

Figure 2.10: CIRRUS CS101/STD Micro, HITEC HS-50 Feather, and HITEC HS-45HB Premium Feather servos (left to right)

Table 2.4: Properties of servos

Servo #	Servo	Mass (g)	Size $L \times W \times H$ (mm)	Speed at 4.8 V (s/60 deg)	Torque at 4.8 V (kg·cm)
1	CIRRUS CS101/STD	4.0	15.5 × 7.5 × 19	0.11	0.7
2	HITEC HS-50	6.1	21 × 11 × 22	0.09	0.6
3	HITEC HS-45HB	8.0	23.6 × 9.8 × 22.4	0.14	1.0

Based on the properties outlined in Tables 2.2, 2.3, and 2.4, a system controlled with Rx 1, ESC 1, and Servo 1 would result in the lightest vehicle. Unfortunately, the

low input voltage of ESC 1 limits the amount of power delivered to the rotor system and prevents vehicle flight. A system with Rx 3, ESC 3, and Servo 3 was also tested which allowed the vehicle become airborne at the cost of increased weight. Consequently Rx 1, ESC 2, and Servo 2 was tested which showed a good compromise between low weight and available power. To further decrease the weight, Servo 1 was incorporated into the design with Rx 1 and ESC 2 and this combination was used to control and power the final Hopping Rotochute prototype.

The Hopping Rotochute prototype can be powered by an array of batteries having a voltage between 7.2 and 12 V which is compatible with the electronics outlined above. The batteries used during the testing of the prototype, shown in Figure 2.11, include a 250, 300, and 480 mAh battery as outlined in Table 2.5.

Figure 2.11: Apache 250 mAh, Electrifly 300 mAh, and Thunder Power 400 mAh batteries (left to right)

Table 2.5: Properties of batteries

Manufacturer	Capacity (mAh)	Mass (g)	Size $L \times W \times H$ (mm)	Contiunous Discharge (A)
Apache	250	13.7	32 × 26 × 10	5
Electrifly	300	19.8	51 × 32 × 8	6
Thunder Power	480	24.6	52 × 34 × 8	7.2

2.2.3 Main Body

The main body of the Hopping Rotochute prototype consists of several components including the core, the cage, the cushion, and the mounting bracket as shown in Figure 2.12. Each component of the main body was designed to decrease weight, increase strength, and lower the mass center while creating an exterior shape to help protect the rotating components and allow the body to self-right itself. The design and materials used for each component are outlined below.

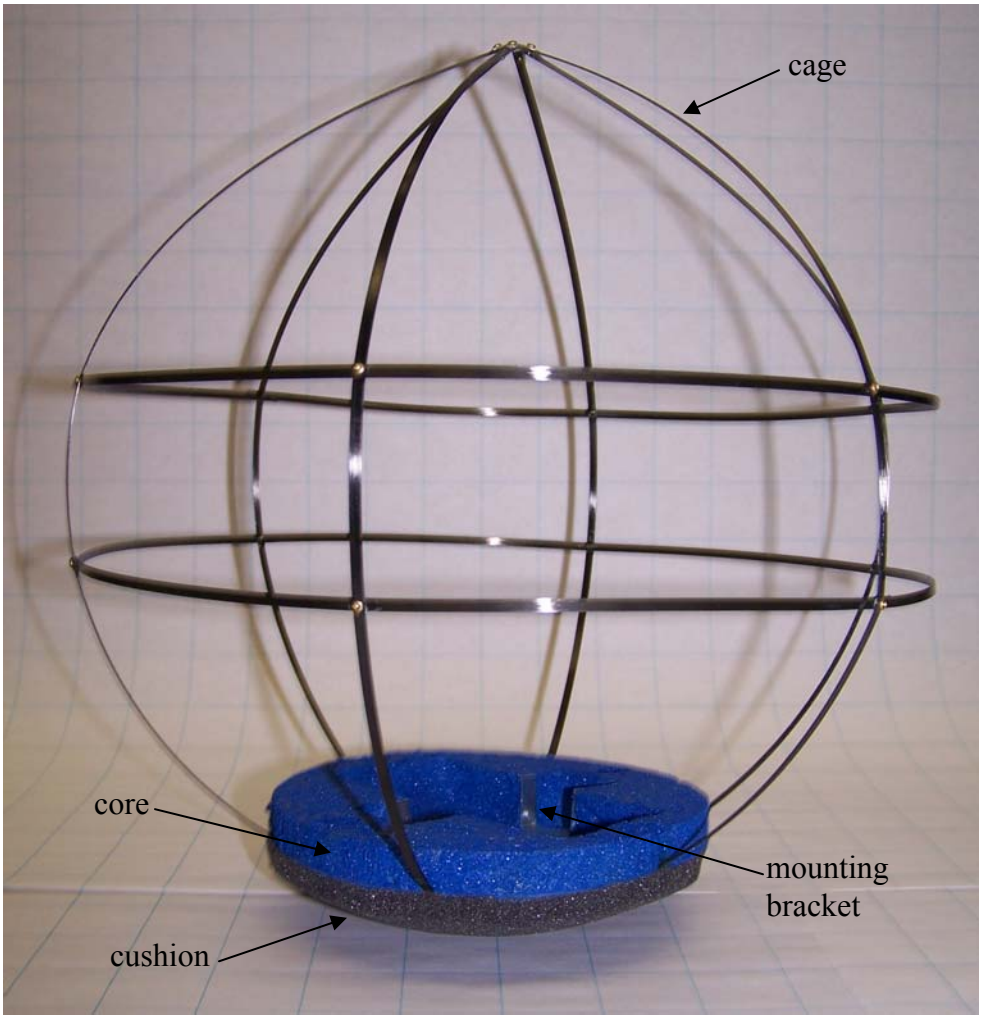

Figure 2.12: Hopping Rotochute prototype main body

Several different types of materials were considered for the core including Styrofoam, expanded polypropylene (EPP) foam, expanded polystyrene (EPS) foam, and acrylic. Considering that the core should be light weight, rigid, and have a good compression recovery, EPP foam was chosen with a density of 30.4 kg/m^3 (1.9 lb/ft^3).

The cage was designed to naturally self-right the vehicle while protecting the rotating components. To achieve this while minimizing weight, five carbon fiber strips

were arranged around the propulsion system. As shown in Figure 2.12, three of the strips run longitudinally while the other two carbon fiber strips run laterally.

Several types of foams were considered for the cushion material in the hopes of finding one that is light weight, has good compression recovery, and dampens the vehicle quickly when in contact with the ground. In order to determine the best candidates, foam samples were weighed and an acrylic ball of the approximate weight of the Hopping Rotochute prototype was dropped onto each to determine the compression recovery and damping characteristics. Of these samples, the three foam materials that performed the best were the slow-recovery (SR) polyurethane, polyurethane, and polyimide. This subset of 6.35 mm (¼ in) thick foam materials was further tested and the results described below.

The cushion material spring constants were determined by placing each foam sample onto a scale and deflecting it by a known amount to determine the force exerted. The results of this experiment are shown in Figure 2.13 which plots the force as a function of deflection. Considering the initial linear part of each curve and using Hooke's law of elasticity,

$$F = -kx \tag{2.1}$$

the spring constants were determined to be 8300, 12,120, and 2290 N/m for the SR polyurethane, polyurethane, and polyimide respectively.

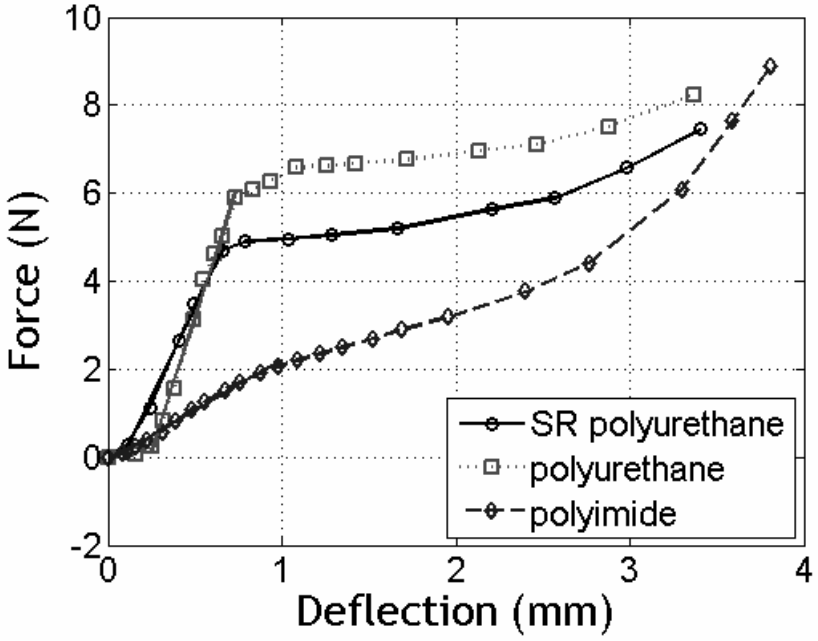

Figure 2.13: Foam cushion force versus deflection

The damping coefficient of each material was determined by using a drop test stand, shown in Figure 2.14 a), and comparing the results to the predicted motion of a spring-mass-damper model. The drop test stand consists of two pieces: a stand and a slider. The stand was made of a plywood structure with a small stainless steel tube attached at the top and a material sample placed at the bottom. The slider consists of a long, smaller diameter stainless steel tube which is connected to a curved base with a material sample attached to the bottom of it. The tube of the slider is able to translate inside the tube of the stand with negligible friction. A schematic of the spring-mass-damper model is given in Figure 2.14 b). The equations of motion of this system during contact is given in equation 2.2

$$m\ddot{z} + \frac{1}{2}c\dot{z} + \frac{1}{2}kz = W \tag{2.2}$$

where m is the mass, c is the damping coefficient, k is the spring constant, $-z$ is the altitude, and W is the weight of the system. The natural frequency of this system is described by

$$\omega_n = \sqrt{\frac{k}{2m}} \tag{2.3}$$

whereas the damping ratio is described by equation 2.4.

$$\zeta = \frac{c}{4m\omega_n} \tag{2.4}$$

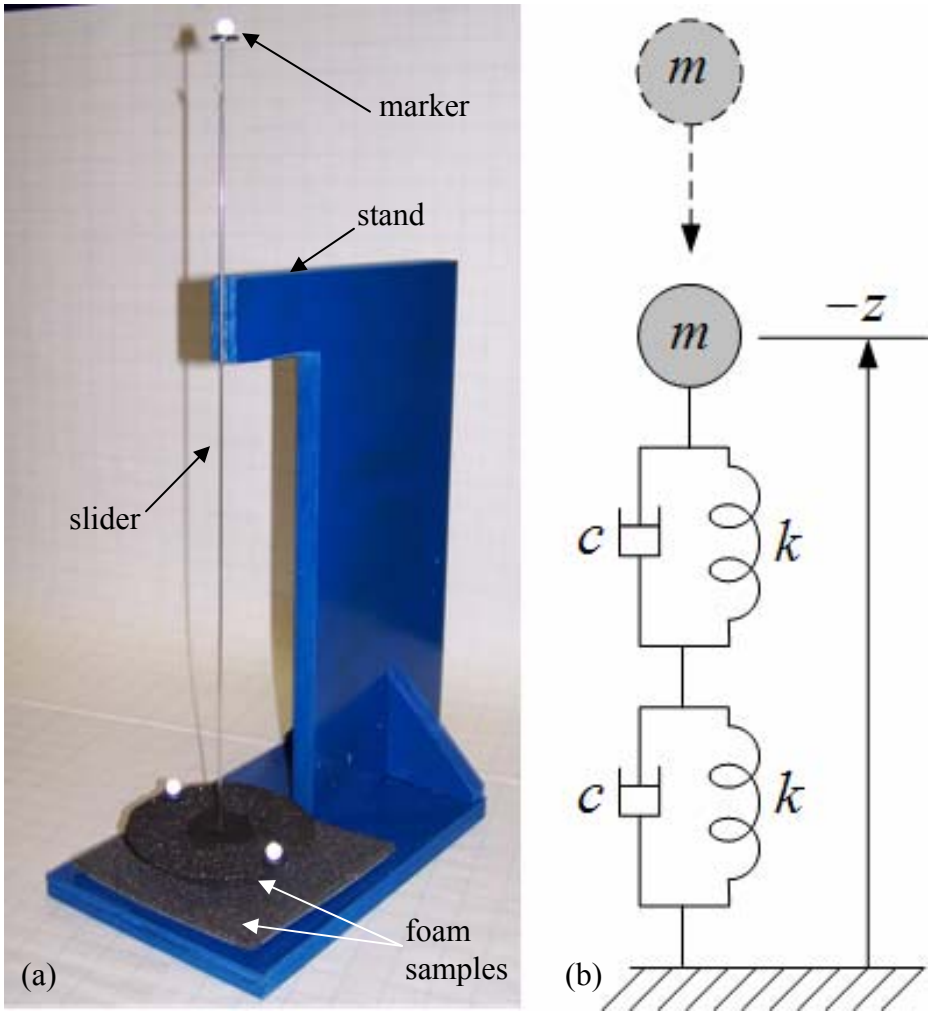

Figure 2.14: Drop test stand and model of drop test stand (left to right)

For each material sample, the slider was lifted to a height of 0.3 m and released. The motion was recorded using a motion capture system (described in Chapter 5.1) and was compared with the simulation results of the spring-mass-damper model using the same initial conditions, mass properties, and spring constants. The damping coefficient of the model was adjusted until the captured motion and the simulation results correlated. An example result is presented in Figure 2.15 which plots the altitude as a function of time. Here the solid line represents the data from the motion capture system

(experimental) and the dashed line is the simulated (theoretical) result. As shown, good correlation between the theoretical and experimental results can and does exist. Using this method, the damping coefficient of the slow-recovery polyurethane, polyurethane, and polyimide were determined to be approximately 29.7, 26.6, and 16.0 N·s/m respectively. The natural frequency and damping ratio of each material is given in Table 2.6.

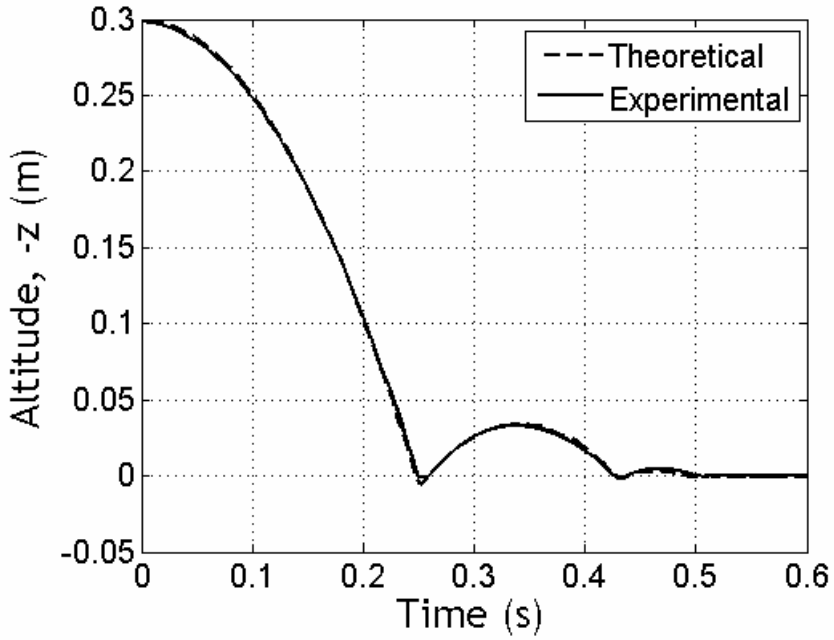

Figure 2.15: Altitude versus time associated with drop test stand

Table 2.6: Cushion foam material properties

Material	Density (kg/m^3)	Compression Recovery	Natural Frequency, ω_n (rad/s)	Damping Ratio, ζ
SR polyurethane	93	excellent	235	0.42
polyurethane	32	good	284	0.31
polyimide	6.4	poor	128	0.45

Based on the data in Table 2.6, using a polyimide cushion would result in the lightest vehicle with the best damping characteristics. Unfortunately, the poor compression recovery associated with the polyimide results in little damping/energy absorption after several successive hops. On the other hand, slow recovery polyurethane has excellent compression recovery, but weighs approximately 15 times that of the polyimide. A compromise was reached by using the polyurethane for the cushion material of the Hopping Rotochute prototype.

2.3 Final Prototype Design and Layout

The final design of the Hopping Rotochute prototype is shown in Figure 2.16. As shown, the transmission of the propulsion system and the micro servo are attached to a fabricated transmission mount which slides in between and is secured by the mounting brackets adhered to the core. The receiver and electronic speed controller are also attached to the transmission mount, while the battery fits snuggly between the bottom of the transmission mount and the foam core. A nylon gear is attached to the servo which drives a nylon pinion attached to the internal mass assembly. The 4:1 gear ratio allows the internal mass to rotate ±180 deg with the typical ±45 deg rotation of the servo. All these components are located at the bottom of the vehicle in order to lower the mass center.

The two rotors are situated sufficiently far from the core and from each other so vertical drag and wake interactions are minimized. The cage was designed around the propulsion system to protect the rotating components while allowing the vehicle to naturally self-right itself. The Hopping Rotochute is radio controlled using a FUTABA

T6EXA radio. Channel 1 is associated with the throttle to power the rotor blades and channel 4 controls the internal mass orientation by means of the servo and gear train.

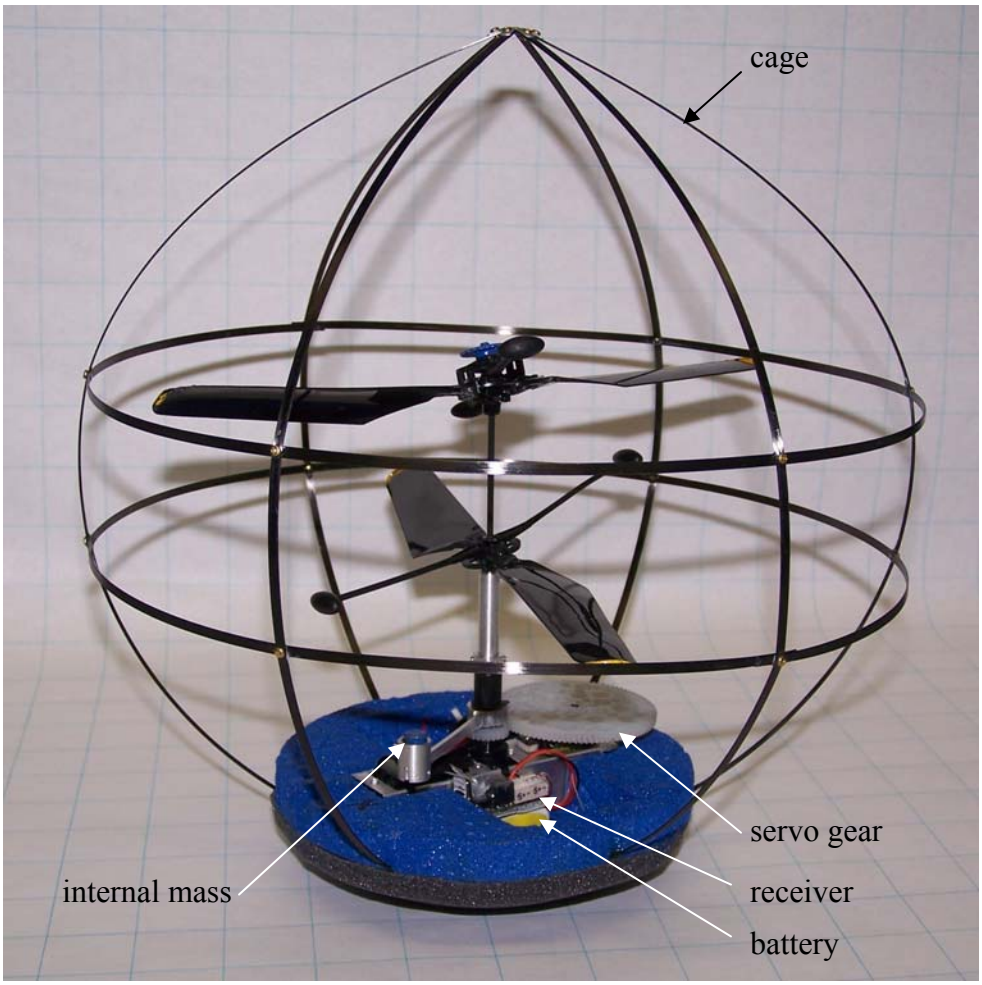

Figure 2.16: Hopping Rotochute prototype

The layout of the Hopping Rotochute prototype is shown in Figure 2.17. The vehicle has an overall height of 25.4 cm and a maximum horizontal diameter of 24.13 cm. The mass and location of the individual components are given in Table 2.7, where d_{CG_i} is the vertical distance from the bottom of the prototype to the mass center of each of

the components. The total mass of the vehicle, including the 250 mAh battery and excluding the internal mass and internal mass assembly is 78.3 g. The fabrication of the prototype is outlined in Appendix A and the drawings of the components is given in Appendix B.

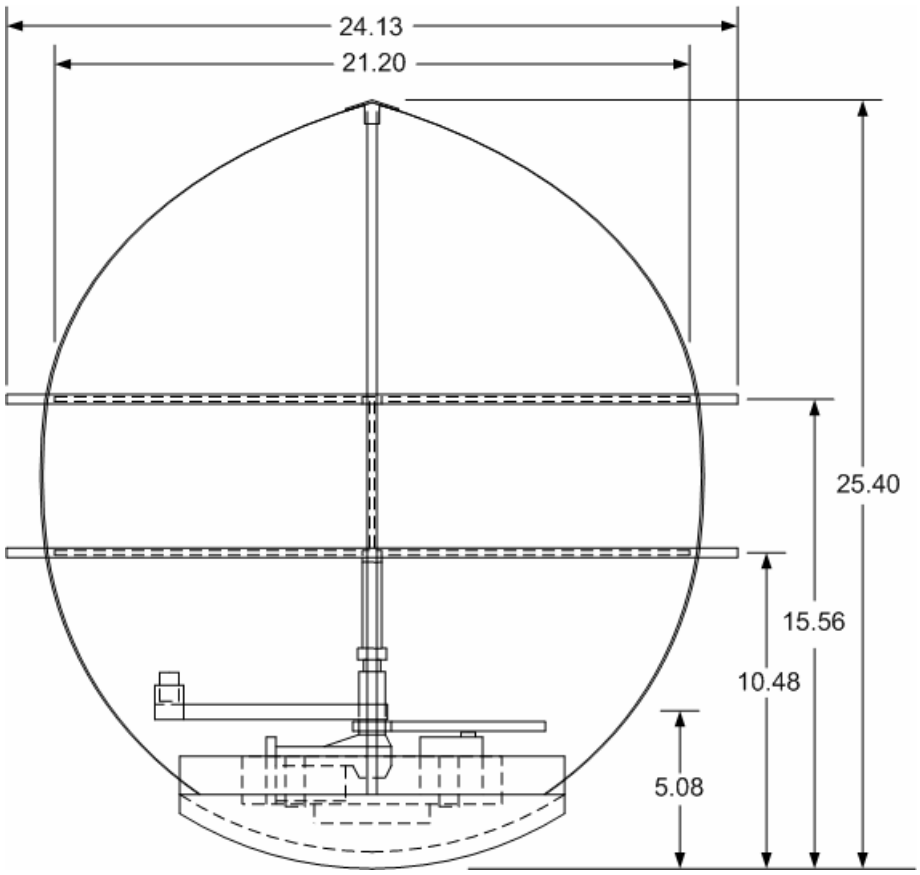

Figure 2.17: Hopping Rotochute prototype layout (units in cm)

Table 2.7: Mass properties of components

Component	Mass (g)	d_{CG_i} (cm)
EPP foam core	7.6	2.7
polyurethane foam cushion	3.1	1.7
1st longitudinal carbon fiber strip	2.0	12.7
2nd longitudinal carbon fiber strip	2.0	12.7
3rd longitudinal carbon fiber strip	2.0	12.7
bottom latitudinal carbon fiber strip	2.0	10.5
top latitudinal carbon fiber strip	2.0	15.6
motor, transmission, electronics, and tran. mount	32.9	2.9
lower rotor and shaft	5.5	10.5
upper rotor and shaft	5.5	15.6
battery (250 mAh)	13.7	1.3
total (without internal mass)	78.3	5.2

CHAPTER 3

TESTING OF THE HOPPING ROTOCHUTE PROTOTYPE

In order to test the feasibility of the Hopping Rotochute design, the fabricated prototype was tested in a number of different scenarios. The purpose of these tests was to evaluate the capabilities of the prototype with regards to the appointed system requirements. In addition, the rotor system was tested to determine its aerodynamic characteristics which also influence the capabilities of the device. The details and results of these tests are discussed in this chapter and in [41].

3.1 Rotor System Aerodynamic Analysis

The coaxial rotor system of the Hopping Rotochute prototype is a key component in realizing many of the system requirements assigned to the vehicle. The counter-rotating rotors provide the necessary lift to allow the vehicle hop and its aerodynamic efficiency is directly related to how far the vehicle can travel before the battery is completely drained. In order to determine the aerodynamic characteristics of the Hopping Rotochute prototype rotor system, several different methods were considered including a blade element momentum theory (BEMT) analysis [42-46], a computational fluid dynamics (CFD) analysis [47-51], and the employment of a rotor test stand [52-58]. To avoid the complexities involved in the BEMT and CFD analyses, a custom-made rotor test stand was fabricated to experimentally obtain the aerodynamic characteristics of the rotor system as shown in Figure 3.1. The rotor test stand consists of an aluminum bar that can pivot about an adjustable-height PVC pipe. The Hopping Rotochute was attached to one end of the aluminum bar while an aluminum rod was attached to the other

end. As the rotors are powered, the rod pushes against a digital scale, which measures the thrust being produced at a given rotor speed. The rotor speed was measured using a tachometer while multimeters were employed to measure the current and voltage going through and across the motor.

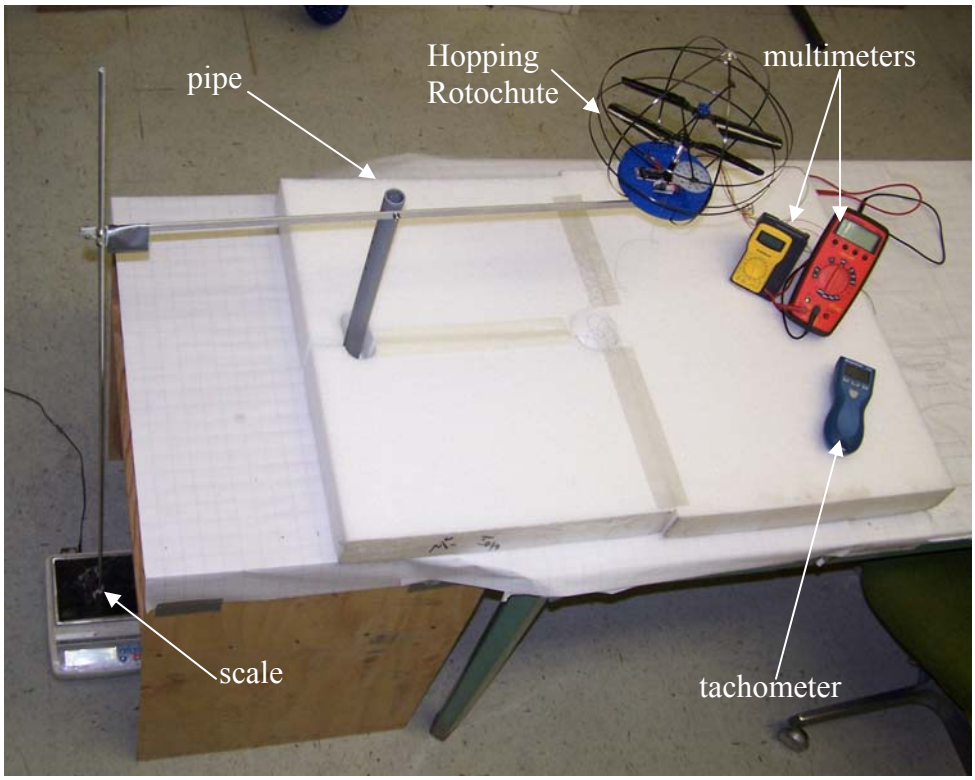

Figure 3.1: Rotor test stand

Using the rotor test stand, the thrust, current, and voltage were measured at several rotor heights above the ground and rotor speeds. The rotor speed was varied up to 2100 r/min while the rotor height was varied from 10.1 cm to 38.1 cm above the ground. The results were curve fit, extrapolated to 2500 r/min, and are presented in Figures 3.2 through 3.4. The power was also calculated as a function of height and rotor

speed and is plotted in Figure 3.5. As shown, the thrust, current, and potential increase in a quadratic manner with rotor speed. It is also interesting to note the in-ground-effect and out-of ground-effect of this system. At a height of 30.5 cm, about 1.5 times the rotor diameter, the system reaches out-of ground-effect.

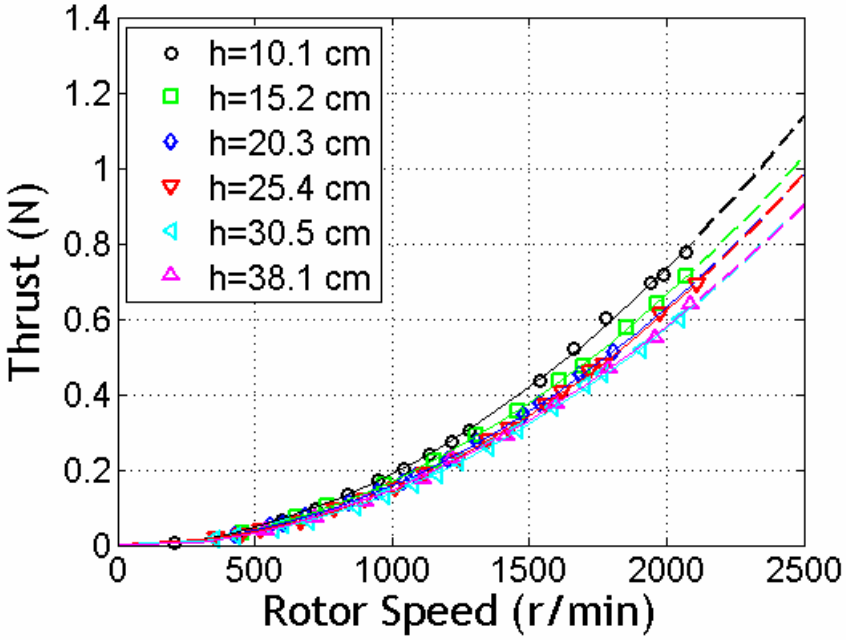

Figure 3.2: Rotor thrust versus rotor speed

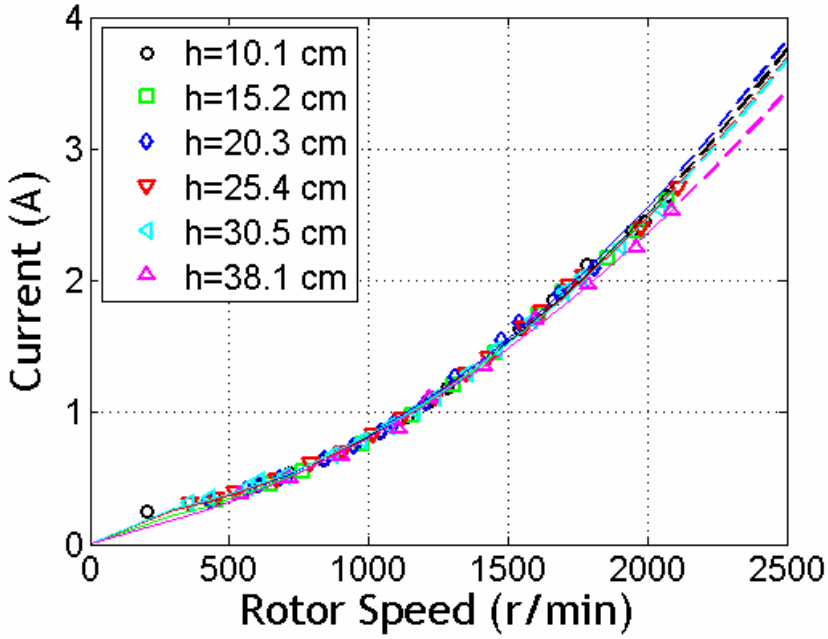

Figure 3.3: Current versus rotor speed

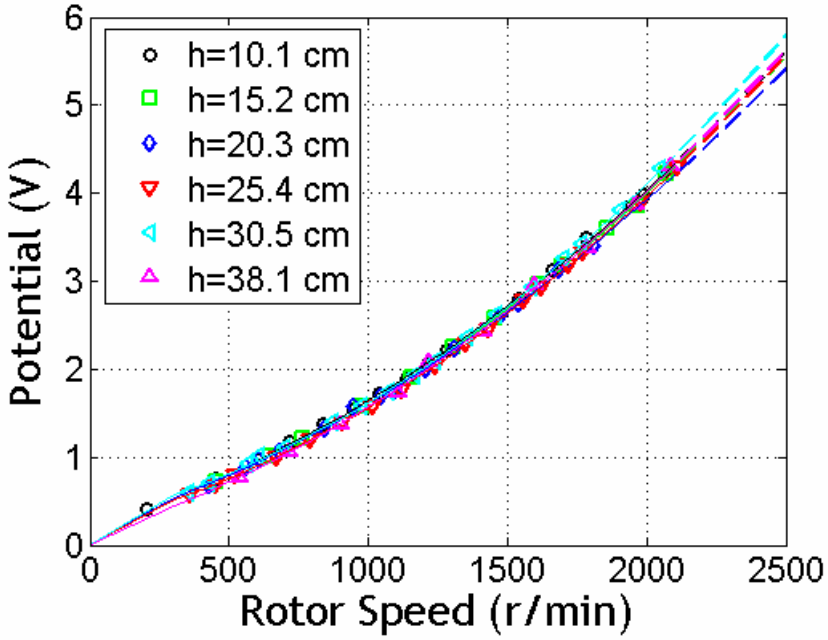

Figure 3.4: Potential versus rotor speed

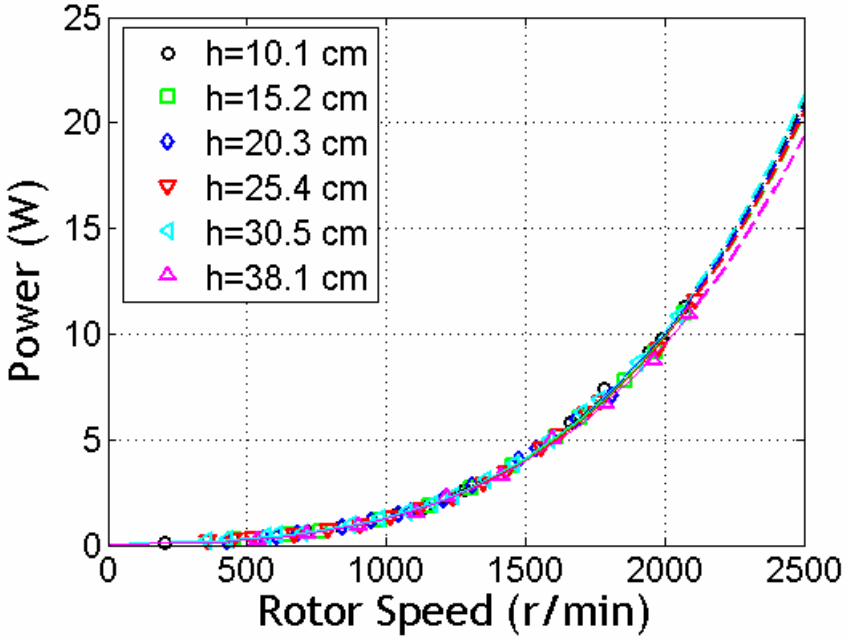

Figure 3.5: Power versus rotor speed

The figure of merit (*FM*) of a given rotor system can be used to approximate how efficient the hovering rotor is in terms of generating thrust for a given power [42]. The figure of merit of the rotor system used on the Hopping Rotochute prototype was calculated using equation 3.1

$$FM = \frac{C_T^{3/2}}{\sqrt{2}C_P} \tag{3.1}$$

where the coefficient of thrust (C_T) and coefficient of power (C_P) are calculated using equations 3.2 and 3.3.

$$C_T = \frac{T}{\rho A \Omega^2 R^2} \tag{3.2}$$

$$C_P = \frac{P}{\rho A \Omega^3 R^3} \tag{3.3}$$

The thrust (T), power (P), and rotor speed (Ω) used in these equations are based on values found from the curves of Figures 3.2 and 3.5. Given that the sum of the vehicle weight and the download (0.858 N) must equal the total thrust of the hovering rotor system, the rotor speed and the total power were found to be 2440 r/min and 17.9 W respectively. Assuming that each rotor produces one-half of the total thrust and consumes one-half of the total power, the thrust and power used in equations 3.2 and 3.3 are 0.429 N and 8.95 W. Using an air density (ρ) of 1.225 kg/m^3, a rotor radius (R) of 10.6 cm, and an area (A) of 353 cm^2, the figure of merit was calculated to be 11%. The associated disc loading ($DL=T/A$) was calculated to be 12.15 N/m^2 whereas the coefficient of thrust was calculated to be 0.0135. The calculated figure of merit is low which is a common result associated with small rotor systems used on micro air vehicles operating at low Reynolds numbers. For example, the figure of merit reported by Bohorquez and Pines presents values only up to 33% for a single main rotor using a NACA 0012 airfoil at 2500 r/min [58]. Although this value of the figure of merit is 3 times higher than that calculated for the rotor used on the Hopping Rotochute, the *FM* associated with the Hopping Rotochute includes vertical download, transmission losses, as well as wake interactions from the two counter-rotating rotors. All these effects decrease the efficiency and results in a lower figure of merit as compared to the results presented in [58].

3.2 Flight Testing of the Hopping Rotochute Prototype

To demonstrate the feasibility of the Hopping Rotochute prototype, many flight tests were performed in a variety of different environments. The initial flight tests were performed by simply powering the prototype's rotor system and hopping the vehicle at different heights around the Indoor Flight Facility (described in Chapter 5.1) while using a 2.7 g internal mass at a 5.4 cm offset for directional control. The motion of one such hop sequence was recorded using the motion capture system (described in Chapter 5.1) and the results are given in Figures 3.6 through 3.15. Figures 3.6 and 3.7 present the center of mass position associated with the hop sequence in 3 and 2-dimensional space respectively. Figure 3.7 also demonstrates the orientation of the internal mass before the hops were initiated. Here the white circle represents the horizontal cross-section of the vehicle and the grey circle represents the internal mass. For this particular hop sequence, the internal mass was initially oriented to -90 deg from the x-axis and was held at this angle with respect to the body during the first hop. Before the second hop was initiated, the internal mass was rotated to 70 deg from the x-axis and was fixed at this orientation with respect to the body during the second flight. Figures 3.8 and 3.9 show the range and cross range of the vehicle's mass center as a function of time. As shown, the initial internal mass orientation allowed the Hopping Rotochute prototype to hop 2.93 m along the negative y-axis while achieving a height up to 1.85 m (see Figure 3.10). As mentioned earlier, after the first flight the internal mass was reoriented allowing the vehicle to achieve both range and cross range during the second hop with a total horizontal distance of 1.73 m. Figure 3.10 shows the prototype reached a maximum altitude of 1.22 m during the second hop. The pitch angle of the vehicle during the hop sequence is shown in Figure 3.11. During the first hop, the pitch angle initially increased up to 8.5 deg while the rotors were powered and then subsequently decreased until the power ceased at 2 s due to the stability properties of the rotor system. Once power ceased, the vehicle yawed and the angular momentum of the body pitched the vehicle up

to 35 deg before the aerodynamic forces rotated it the opposite direction. At 3.1 s, the prototype contacted the ground after which the vehicle pitched back and forth with a natural frequency of about 8 rad/s and a damping ratio of 0.1 until the nominal orientation was reached. As shown in Figure 3.11, the same type of pitching behavior occurred during the second hop which demonstrates the ability of the Hopping Rotochute prototype to passively upright itself.

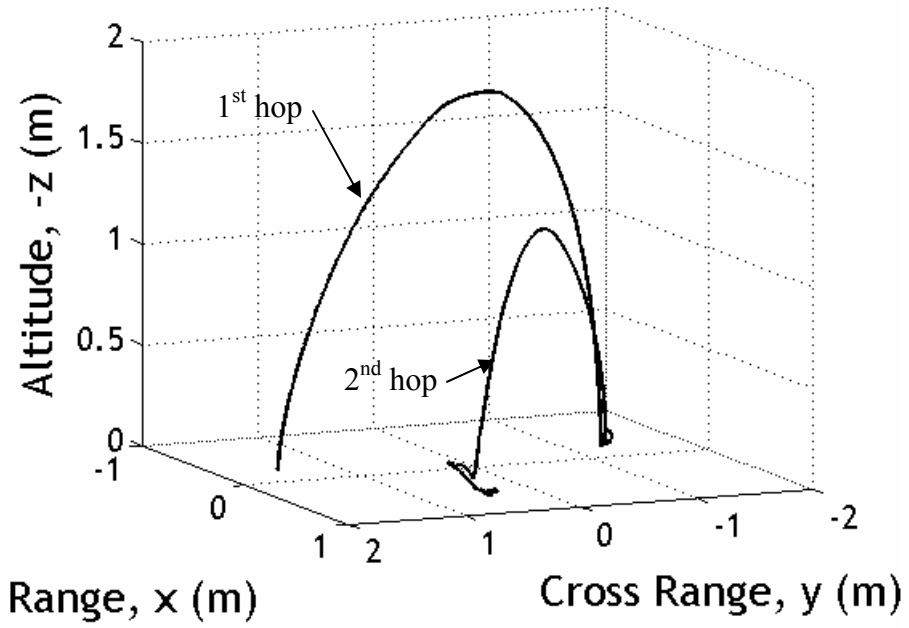

Figure 3.6: Altitude versus cross range versus range

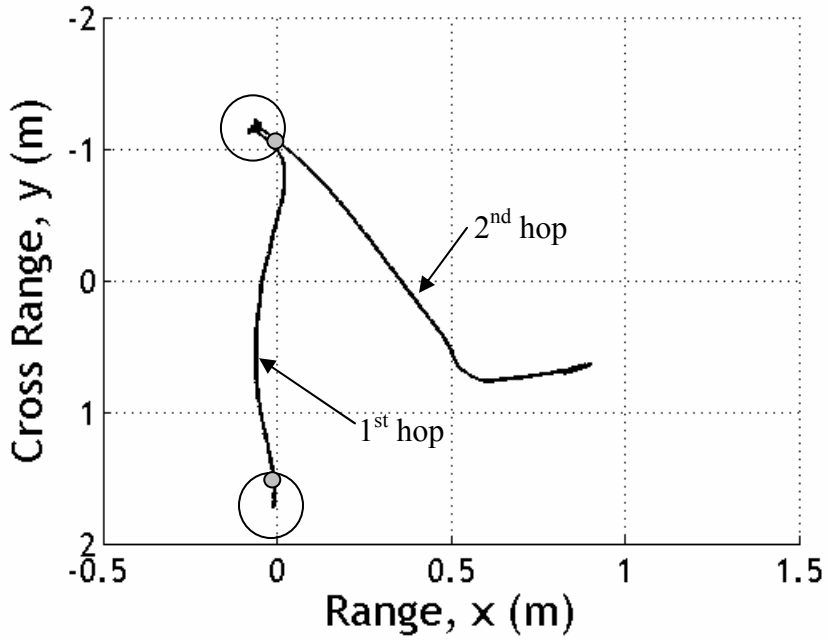

Figure 3.7: Cross range versus range

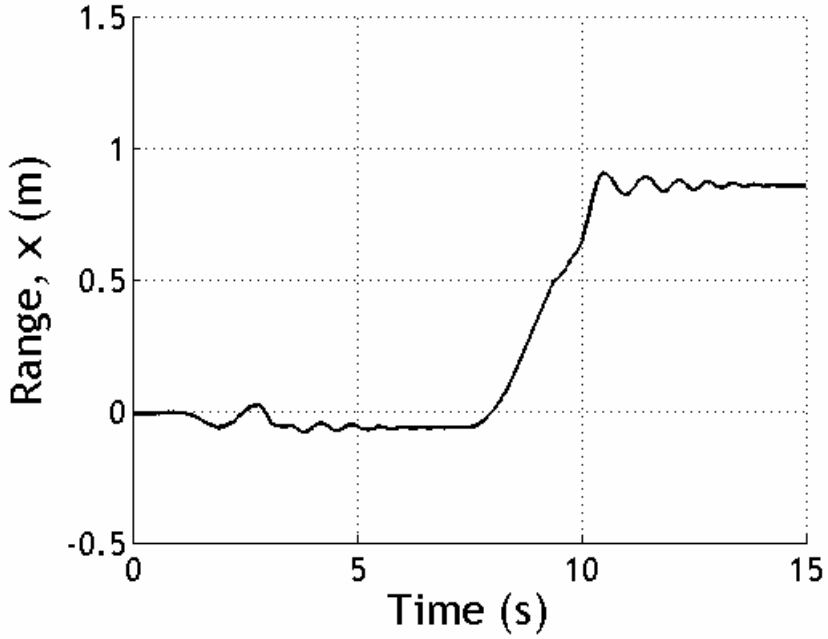

Figure 3.8: Range versus time

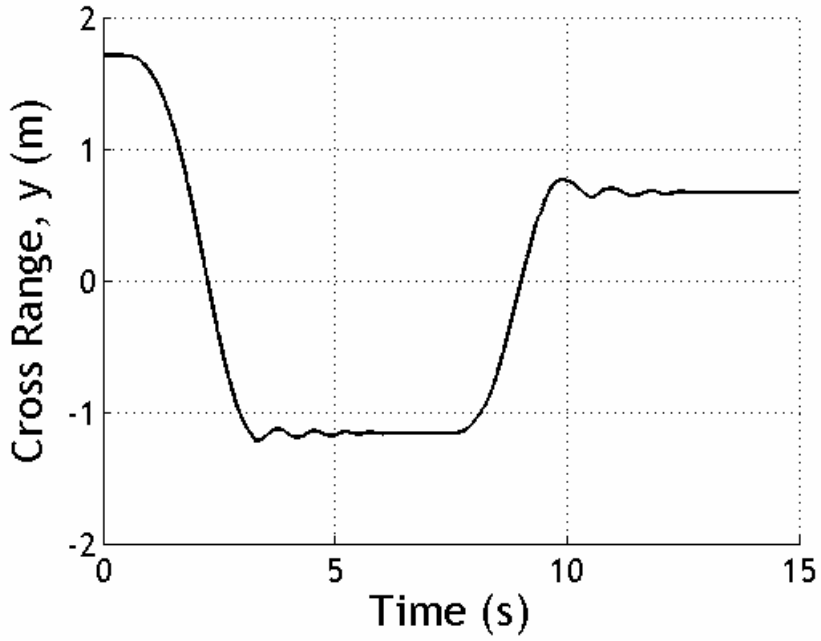

Figure 3.9: Cross range versus time

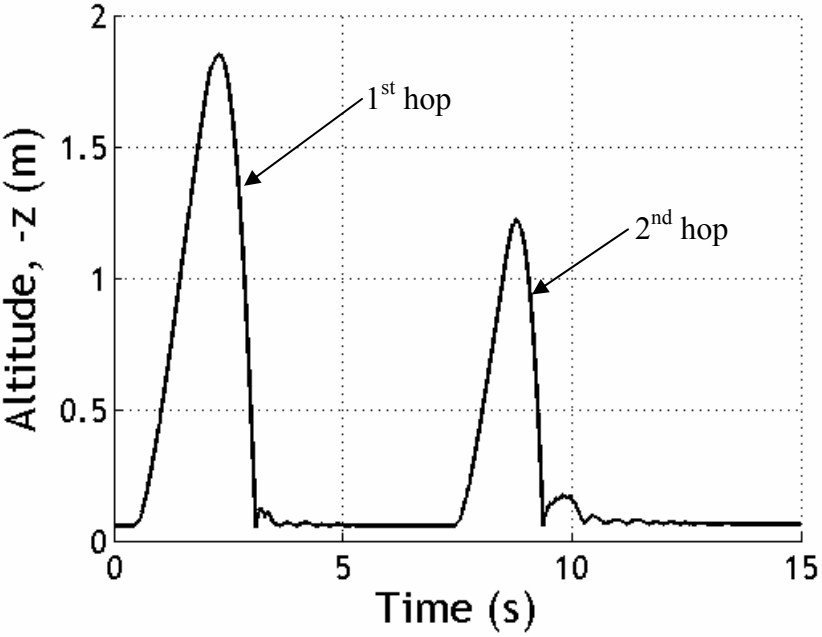

Figure 3.10: Altitude versus time

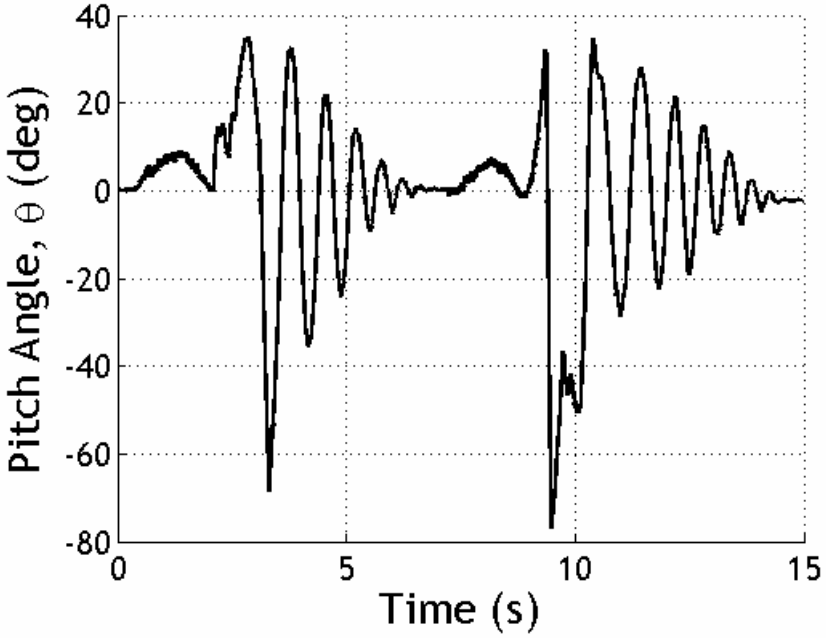

Figure 3.11: Pitch angle versus time

Figure 3.12 presents the rotor speed profile which was calculated based on the captured data. As shown, the rotor speed quickly ramped up to approximately 2550 r/min during the first hop where it remained fairly constant for 1.5 s before decreasing back down to zero. The rotor speed associated with the second hop also ramped up quickly to about 2525 r/min and was held fairly constant for approximately 1 s before the power was ceased. Using these rotor speed profiles and the results from the rotor test stand, the thrust, current, and power were calculated for this hop sequence and are presented as a function of time in Figures 3.13 through 3.15 respectively. As shown, the small electric motor is able to produce a thrust greater than 1 N requiring a power exceeding 20 W which allows the vehicle to become airborne. By numerically integrating the current versus time curve, shown in Figure 3.14, the amount of battery discharge during each hop was calculated. During the first and second hop, the battery discharged approximately 2.0 and 1.4 mAh respectively. Given that the prototype traveled 2.93 m in the horizontal plane during the first hop, the total number of hops and total achievable range of this

system using the 250 mAh battery and this hop profile is 120 and 360 m respectively. Using the profile of the second hop, the prototype would be to achieve 180 hops while traveling up to 310 m.

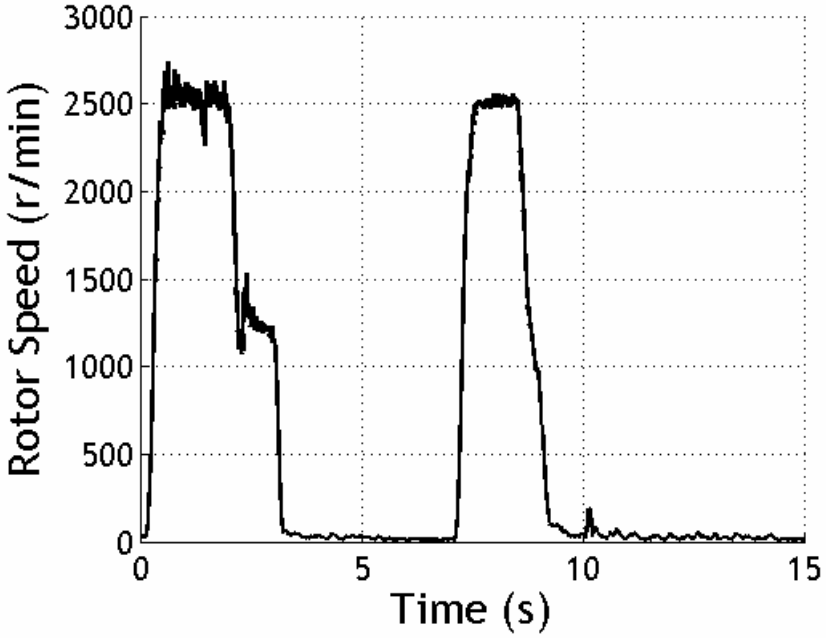

Figure 3.12: Rotor speed versus time

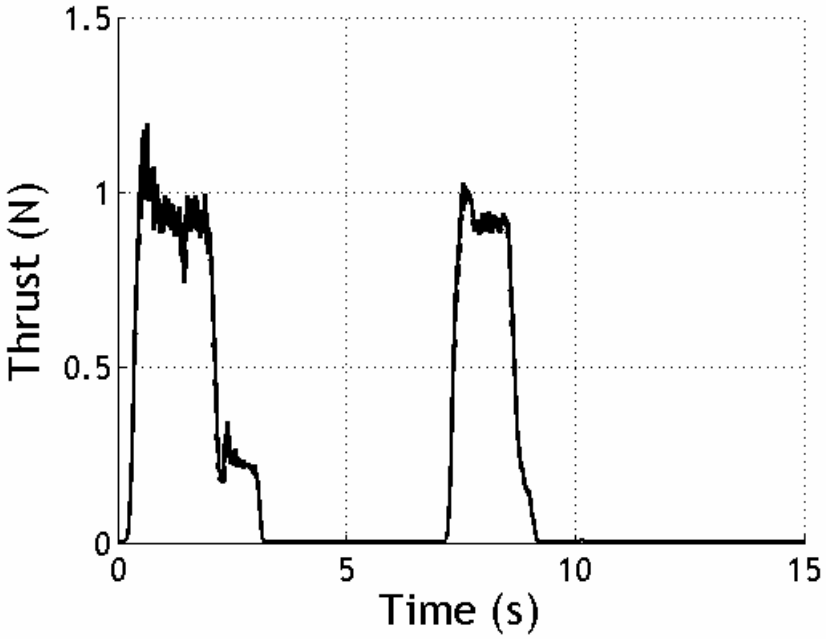

Figure 3.13: Thrust versus time

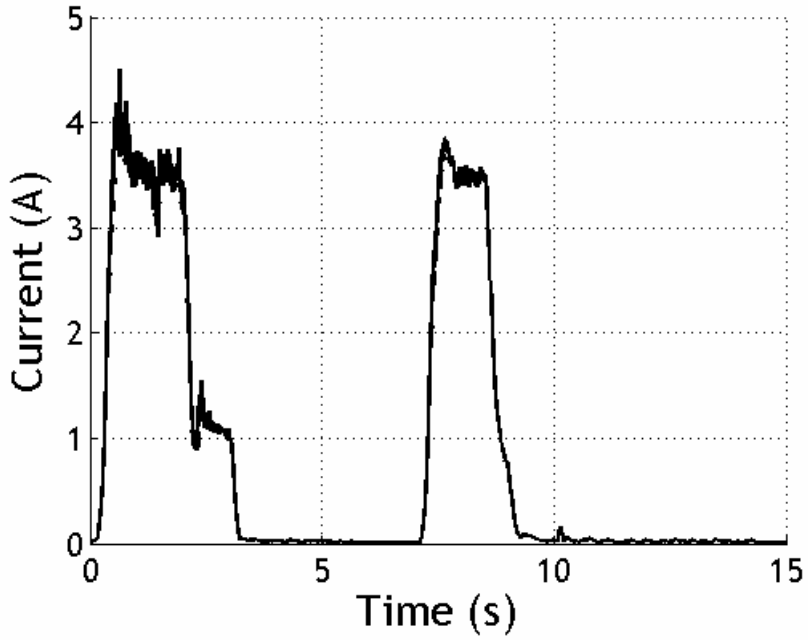

Figure 3.14: Current versus time

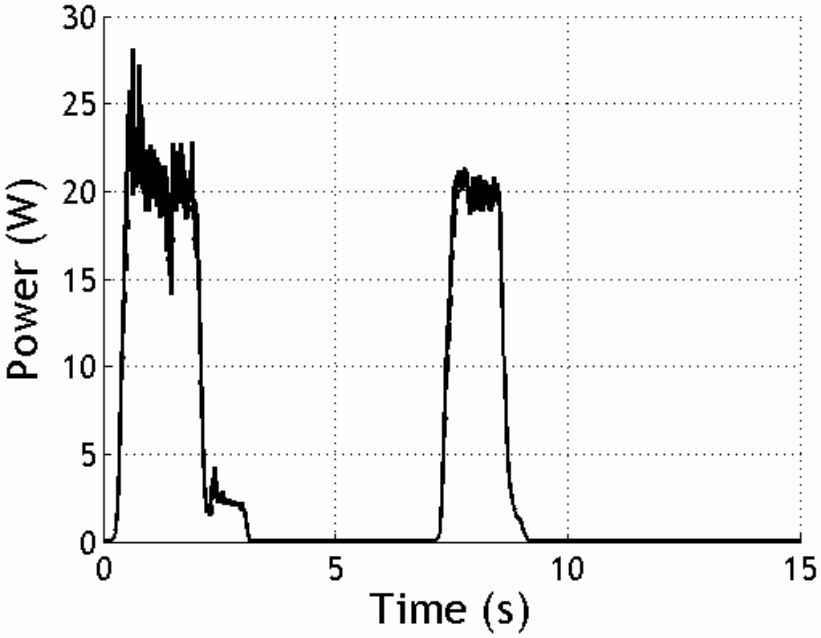

Figure 3.15: Power versus time

Flight tests were also performed in the Indoor Flight Facility with internal masses of different weights to qualitatively evaluate the change in flight performance due to this parameter. Flight tests showed that increasing the internal mass weight effectively decreased the attainable altitude of the vehicle for a given burst duration, but increased the horizontal distance traveled due to the higher initial launch angle and larger pitching moment during flight.

A series of tests were also conducted to evaluate the mobility of the vehicle through cluttered environments and its robustness during ground impact and obstacle collisions. The Hopping Rotochute prototype was able to successfully hop on top of and over tables, desks, and chairs without incurring any significant damage. The vehicle was also flown through doorways and up/down stairs with relative ease. In addition, the prototype was flown outdoors, to the top of a building, across the roof, and landed on the other side. Throughout all these tests, the only malfunctions that occurred were due to a bad soldering job at the electric motor - electronic speed controller junction and the occasional disconnect of the transmission housing from the mounting brackets.

3.3 Discussion

The results of the flight tests demonstrated that the design of the Hopping Rotochute prototype met or exceeded the system requirements set forth in Chapter 1. The vehicle was made small (24.1 × 24.1 × 25.4 cm), lightweight (~80 g), and simple as possible using off-the-shelf components. The use of a movable internal mass for directional control proved to be a viable solution which allowed the vehicle to hop in the desired direction of travel. The vehicle was able to passively self-right itself when in ground contact due to the designed low mass center and egg-shaped body. In fact, by carefully placing the vehicle at any orientation on a flat surface, the vehicle was always able to reorient itself to an upright attitude. One potential problem of the cage design is the possibility of it getting entangled in the limbs of bushes or small trees. This could be

avoided by traveling around or over such obstacles. The vehicle was able to successfully carry small payload of at least 10 g (here VICON markers and the internal mass). Although no sensitive electronic equipment, other than the required electronic components to control and power the vehicle, were incorporated into the design, the requirement of traversing without incurring any damage to the payload is deemed satisfied. If more impact sensitive electronic equipment is carried onboard the Hopping Rotochute, the rotor speed can be reduced rather than ceased which would allow the vehicle to fall slowly to the ground and prevent payload damage. The flight tests demonstrated that the vehicle could jump over 2 m high. Although this might not be the optimum for preserving energy, the vehicle was able to fly to the top of a building approximately 4 m high, double the system requirement. The results of the flight tests also predicted that the vehicle could achieve a total range over 200 m, accumulating a range of 360 m and 310 m associated with the first and second hop profile respectively. The prototype demonstrated the ability to use minimal energy. That is, once the vehicle is hopped into the desired area, the robot has the ability to sit for several hours or even days depending on the amount of energy used during the positioning of the device as well as the energy drawn by the associated electronics. Additional energy would be needed if sensors were incorporated. By using the internal mass to shift the vehicle's center of gravity during flight, the Hopping Rotochute was able to shape simple trajectories via radio control. This feature could be improved by the incorporation of an autopilot.

CHAPTER 4

HOPPING ROTOCHUTE DYNAMIC MODEL

In order to predict the dynamics and flight performance of the Hopping Rotochute, a dynamic model was developed [59]. The purpose of the dynamic model is to allow key parameters to be easily changed in order to explore the design space and to assist in optimizing the flight performance of the vehicle. This chapter outlines the dynamic model of the Hopping Rotochute and its implementation.

A schematic of the Hopping Rotochute system and the reference frames used in the development of the dynamic model are shown in Figure 4.1. The Hopping Rotochute is modeled with six degrees of freedom, including three inertial position components of the total mass center and three Euler orientation angles [60-74]. In addition to the aerodynamic loads that act on the body, a soft contact model is employed to estimate the applied forces during ground contact. The kinematic and dynamic equations of motion are presented below as well as the forces and moments that act on the body.

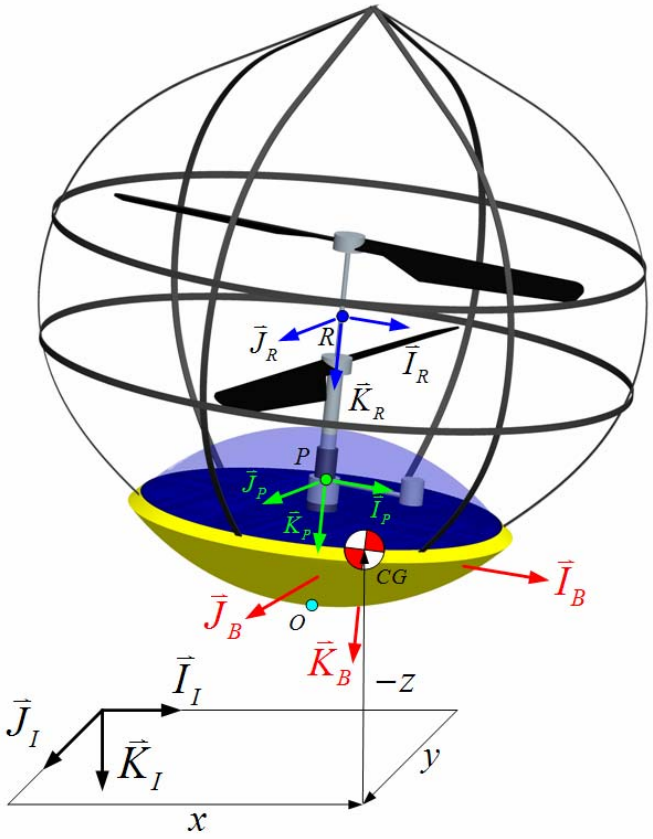

Figure 4.1: Hopping Rotochute schematic

4.1 Equations of Motion

The kinematic equations of motion for the vehicle are provided in equations 4.1 and 4.2

$$\begin{Bmatrix} \dot{x} \\ \dot{y} \\ \dot{z} \end{Bmatrix} = \left[\mathbf{T}_{IB}\right] \begin{Bmatrix} u \\ v \\ w \end{Bmatrix} \tag{4.1}$$

$$\begin{Bmatrix} \dot{\phi} \\ \dot{\theta} \\ \dot{\psi} \end{Bmatrix} = \begin{bmatrix} 1 & s_\phi t_\theta & c_\phi t_\theta \\ 0 & c_\phi & -s_\phi \\ 0 & s_\phi / c_\theta & c_\phi / c_\theta \end{bmatrix} \begin{Bmatrix} p \\ q \\ r \end{Bmatrix} \tag{4.2}$$

where the standard shorthand notation is used for trigonometric functions: $\cos(\alpha) \equiv c_\alpha$, $\sin(\alpha) \equiv s_\alpha$, and $\tan(\alpha) \equiv t_\alpha$. The matrix $\mathbf{T}_{IB}$ represents the transformation matrix from the body reference frame to an inertial reference frame.

$$\mathbf{T}_{IB} = \begin{bmatrix} c_\theta c_\psi & s_\phi s_\theta c_\psi - c_\phi s_\psi & c_\phi s_\theta c_\psi + s_\phi s_\psi \\ c_\theta s_\psi & s_\phi s_\theta s_\psi + c_\phi c_\psi & c_\phi s_\theta s_\psi - s_\phi c_\psi \\ -s_\theta & s_\phi c_\theta & c_\phi c_\theta \end{bmatrix} \tag{4.3}$$

The dynamic equations of motion are formed by summing the forces and moments about the system mass center in the body reference frame and equating the result to the time derivative of linear and angular momentum respectively. The translational and rotational dynamic equations of motion are expressed as

$$\begin{Bmatrix} \dot{u} \\ \dot{v} \\ \dot{w} \end{Bmatrix} = \frac{1}{m} \begin{Bmatrix} X \\ Y \\ Z \end{Bmatrix} - \begin{bmatrix} 0 & -r & q \\ r & 0 & -p \\ -q & p & 0 \end{bmatrix} \begin{Bmatrix} u \\ v \\ w \end{Bmatrix} \tag{4.4}$$

$$\begin{Bmatrix} \dot{p} \\ \dot{q} \\ \dot{r} \end{Bmatrix} = [I]^{-1} \left(\begin{Bmatrix} L \\ M \\ N \end{Bmatrix} - \begin{bmatrix} 0 & -r & q \\ r & 0 & -p \\ -q & p & 0 \end{bmatrix} [I] \begin{Bmatrix} p \\ q \\ r \end{Bmatrix} \right) \tag{4.5}$$

The mass moment of inertia matrix, *I*, is dependent on the location and size of the internal mass. In this thesis work, the internal mass is positioned with respect to the body by a distance d_{IM} along $\vec{I}_P$ from the pivot point *P*. The internal mass frame (*P*) is oriented with respect to the body fixed frame (*B*) using the rotation sequence: ψ_{IM} about the $\vec{K}_B$ axis and then θ_{IM} about the resulting $\vec{J}_P$ axis. Using this rotation sequence, the transformation matrix from the body reference frame to the internal mass reference frame, $\mathbf{T}_{PB}$, can be constructed and is shown in equation 4.6.

$$\mathbf{T}_{PB} = \begin{bmatrix} c_{\psi_{IM}} c_{\theta_{IM}} & s_{\psi_{IM}} c_{\theta_{IM}} & -s_{\theta_{IM}} \\ -s_{\psi_{IM}} & c_{\psi_{IM}} & 0 \\ c_{\psi_{IM}} s_{\theta_{IM}} & s_{\psi_{IM}} s_{\theta_{IM}} & c_{\theta_{IM}} \end{bmatrix} \tag{4.6}$$

Note that although the internal mass on the prototype is only allowed to rotate about the $\vec{K}_B$ axis by ψ_{IM}, the orientation of the internal mass is kept general in the mathematical model.

4.2 Body Forces and Moments

The applied forces and moments expressed in equations 4.4 and 4.5 contain contributions from weight ($_W$), body aerodynamics ($_{BA}$), rotor aerodynamics ($_{RA}$), and contact loads ($_C$). The total forces and moments applied to the vehicle expressed in the body reference frame are given by equations 4.7 and 4.8 respectively.

$$\begin{Bmatrix} X \\ Y \\ Z \end{Bmatrix} = \begin{Bmatrix} X_W + X_{BA} + X_{RA} + X_C \\ Y_W + Y_{BA} + Y_{RA} + Y_C \\ Z_W + Z_{BA} + Z_{RA} + Z_C \end{Bmatrix} \tag{4.7}$$

$$\begin{Bmatrix} L \\ M \\ N \end{Bmatrix} = \begin{Bmatrix} L_{BA} + L_{RA} + L_C \\ M_{BA} + M_{RA} + M_C \\ N_{BA} + N_{RA} + N_C \end{Bmatrix} \tag{4.8}$$

The weight contribution is given by equation 4.9.

$$\begin{Bmatrix} X_W \\ Y_W \\ Z_W \end{Bmatrix} = mg \begin{Bmatrix} -s_\theta \\ s_\phi c_\theta \\ c_\phi c_\theta \end{Bmatrix} \tag{4.9}$$

The body aerodynamic force is calculated assuming that only drag acts on the body at the center of pressure ($_{CP}$) as shown in equation 4.10.

$$\begin{Bmatrix} X_{BA} \\ Y_{BA} \\ Z_{BA} \end{Bmatrix} = -\frac{1}{2}\rho V_{CP} S C_D \begin{Bmatrix} u_{CP} \\ v_{CP} \\ w_{CP} \end{Bmatrix} \tag{4.10}$$

where

$$V_{CP} = \sqrt{u_{CP}^2 + v_{CP}^2 + w_{CP}^2} \tag{4.11}$$

The relative aerodynamic velocity components at the center of pressure are influenced by atmospheric winds as well as the angular velocity of the body. The mean atmospheric wind is assumed to act in the horizontal plane and is directed at an angle ψ_{MW} from the $\vec{I}_I$ axis with a magnitude of V_{MW}. The relative aerodynamic velocity components at the center of pressure expressed in the body reference frame are given as,

$$\begin{Bmatrix} u_{CP} \\ v_{CP} \\ w_{CP} \end{Bmatrix} = \begin{Bmatrix} u \\ v \\ w \end{Bmatrix} + \begin{bmatrix} 0 & -r & q \\ r & 0 & -p \\ -q & p & 0 \end{bmatrix} \begin{Bmatrix} SL_{CG\to CP} \\ BL_{CG\to CP} \\ WL_{CG\to CP} \end{Bmatrix} + \left[\mathbf{T}_{BI}\right] \begin{Bmatrix} V_{MW} c_{\psi_{MW}} \\ V_{MW} s_{\psi_{MW}} \\ 0 \end{Bmatrix} \tag{4.12}$$

Here $SL_{CG\to CP}$, $BL_{CG\to CP}$, and $WL_{CG\to CP}$ represent the components of the position vector from the mass center to the center of pressure of the body along the stationline, buttline, and waterline respectively.

The body aerodynamic moment about the mass center is calculated using

$$\begin{Bmatrix} L_{BA} \\ M_{BA} \\ N_{BA} \end{Bmatrix} = \frac{1}{4}\rho V_{CP} S D^2 \begin{Bmatrix} C_{lp} p \\ C_{mq} q \\ C_{nr} r \end{Bmatrix} + \left[\mathbf{R}_{CG\to CP}\right] \begin{Bmatrix} X_{BA} \\ Y_{BA} \\ Z_{BA} \end{Bmatrix} \tag{4.13}$$

where $\mathbf{R}_{CG\to CP}$ is the skew-symmetric matrix representation of the position vector from the mass center to the center of pressure of the body.

$$\mathbf{R}_{CG\to CP} = \begin{bmatrix} 0 & -WL_{CG\to CP} & BL_{CG\to CP} \\ WL_{CG\to CP} & 0 & -SL_{CG\to CP} \\ -BL_{CG\to CP} & SL_{CG\to CP} & 0 \end{bmatrix} \tag{4.14}$$

The aerodynamic force from the rotor system is given in equation 4.15

$$\begin{Bmatrix} X_{RA} \\ Y_{RA} \\ Z_{RA} \end{Bmatrix} = \left[\mathbf{T}_{BR}\right] \begin{Bmatrix} 0 \\ 0 \\ -T \end{Bmatrix} \tag{4.15}$$

where T is the thrust produced by the rotating rotor system along the $\vec{K}_R$ direction. In this development, the rotor frame (R) is oriented with respect to the body fixed frame (B) using the rotation sequence: θ_R about the $\vec{J}_B$ axis and then ϕ_R about the resulting $\vec{I}_R$ axis. Using this rotation sequence, the transformation matrix from the rotor frame to the body frame, $\mathbf{T}_{BR}$, can be constructed and is shown in equation 4.16.

$$\mathbf{T}_{BR} = \begin{bmatrix} c_{\theta_R} & s_{\phi_R} s_{\theta_R} & c_{\phi_R} s_{\theta_R} \\ 0 & c_{\theta_R} & -s_{\phi_R} \\ -s_{\theta_R} & s_{\phi_R} c_{\theta_R} & c_{\phi_R} c_{\theta_R} \end{bmatrix} \tag{4.16}$$

The rotor blades of the Hopping Rotochute do not instantaneously follow the rotor shaft when the body rotates. To capture this phenomenon, two first order filters are employed to create this lag,

$$\dot{\phi}_F = \frac{\phi - \phi_F}{\tau} \tag{4.17}$$

$$\dot{\theta}_F = \frac{\theta - \theta_F}{\tau} \tag{4.18}$$

The resulting filtered states are used to calculate the values of ϕ_R and θ_R as shown in equations 4.19 and 4.20.

$$\phi_R = \phi_F - \phi \tag{4.19}$$

$$\theta_R = \theta_F - \theta \tag{4.20}$$

The aerodynamic moment from the rotor system is given in equation 4.21.

$$\begin{Bmatrix} L_{RA} \\ M_{RA} \\ N_{RA} \end{Bmatrix} = \left[\mathbf{R}_{CG\to R}\right] \begin{Bmatrix} X_{RA} \\ Y_{RA} \\ Z_{RA} \end{Bmatrix} \tag{4.21}$$

The contact forces and moments that act on the body during ground impact are calculated based on a soft contact model originally developed by Goyal, Pinson, and Sinden [75, 76]. Although other contact models based on hard contact [77-86] and soft contact [87-91] approaches exist, this particular soft contact model was chosen because it permits numerical integration in a timely manner and represents a variety of contact behaviors well. The soft contact model estimates the loads, including Coulomb-like dry friction, by modeling localized non-permanent material deformation of the contacting surfaces. Vertices are used to approximate the exterior shape of the body (a convex polyhedron), while a horizontal plane (face) represents the ground as shown in Figure 4.2. Contact between each body vertex and the ground face occurs through massless rigid planes called surface elements (SEs). During a contact episode, the SEs are constrained to remain parallel to the ground face but can slip against one another. As shown in Figure 4.3, each body vertex (labeled 1) is connected to an associated surface element through two pairs of massless spring and dampers. The normal spring (k_{1n}) and damper (c_{1n}) of each body vertex are constrained along the ground face normal $(\vec{n})$, while the tangential spring (k_{1t}) and damper (c_{1t}) always stay in the ground face plane.

The orientation of the tangential elements in this plane is parallel to the direction of slip between the contacting SEs. A similar arrangement of springs and dampers with constants $k_{2n}, k_{2t}, c_{2n},$ and c_{2t} connects the SEs associated with the ground face (labeled 2 in Figure 4.3).

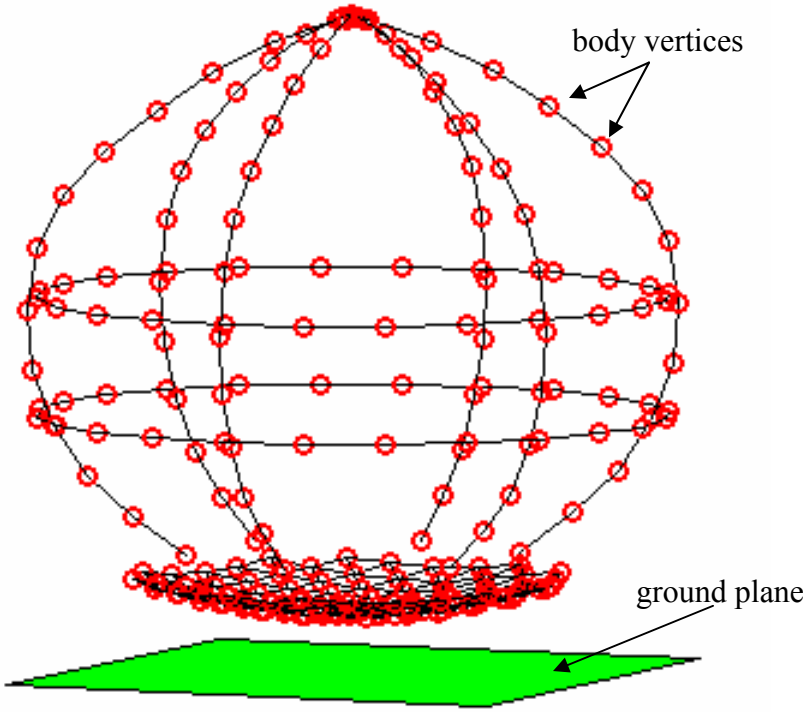

Figure 4.2: Example arrangement of body vertices and ground face for the soft contact model

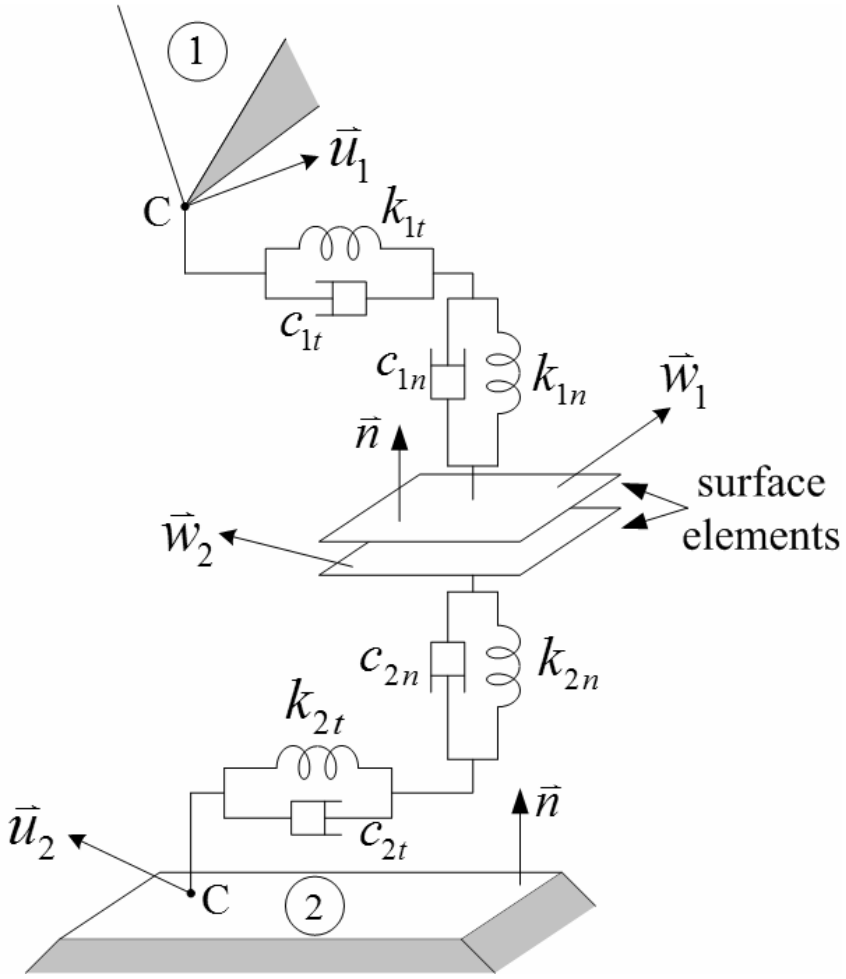

Figure 4.3: Spring and damper schematic for the soft contact model

During simulation, a collision detection method determines which body vertices are contacting the ground face and the point of application (point C in Figure 4.3). Each contact point has two force components, including a normal component $\left(\vec{F}_n\right)$ along $\vec{n}$ and a frictional component $\left(\vec{F}_t\right)$ in the tangential plane of contact. The normal and tangential force from each contact point is given in equations 4.22 and 4.23 respectively, where $\vec{s}_{1n}$ and $\vec{s}_{2n}$ are the distance vectors of the normal springs and $\vec{s}_{1t}$ and $\vec{s}_{2t}$ are the distance vectors of the tangential springs.

$$\vec{F}_n = -k_{1n}\vec{s}_{1n} - c_{1n}\dot{\vec{s}}_{1n} = -k_{2n}\vec{s}_{2n} - c_{2n}\dot{\vec{s}}_{2n} \tag{4.22}$$

$$\vec{F}_t = -k_{1t}\vec{s}_{1t} - c_{1t}\dot{\vec{s}}_{1t} = -k_{2t}\vec{s}_{2t} - c_{2t}\dot{\vec{s}}_{2t} \tag{4.23}$$

The rate of change of the springs are expressed in equations 4.24 and 4.25

$$\dot{\vec{s}}_{1n} = \vec{u}_{1n} - \vec{w}_{1n} \qquad \dot{\vec{s}}_{2n} = \vec{u}_{2n} - \vec{w}_{2n} \tag{4.24}$$

$$\dot{\vec{s}}_{1t} = \vec{u}_{1t} - \vec{w}_{1t} \qquad \dot{\vec{s}}_{2t} = \vec{u}_{2t} - \vec{w}_{2t} \tag{4.25}$$

where $\vec{u}_1$ and $\vec{u}_2$ are the absolute velocities of the contact point on the body and on the ground respectively while $\vec{w}_1$ and $\vec{w}_1$ are the absolute velocities of the two SEs. In this development, $\Delta\vec{u} = \vec{u}_1 - \vec{u}_2$, $\Delta\vec{w} = \vec{w}_1 - \vec{w}_2$, and $\Delta\vec{w}_n = 0$ since no relative motion is allowed between the SEs along $\vec{n}$. Substituting these equations into equations 4.24 and 4.25 yields

$$\dot{\vec{s}}_{1n} - \dot{\vec{s}}_{2n} = \Delta\vec{u}_n \qquad \dot{\vec{s}}_{1t} - \dot{\vec{s}}_{2t} = \Delta\vec{u}_t - \Delta\vec{w}_t \tag{4.26}$$

The contact force of a contact point in the normal direction and the tangential plane is formed by manipulating equations 4.22, 4.23, and 4.26 to yield

$$\vec{F}_n = -\vec{b}_n \tag{4.27}$$

$$\vec{F}_t = -\vec{b}_t + c^*\Delta\vec{w}_t \tag{4.28}$$

where

$$c^* = \frac{c_{1t}c_{2t}}{c_{1t} + c_{2t}} \tag{4.29}$$

$$\vec{b}_n = \frac{1}{c_{1n} + c_{2n}}\left(c_{2n}k_{1n}\vec{s}_{1n} - c_{1n}k_{2n}\vec{s}_{2n} + c_{1n}c_{2n}\Delta\vec{u}_n\right) \tag{4.30}$$

$$\vec{b}_t = \frac{1}{c_{1t} + c_{2t}} \left(c_{2t} k_{1t} \vec{s}_{1t} - c_{1t} k_{2t} \vec{s}_{2t} + c_{1t} c_{2t} \Delta \vec{u}_t \right) \tag{4.31}$$

With the coefficient of friction between the two surfaces denoted as μ and λ a non-negative real variable, the friction law can be expressed as

$$\left| \vec{F}_t \right| \le \mu \left| \vec{F}_n \right| \qquad \Delta \vec{w}_t = -\lambda \vec{F}_t \qquad \lambda \ge 0 \tag{4.32}$$

Substituting equations 4.27 and 4.28 into equation 4.32 results in,

$$\frac{\left| \vec{b}_t \right|}{\left(1 + \lambda c^* \right)} \le \mu \left| \vec{b}_n \right| \tag{4.33}$$

A state of stick exists between the two surface elements when $\left| \vec{b}_t \right| \le \mu \left| \vec{b}_n \right|$. While in a state of stick, $\lambda = 0$ and $\Delta \vec{w}_t = 0$ which from equation 4.28 implies that $\vec{F}_t = -\vec{b}_t$. If, on the other hand, $\left| \vec{b}_t \right| > \mu \left| \vec{b}_n \right|$, the value of that makes equation 4.33 an equality is,

$$\lambda = \frac{\left| \vec{b}_t \right| - \mu \left| \vec{b}_n \right|}{c^* \mu \left| \vec{b}_n \right|} \tag{4.34}$$

In this case $\Delta \vec{w}_t$ and $\vec{F}_t$ can be calculated using equations 4.28 and 4.32 using the value of λ calculated from equation 4.34.

$$\Delta \vec{w}_t = \frac{\lambda \vec{b}_t}{\left(1 + \lambda c^* \right)} \tag{4.35}$$

$$\vec{F}_t = \frac{-\vec{b}_t}{\left(1 + \lambda c^* \right)} \tag{4.36}$$

The total contact force applied to the body in the body reference frame is calculated by summing the forces produced at each contact point as given in equation 4.37.

$$\begin{Bmatrix} X_C \\ Y_C \\ Z_C \end{Bmatrix} = [\mathbf{T}_{BI}] \sum_{C=1}^{NC} \left(\begin{Bmatrix} F_{n_x} + F_{t_x} \\ F_{n_y} + F_{t_y} \\ F_{n_z} + F_{t_z} \end{Bmatrix} \right) \tag{4.37}$$

where *NC* is the number of contact points. The moment about the mass center produced by the contact is calculated by crossing the distance vector from the mass center to each contact point with the force exerted at that contact point as shown in equation 4.38.

$$\begin{Bmatrix} L_C \\ M_C \\ N_C \end{Bmatrix} = \sum_{C=1}^{NC} \left([\mathbf{R}_{CG \to C}][\mathbf{T}_{BI}] \begin{Bmatrix} F_{n_x} + F_{t_x} \\ F_{n_y} + F_{t_y} \\ F_{n_z} + F_{t_z} \end{Bmatrix} \right) \tag{4.38}$$

The state of the springs in the contact mechanism are tracked with the following differential equations, obtained from equations 4.22, 4.23, and 4.26.

$$\dot{\vec{s}}_{1n} = \frac{c_{2n}}{c_{1n} + c_{2n}} \Delta \vec{u}_n - \frac{1}{c_{1n} + c_{2n}} \left(k_{1n} \vec{s}_{1n} + k_{2n} \vec{s}_{2n} \right) \tag{4.39}$$

$$\dot{\vec{s}}_{2n} = \frac{-c_{1n}}{c_{1n} + c_{2n}} \Delta \vec{u}_n - \frac{1}{c_{1n} + c_{2n}} \left(k_{1n} \vec{s}_{1n} + k_{2n} \vec{s}_{2n} \right) \tag{4.40}$$

$$\dot{\vec{s}}_{1t} = \frac{c_{2t}}{c_{1t} + c_{2t}} \left(\Delta \vec{u}_t - \Delta \vec{w}_t \right) - \frac{1}{c_{1t} + c_{2t}} \left(k_{1t} \vec{s}_{1t} + k_{2t} \vec{s}_{2t} \right) \tag{4.41}$$

$$\dot{\vec{s}}_{2t} = \frac{-c_{1t}}{c_{1t} + c_{2t}} \left(\Delta \vec{u}_t - \Delta \vec{w}_t \right) - \frac{1}{c_{1t} + c_{2t}} \left(k_{1t} \vec{s}_{1t} + k_{2t} \vec{s}_{2t} \right) \tag{4.42}$$

4.3 Discussion

During this study 223 vertices were used to approximate the exterior shape of the Hopping Rotochute body. Based on this, the simulation tracks 2690 states by numerically integrating the dynamic equations given in equations 4.1, 4.2, 4.4, 4.5, 4.17, 4.18, 4.39, 4.40, 4.41, and 4.42 using a 4^{th} order Runge-Kutta algorithm. Of course during the simulation not all of the body vertices are in contact with the ground. A collision detection method, based on linear interpolation, was implemented to determine when a new contact appeared or an existing contact disappeared (broken) during an integration interval. The collision detection method backs up the simulation to the time and states of the Hopping Rotochute when the new or broken contact took place and changes the time step appropriately. While in ground contact, the time step was set to 0.01 ms to capture the dynamics of the high-frequency model response while the contact forces and moments were calculated using equations 4.37 and 4.38 respectively. While the device was airborne, no contact points existed, the time step was set to 0.1 ms, and no contact forces or moments were applied to the body.

CHAPTER 5

VALIDATION OF THE DYNAMIC MODEL

The dynamic model described in Chapter 4 is based on several assumptions and contains several parameters which must be determined. In order to use the model with confidence to predict the dynamics and flight performance of the Hopping Rotochute, these parameters need to be determined and the dynamic model must be validated. This chapter focuses on the instrumentation used to measure the motion of the Hopping Rotochute prototype, the procedures used to determine the unknown parameters, and the validation results. The purpose of the validation process is to assess the accuracy of the dynamic model and hence the accuracy of the flight performance results.

5.1 Motion Measurement System

Throughout this thesis work, the motion of the Hopping Rotochute prototype and the drop test stand were measured using a motion capture system [92-94] and subsequently used to determine unknown parameters and characteristics. More specifically, these motions were experimentally obtained using a 3-D optical position analysis system from VICON Motion Systems [92, 95] which has proven itself in a variety of settings [96-101]. The twelve camera motion capture system is housed in the Indoor Flight Facility (IFF) at Georgia Tech which is 7.6 m wide, 8.5 m long, and 3.6 m high. As shown in Figure 5.1, the cameras are strategically arranged around the room so the capture volume can encompass the entire room. Two cameras are located at each corner of the room while a single camera is situated in the middle of each of the four walls. The cameras emit and collect visible infrared light at a frequency up to 2000

frames/s from spherical retro-reflective markers that are rigidly attached to the object of choice. Optical correlation techniques are employed to determine the three-dimensional position of the center of each marker to within 1 mm accuracy in real time. The time stamped data is stored in a text file and is subsequently used to determine the position, orientation, velocity, and angular velocity of the body.

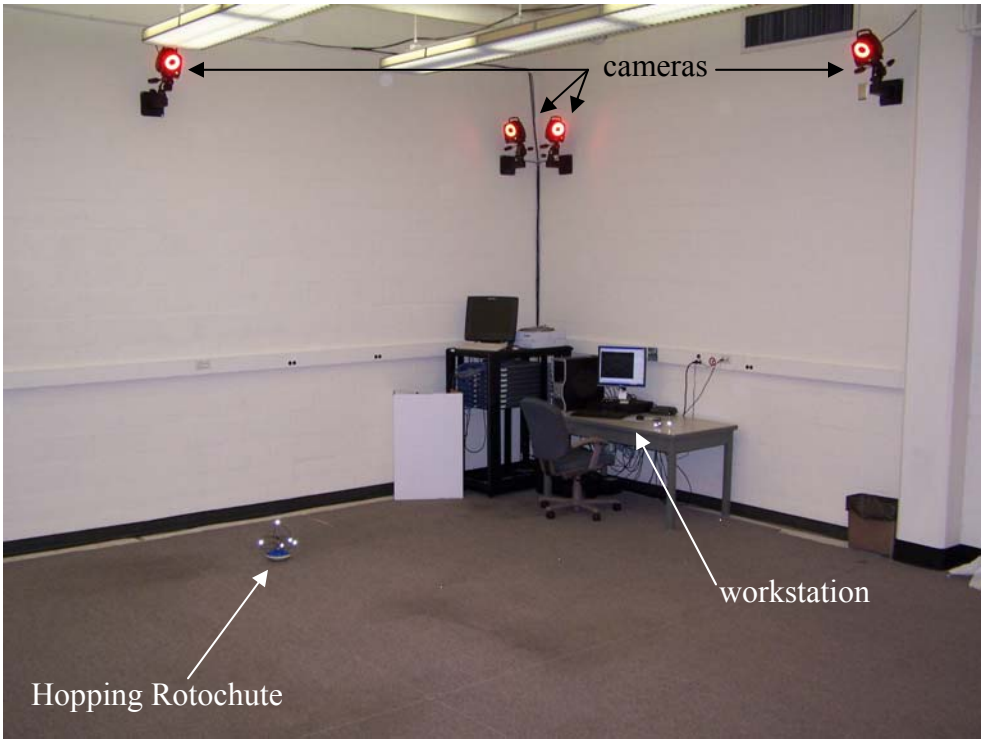

Figure 5.1: Indoor Flight Facility with VICON motion capture system

To capture the motion of the drop test stand, three 14 mm diameter markers were rigidly attached to the slider; one at the top and two at the bottom as shown in Figure 2.14 a). The capture rate of the cameras was set to 120 frames/s during the drop tests which was more than fast enough to capture the dynamics of the device.

As shown in Figure 5.2, six 9 mm diameter markers were used during the experimental testing of the Hopping Rotochute prototype. Three of the markers were rigidly attached to the base, two were secured to the lower rotor shaft, and the other was placed on top of the cage. A camera capture rate of 500 frames/s was used to measure the motion of the Hopping Rotochute prototype body and lower rotor shaft.

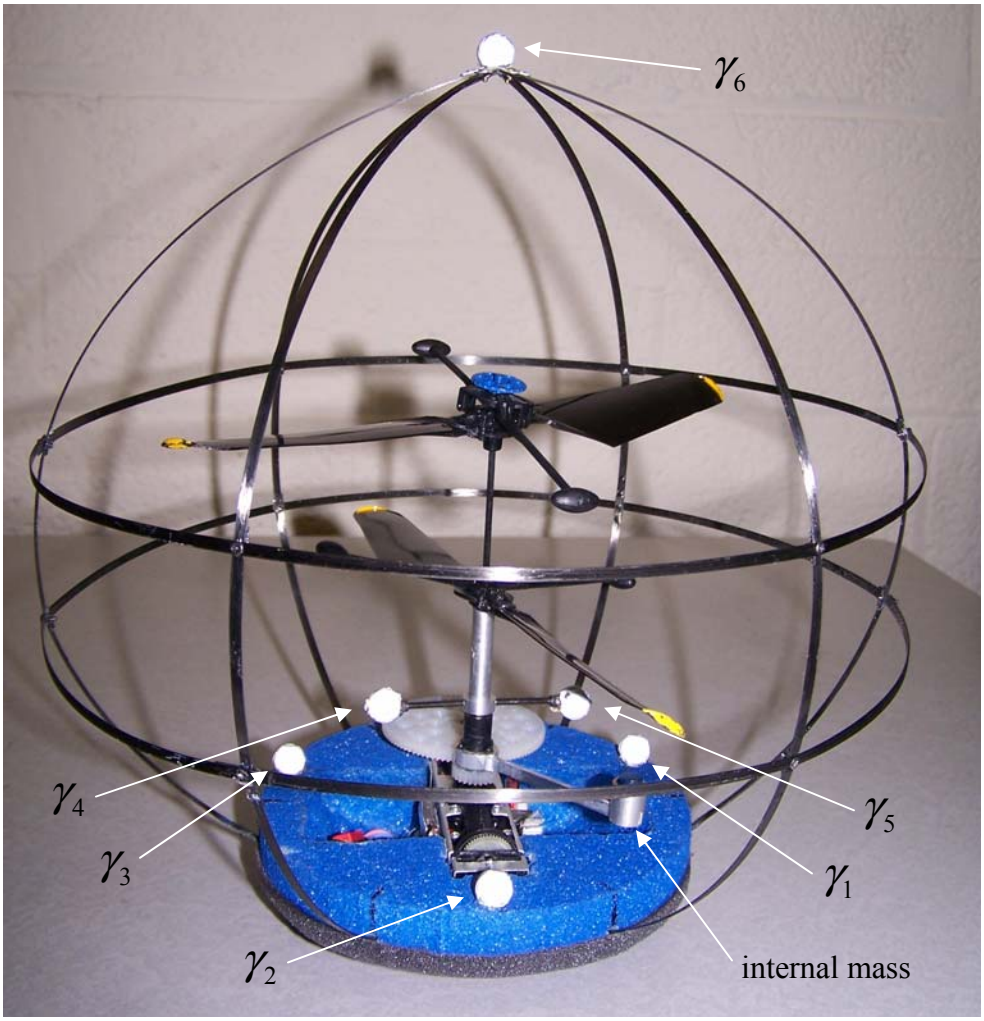

Figure 5.2: Hopping Rotochute prototype with VICON markers

In order to generate the mass center position and orientation of a body, the marker position data is processed to generate the transformation matrix from the body reference frame to an inertial frame. To illustrate this process, consider the markers labeled γ_1, γ_2, and γ_3 attached to the base of the Hopping Rotochute prototype shown in Figure 5.2. The body reference frame unit vectors are defined such that the $\vec{J}_B$ axis points laterally from marker γ_1 to γ_3, the $\vec{K}_B$ axis points vertically downward, and the $\vec{I}_B$ axis points forward (normal to the plane created by the $\vec{J}_B$ and $\vec{K}_B$ axes). Mathematically, these three markers are used to define the body reference frame using equations 5.1 through 5.3.

$$\vec{J}_B = \frac{\vec{r}_{O\to\gamma_3} - \vec{r}_{O\to\gamma_1}}{\left\|\vec{r}_{O\to\gamma_3} - \vec{r}_{O\to\gamma_1}\right\|} = j_{Bx}\vec{I}_I + j_{By}\vec{J}_I + j_{Bz}\vec{K}_I \tag{5.1}$$

$$\vec{K}_B = \frac{\left(\vec{r}_{O\to\gamma_2} - \vec{r}_{O\to\gamma_1}\right)\times\vec{J}_B}{\left\|\left(\vec{r}_{O\to\gamma_2} - \vec{r}_{O\to\gamma_1}\right)\times\vec{J}_B\right\|} = k_{Bx}\vec{I}_I + k_{By}\vec{J}_I + k_{Bz}\vec{K}_I \tag{5.2}$$

$$\vec{I}_B = \frac{\vec{J}_B\times\vec{K}_B}{\left\|\vec{J}_B\times\vec{K}_B\right\|} = i_{Bx}\vec{I}_I + i_{By}\vec{J}_I + i_{Bz}\vec{K}_I \tag{5.3}$$

Note that the body reference frame and the inertial reference frame unit vectors are related by equation 5.4.

$$\begin{Bmatrix}\vec{I}_B\\ \vec{J}_B\\ \vec{K}_B\end{Bmatrix} = \left[\mathbf{T}_{BI}\right]\begin{Bmatrix}\vec{I}_I\\ \vec{J}_I\\ \vec{K}_I\end{Bmatrix} \tag{5.4}$$

Using this relationship and equating components resolved in the inertial frame yields,

$$\begin{bmatrix} i_{Bx} & j_{Bx} & k_{Bx} \\ i_{By} & j_{By} & k_{By} \\ i_{Bz} & j_{Bz} & k_{Bz} \end{bmatrix} = \left[\mathbf{T}_{IB}\right] \tag{5.5}$$

The Euler orientation angles of the body are obtained by comparing the functional form of the transformation matrix in equation 4.3 with the measured transformation matrix in equation 5.5, yielding

$$\theta = -\sin^{-1}\left(i_{Bz}\right) \tag{5.6}$$

$$\phi = \tan^{-1}\left(\frac{j_{Bz}}{k_{Bz}}\right) \tag{5.7}$$

$$\psi = \tan^{-1}\left(\frac{i_{By}}{i_{Bx}}\right) \tag{5.8}$$

The position and orientation data are numerically differentiated using a second-order finite difference method and a running average with a 10-sample window size is implemented to reduce noise amplification. The results of this procedure are substituted into equations 4.1 and 4.2 to obtain the components of the linear and angular velocities in the body reference frame. A similar approach is taken to calculate rotor speed using the markers labeled γ_4, γ_5, and γ_6 in Figure 5.2. The same procedure is also used to determine the position and velocity of the drop test stand's slider.

5.2 Ground Contact Validation

The soft contact model requires the values of the spring constants (*k*) and damper coefficients (*c*) of both the polyurethane foam cushion material on the bottom of the Hopping Rotochute and the carpet covering the ground of the IFF. In addition, the

coefficient of friction, μ, is needed between these two materials. Three different procedures were used for the determination of these material characteristics. In order to find the spring constants, material samples were tested as described in Chapter 2.2.3. The spring constants were determined to be approximately 12,120 N/m for the polyurethane foam and 6,800 N/m for the carpet. These spring constants assume that only one vertex exists for the sample material area of 20.3 cm^2. Since the contact model consists of many vertices which are approximately equal distance from each other, there are more vertices per area. To incorporate this into the model, an equivalent spring constant is calculated based on the vertex spacing. A plot of the equivalent spring constant as a function of vertex spacing is given in Figure 5.3 for the polyurethane and carpet material. During this study, a vertex spacing of 6.9 mm was used which gives an equivalent spring constant of 212 N/m for the polyurethane foam and 120 N/m for the carpet as shown in Table 5.1.

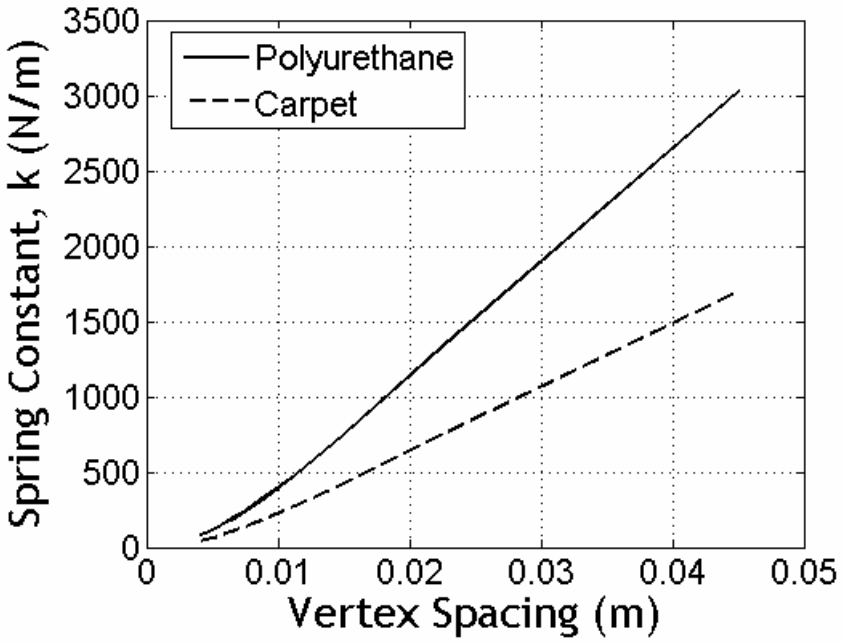

Figure 5.3: Polyurethane and carpet spring constants versus vertex spacing

Table 5.1: Material properties

Parameter	Value	Units	Material(s)
k_{1n}, k_{1t}	212, 212	N/m	polyurethane
c_{1n}, c_{1t}	0.5, 0.5	N·s/m	polyurethane
k_{2n}, k_{2t}	120, 120	N/m	carpet
c_{2n}, c_{2t}	0.5, 0.5	N·s/m	carpet
μ	3.0	-	polyurethane/carpet

To obtain the damping coefficients of each material, the drop test stand was employed as described in Chapter 2.2.3. The motion was recorded by the motion capture system and subsequently compared with simulation results using the same initial conditions and mass properties as well as the spring constants from the test previously described. The damping coefficients were adjusted until the experimental trajectory matched the simulation results. The damping coefficient along the normal and tangential directions associated with a vertex spacing of 6.9 mm was determined to be 0.5 N·s/m for both the polyurethane and the carpet as outlined in Table 5.1. The drop test stand was also used to drop a polyurethane foam sample onto a carpet sample. The data recorded from this test was compared to simulation results using the spring constants and damping coefficients outlined above. The comparison is given in Figure 5.4 which plots the altitude as a function of time. Here the solid line represents the data from the motion capture system (experimental) and the dashed line is the simulated time history (theoretical). A shown, the theoretical and experimental results correlate very well.

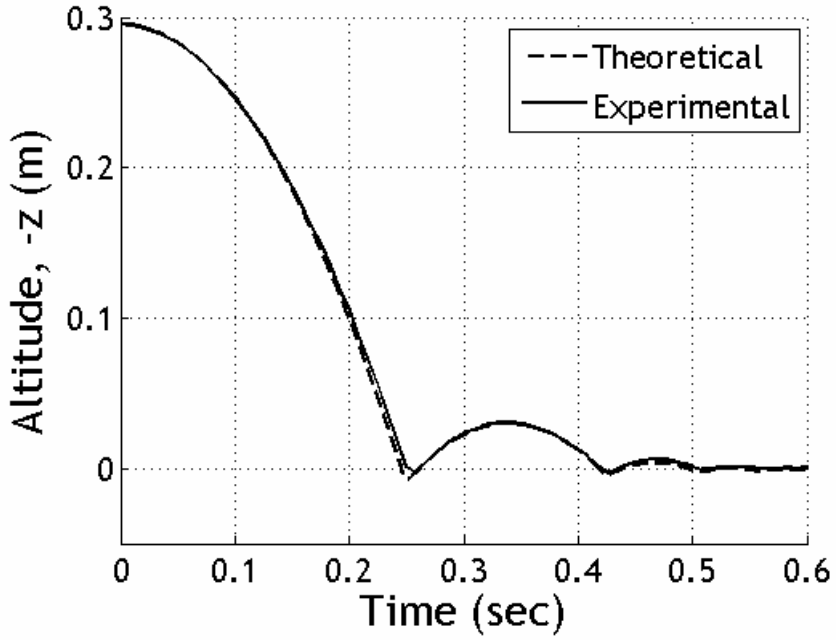

Figure 5.4: Altitude versus time associated with drop test stand

The coefficient of friction was obtained by placing a mass of known weight on a polyurethane foam sample and moving it at a constant speed across the carpet while measuring the force as shown in Figure 5.5. Using the friction law,

$$F = \mu N \tag{5.9}$$

the coefficient of friction between the polyurethane foam and the carpet was calculated to be approximately 3.0.

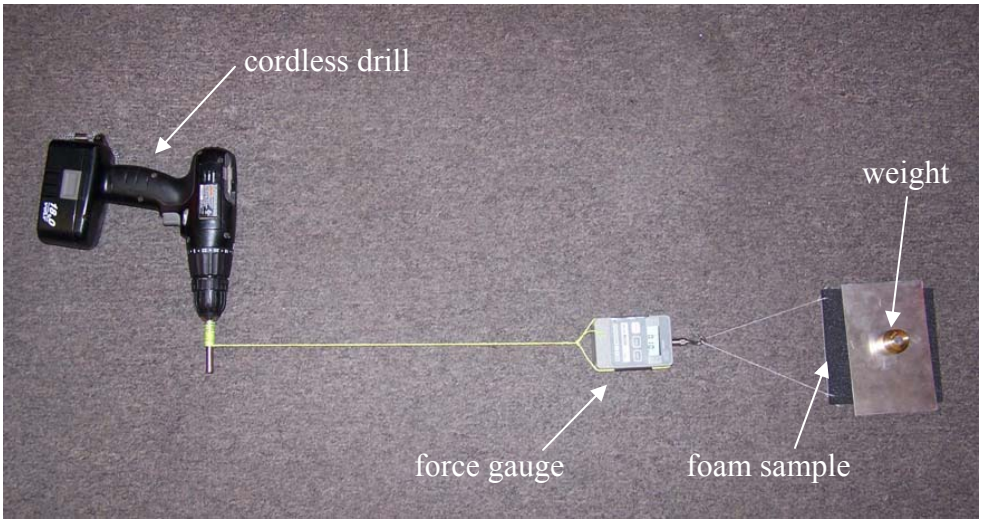

Figure 5.5: Friction test setup

With the contact model parameters determined, the motion of the Hopping Rotochute prototype was captured and compared to the dynamic model simulation results to determine the validity of the soft contact model. The prototype was dropped from a height of 1.2 m without applying power to the rotor system and the motion was recorded using the motion capture system. The same drop was simulated with the experimentally tuned dynamic model using the same initial conditions and the results are shown in Figure 5.6 through 5.9 where the solid line and dashed line represent the captured (experimental) and simulated (theoretical) data respectively. As shown in Figure 5.6, the Hopping Rotochute prototype bounces to a height of about 13 cm after ground impact while the simulation predicts a height of 14 cm. Figure 5.7 demonstrates that the general behavior of the range and cross range motion is predicted by the simulation, although the simulated drop does not travel as far in the horizontal plane. Figures 5.8 and 5.9 present the roll and pitch angles as a function of time. As shown, the initial impact rolls the

prototype up to about 6.2 deg while pitching it to 13 deg. The simulation, on the other hand, predicts values of 7.5 and 17 deg respectively. Figures 5.8 and 5.9 also demonstrate that the frequency and damping ratio of the simulated rolling and pitching oscillations agree with the captured motion when in ground contact.

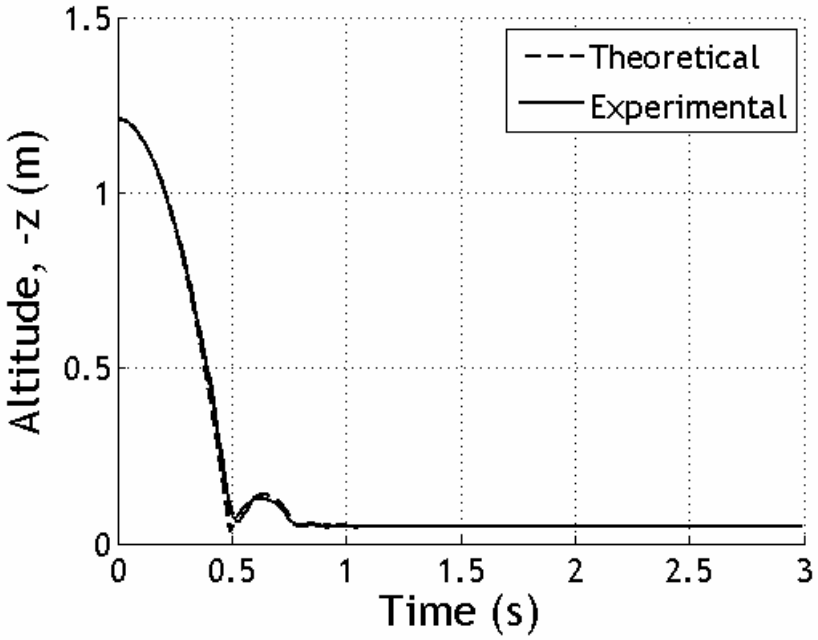

Figure 5.6: Drop test altitude versus time

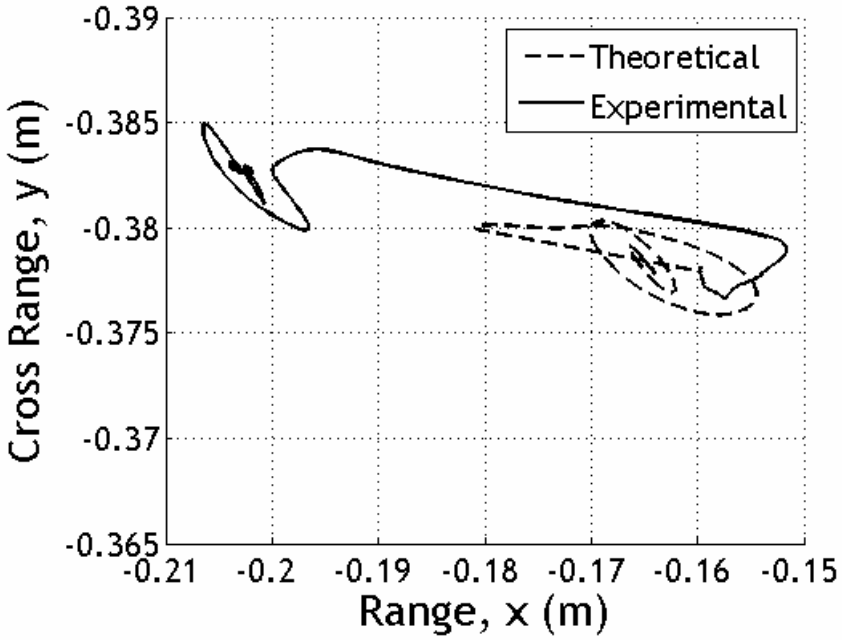

Figure 5.7: Drop test cross range versus range

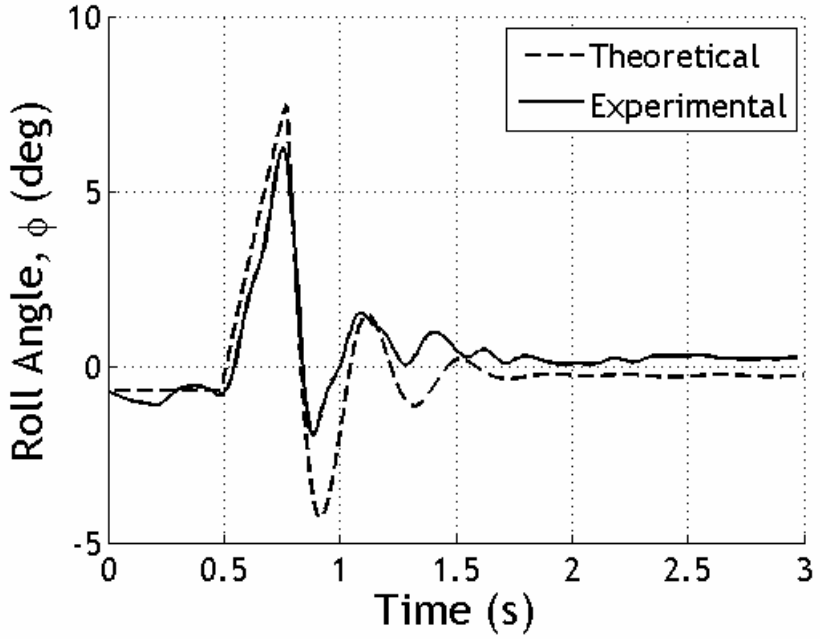

Figure 5.8: Drop test roll angle versus time

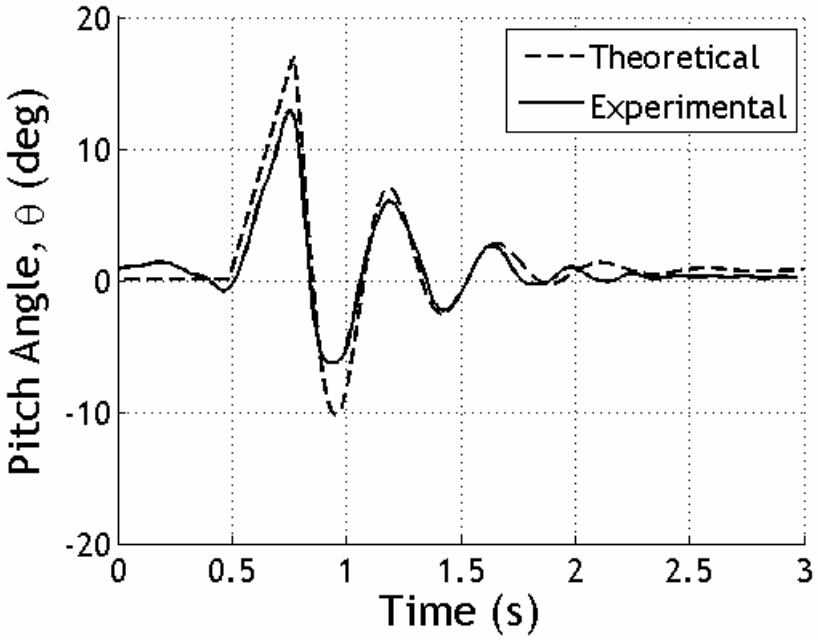

Figure 5.9: Drop test pitch angle versus time

5.3 Flight Dynamic Validation

The Hopping Rotochute dynamic model includes rotor and body aerodynamic loads which must be characterized. The aerodynamic properties of the rotor system were obtained via a rotor test stand (Chapter 3.1). The rotor lag time constant was experimentally obtained by video-taping the powered rotor system while the prototype was pitched quickly by 90 deg about a point on the base. The pitch angle of the body and the angle of the tip path plane were measured throughout the time-stamped video footage and this data was compared to the results of a first order filter to determine the time constant. The rotor lag time constant was found to be approximately 0.17 s. The body aerodynamic coefficients and center of pressure were obtained by analyzing data collected from the motion capture system and performing a force and moment balance to

determine these unknowns. During powered flight, the drag coefficient was determined to be 1.0 and the center of pressure was calculated to be approximately -9.4 cm along $\vec{K}_B$ from point O $\left(WL_{O\to CP} = -9.4 \text{ cm}\right)$ which is right below the lower rotor blades. Note that this aerodynamic force accounts for the additional drag on the body while the rotors are spinning since download is already captured by the results of the rotor test stand experiment. The body aerodynamic drag coefficient and center of pressure during unpowered flight was determined to be 0.6 and -6.4 cm along $\vec{K}_B$ from point O $\left(WL_{O\to CP} = -6.4 \text{ cm}\right)$. The aerodynamic damping moment coefficients were experimentally determined to be approximately -0.3. The aerodynamic properties of the Hopping Rotochute are tabulated in Table 5.2.

Table 5.2: Aerodynamic properties

Parameter	Value	Units
C_D (powered flight)	1.0	-
$WL_{O\to CP}$ (powered flight)	-9.4	cm
C_D (unpowered flight)	0.6	-
$WL_{O\to CP}$ (unpowered flight)	-6.4	cm
C_{lp}, C_{mq}, C_{nr}	-0.3, -0.3, -0.3	-
D	25.4	cm
S	506.7	cm^2
τ	0.17	s

In order to validate the flight dynamics part of the Hopping Rotochute model, the motion capture system was employed to record an example hop and the results were

compared to simulation results which incorporated the same initial conditions and the model parameters described above in Table 5.2. The time histories of the example hop recorded by the motion capture system as well as the results from the simulation are shown in Figures 5.10 through 5.19. In these charts, the solid line represents the data from the motion capture system (experimental) and the dashed line represents the simulated results (theoretical). As shown in Figures 5.10 through 5.13, the mass center position versus time associated with the captured and simulated results correlate well. For this particular hop, the Hopping Rotochute reached a maximum altitude of about 77 cm at 1.6 s while achieving a total range of 1.73 m associated with the captured data and 1.57 m for the simulated results. The pitch angle versus time is given in Figure 5.14. The captured pitch angle increases to a value of 8.5 deg whereas the simulated pitch angle reaches a maximum of 14.5 deg before rapidly decreasing after 1.5 s while the vehicle is unpowered. Although the recorded pitch angle is consistently lower than that resulting from the simulation, the general trend is captured. Figures 5.15 and 5.16 compare forward and vertical velocities of the captured and simulated motion respectively. The forward velocity decreases almost linearly to a value of -1.6 m/s associated with the captured data and -1.66 m/s for the simulated result while the vehicle is powered and subsequently increases once the power is ceased. The vertical velocity exponentially decreases and plateaus at approximately -0.9 m/s before rapidly increasing when unpowered until ground impact occurs. Figure 5.17 presents the rotor speed profiles associated with the captured and simulated data. The captured rotor speed is conservative and has a time lag when compared to the simulated rotor speed due to marker exclusions and the calculation routine. The simulated rotor speed ramps up to

2540 r/min whereas the captured rotor speed achieves a maximum average value of 2420 r/min. Since the rotor thrust and power are based on the rotor speed profile, the same type of amplitude and time lag trends occur for these time histories as presented in Figures 5.18 and 5.19. As shown, the thrust and power initially peak due to the high rotor speed and in-ground-effect and then level off before returning back to zero. The maximum thrust and power associated with the simulated result occur at 0.26 s with value of 1.17 N and 22.2 W respectively. The above comparisons between measured and simulated motion of the Hopping Rotochute show that the reported dynamic simulation replicated the major dynamic features of the physical system and is sufficiently accurate to predict performance trends and characteristics as a function of design parameters.

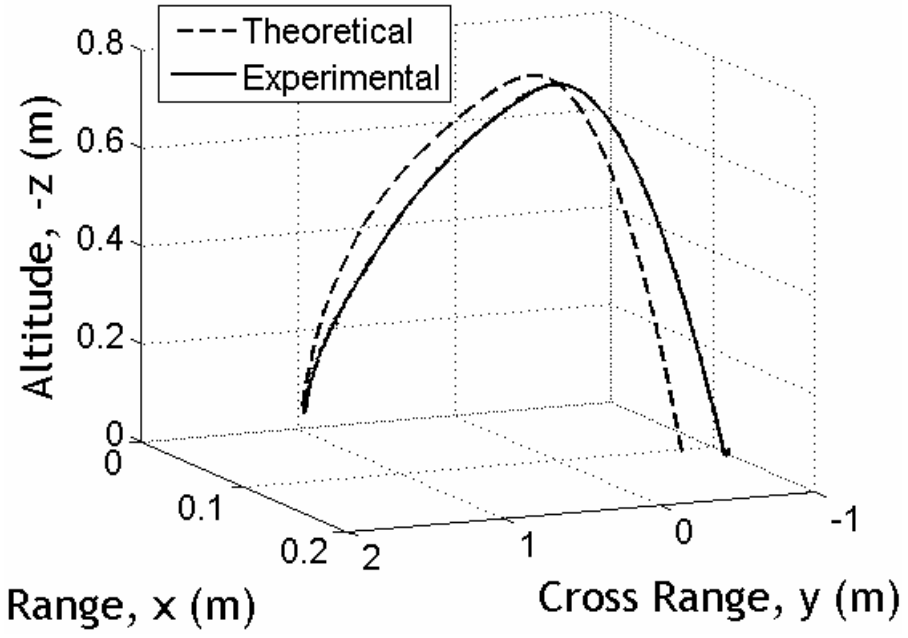

Figure 5.10: Flight test altitude versus cross range versus range

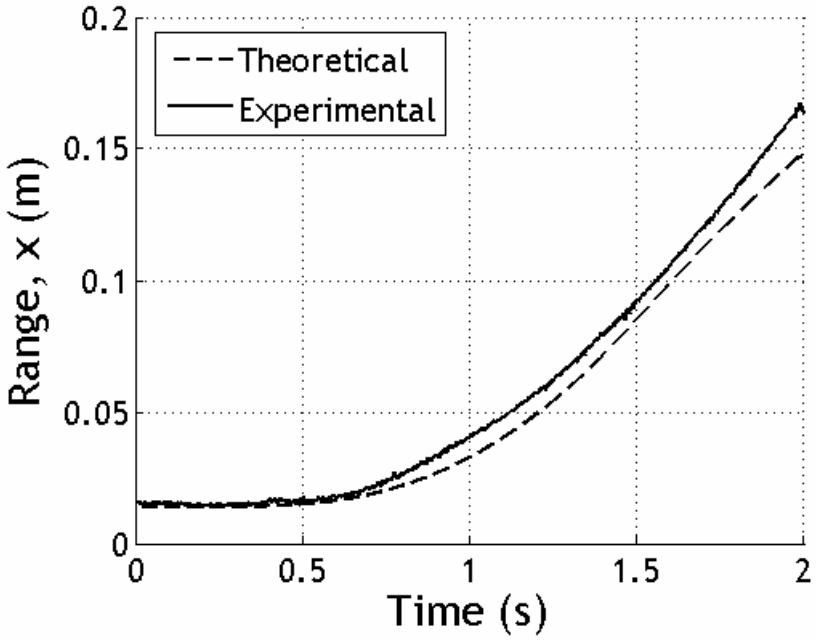

Figure 5.11: Flight test range versus time

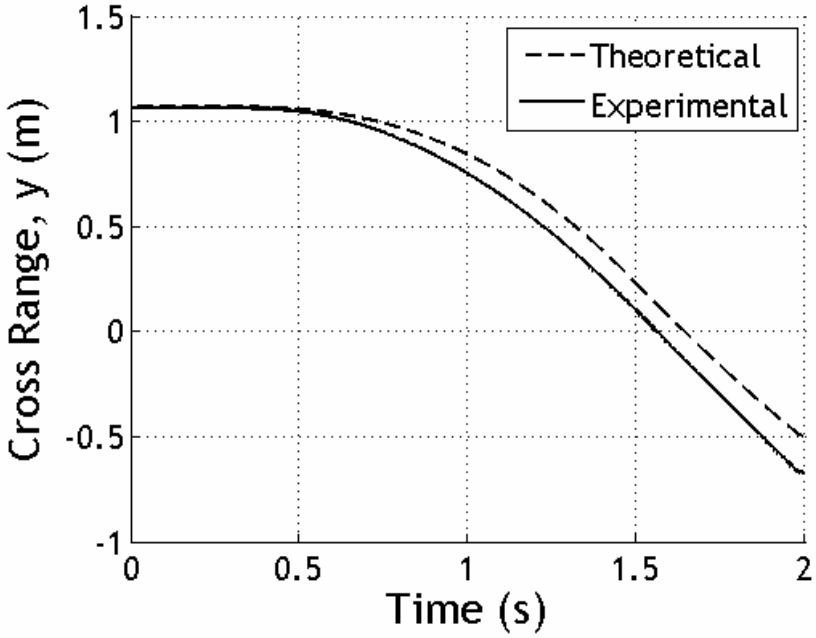

Figure 5.12: Flight test cross range versus time

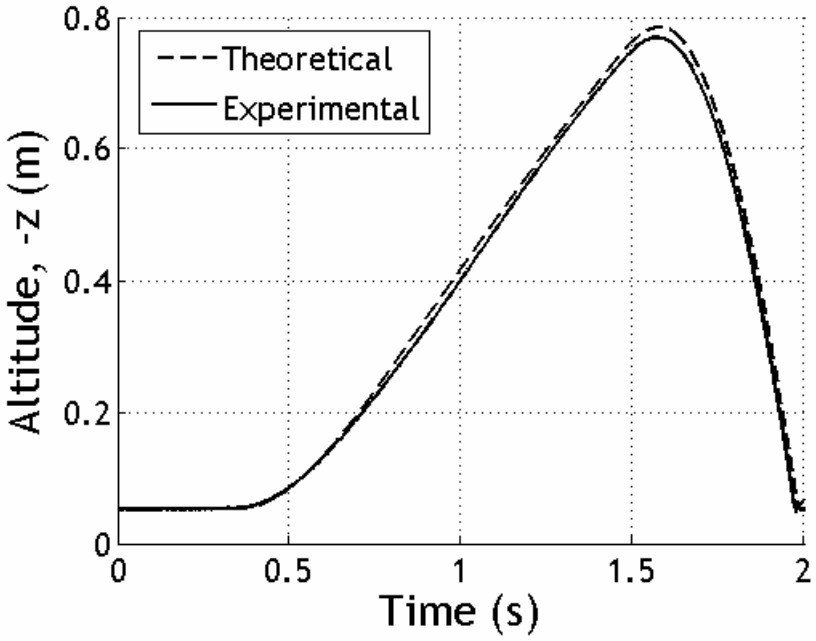

Figure 5.13: Flight test altitude versus time

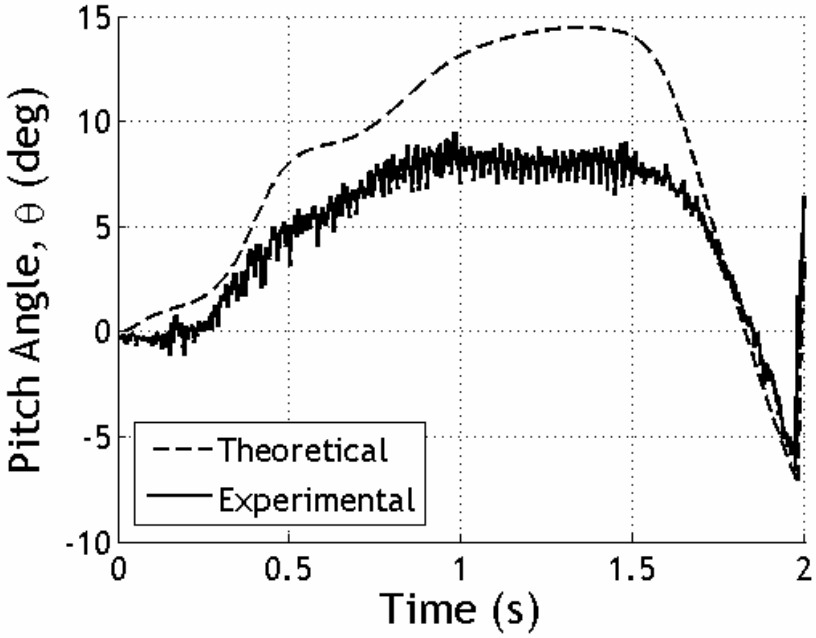

Figure 5.14: Flight test pitch angle versus time

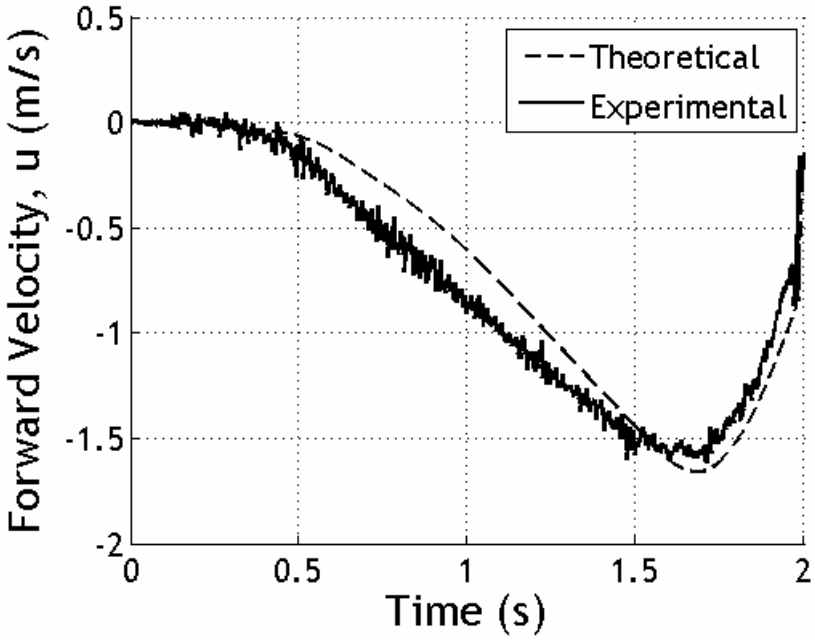

Figure 5.15: Flight test forward velocity versus time

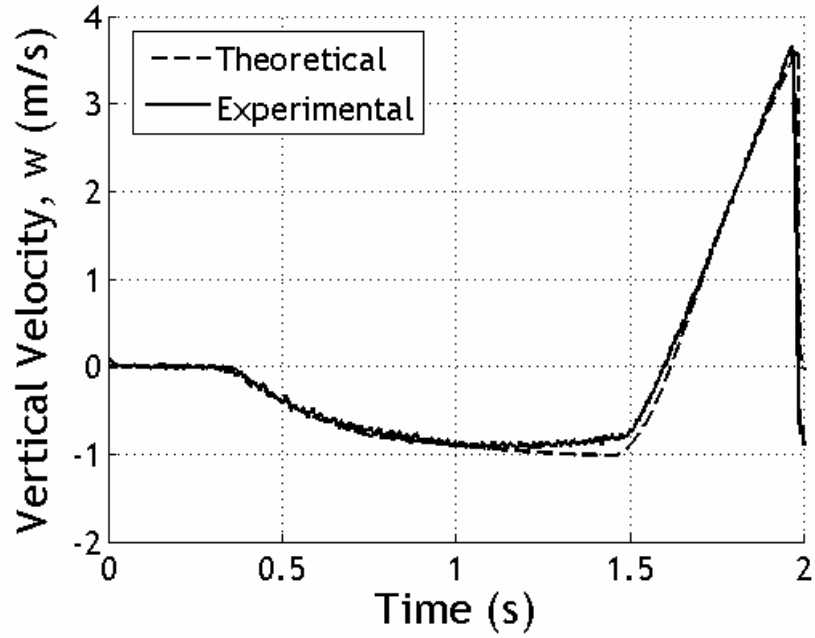

Figure 5.16: Flight test vertical velocity versus time

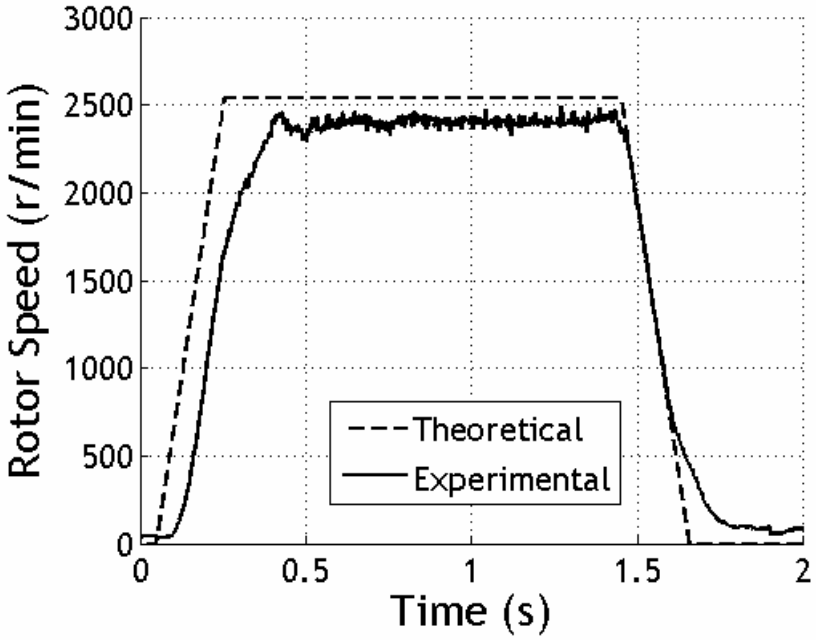

Figure 5.17: Flight test rotor speed versus time

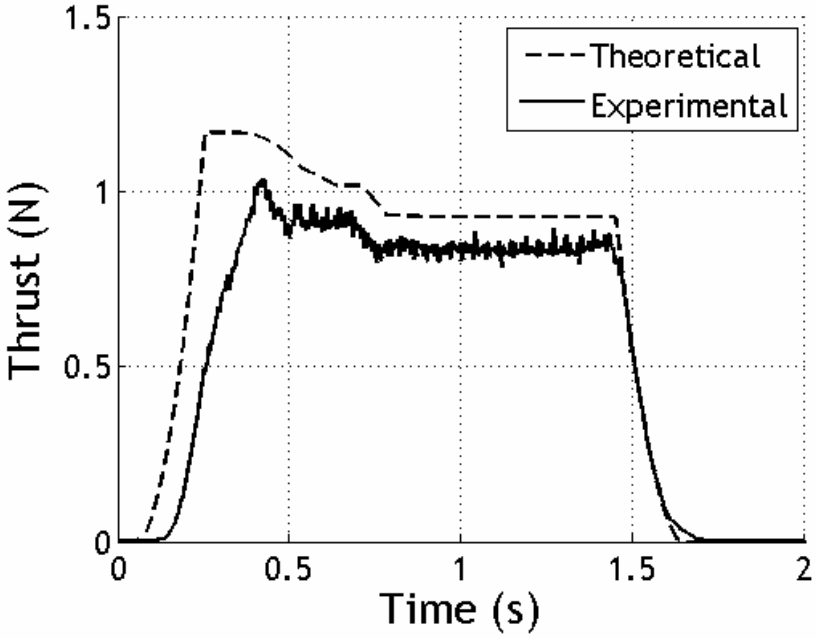

Figure 5.18: Flight test thrust versus time

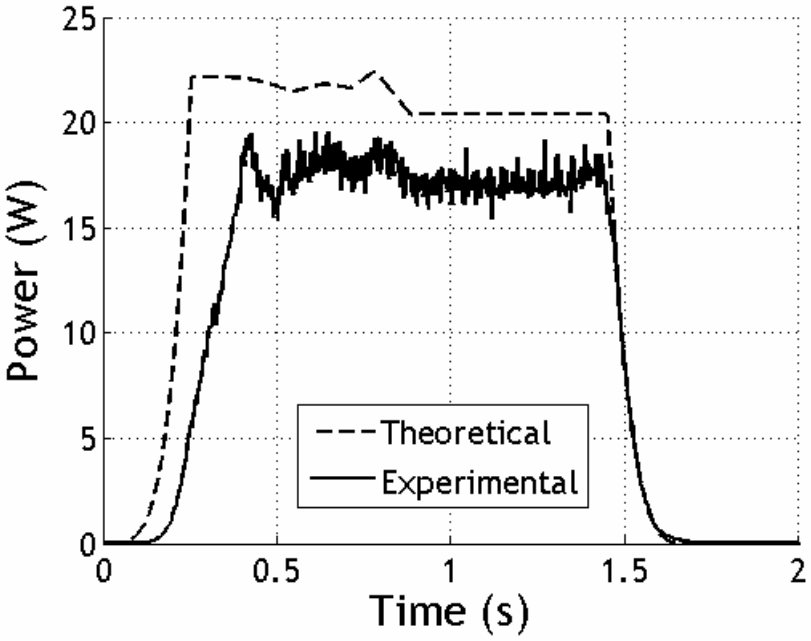

Figure 5.19: Flight test power versus time

CHAPTER 6

FLIGHT PERFORMANCE OF THE HOPPING ROTOCHUTE

As demonstrated by the captured motion presented in Chapter 3.2, the number of hops, maximum altitude, and total achievable range is greatly driven by the hop profile and mass properties of the Hopping Rotochute. To better understand how this as well as other key parameters affects the flight performance, simulation based trade studies using the validated dynamic model are performed and the results are presented in this chapter and in [102]. Example trajectories are also presented to show the dynamic behavior of the device. In addition, the results of wind sensitivity trade studies are documented as well as trajectory shaping results.

6.1 Example Trajectories

In order to determine the main flight performance drivers, many simulations were performed and the resulting trajectories were compared and analyzed. The results of two such example trajectories are given in Figures 6.1 through 6.10. The first trajectory, denoted with a solid line, was obtained using a system with a 300 mAh battery with an internal mass of 6 g at an offset of 4 cm along $\vec{I}_B$ from point P (system 1). The rotor system was powered for 1 s (pulse width = 1 s) to a speed of 4000 r/min. The second trajectory, denoted with a dashed line, is associated with a Hopping Rotochute equipped with a 250 mAh battery and an internal mass of 10 g fixed at a radial location of 6 cm along $\vec{I}_B$ from point P. Here the rotor system was powered for 6 s (pulse width = 6 s) to

a rotor speed of 3000 r/min. The properties of these two systems are outlined in Table 6.1.

Table 6.1: Properties of system 1 and 2

Parameter	System 1 Value	System 2 Value	Units
m	90.4	88.3	g
$SL_{O\rightarrow CG}$	2.65	6.80	cm
$BL_{O\rightarrow CG}$	0.0	0.0	cm
$WL_{O\rightarrow CG}$	-4.85	-5.03	cm
I_{XX}	3447	3368	g·cm^2
I_{YY}	3714	3867	g·cm^2
I_{ZZ}	854	1075	g·cm^2
I_{XY}	0	0	g·cm^2
I_{XZ}	-32	-92	g·cm^2
I_{YZ}	0	0	g·cm^2
m_{IM}	6	10	g
d_{IM}	4	6	cm
ψ_{IM}	0	0	deg
battery	300	250	mAh
pulse width	1	6	s
rotor speed	4000	3000	r/min

As shown in Figures 6.1 through 6.3, the time histories of the mass center position are vastly different. Since system 1 was powered for only 1 s and is heavier, due to the large battery size, the vehicle only reached an altitude of 3.2 m while achieving a range of 0.9 m. On the other hand, system 2 is lighter and powered for a longer duration which allows the vehicle to reach an altitude of 17.4 m with a range of 11.9 m. The effects of the rotor lag time constant are also evident for system 2 causing the range time history to nearly level off at 5.5 s before more range is gained. The pitch angle associated with

each trajectory is shown in Figure 6.4. Notice that enough time is allowed for both systems to settle to an initial launch pitch angle with values of -0.8 and -2.4 deg for system 1 and 2, respectively, before the rotor system was activated. System 2 achieves a greater initial launch angle due to the incorporation of a heavier internal mass which is located at a greater radial distance (offset). Once airborne, system 1 reaches a pitch angle of -7.6 deg before the power is ceased and the moment due to the drag pitches the vehicle in the opposite direction before ground impact. The pitch angle time history associated with system 2 is more complex, pitching back and forth due to the rotor disc lag. The forward velocity time histories are shown in Figure 6.5. System 1 reaches a maximum forward velocity of 0.58 m/s whereas the forward velocity associated with system 2 involves damped oscillations between 0 and 2.49 m/s as the system gains altitude. Once power is shut off, the forward velocity of system 2 reaches a value of 2.86 m/s before contacting the ground. The vertical velocity of system 1, shown in Figure 6.6, reaches a value of -5.35 m/s when powered and hits the ground with a speed of 5.9 m/s. System 2 reaches a vertical velocity of -3.6 m/s which remains relatively constant during powered flight and contacts the ground with a vertical speed of 6.2 m/s. The rotor speed profile of both systems is shown in Figure 6.7. As noted earlier, system 1 is powered for 1 s with a maximum rotor speed of 4000 r/min, whereas system 2 is powered for 6 s with a maximum rotor speed of 3000 r/min. The thrust produced and power consumed is shown in Figures 6.8 and 6.9 respectively. System 1 achieves a maximum thrust of 2.6 N at 2.33 s with an associated power of 111 W, whereas system 2 obtains maximum thrust and power at 2.25 s with values of 1.61 and 39 W, respectively. The initial peak of the thrust is due to in-ground-effect combined with the high rotational speeds. By integrating the

current versus time curve, shown in Figure 6.10, the amount of energy drained from the battery during a single hop can be calculated. By dividing the battery capacity by the energy drained during a single hop, the total number of hops can be estimated. With a 300 mAh battery, system 1 is able to achieve 228 hops. With a range of 0.9 m for a single hop, system 1 is able to travel 205 m in the horizontal plane on a single battery charge. The number of hops and total range of the second system with a 250 mAh battery is 33 and 391 m respectively.

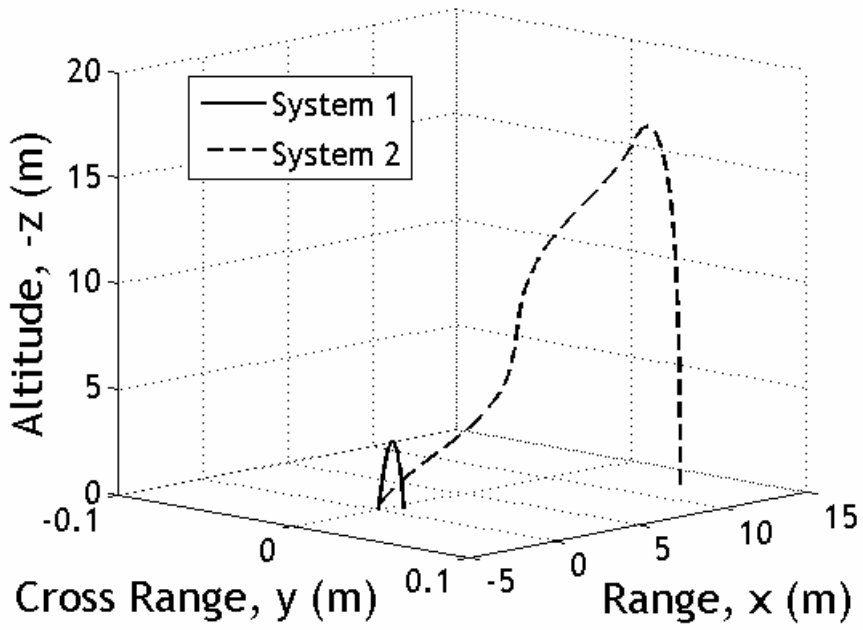

Figure 6.1: Altitude versus cross range versus range

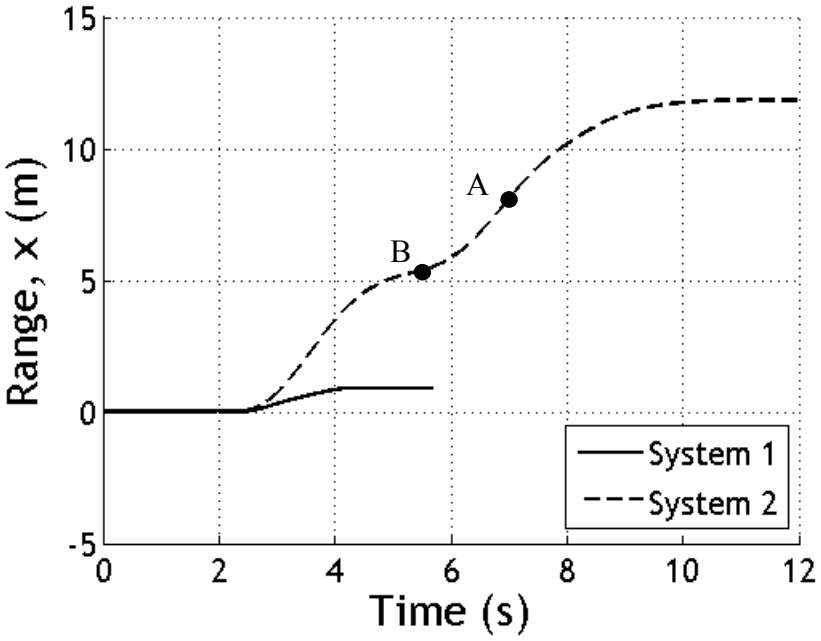

Figure 6.2: Range versus time

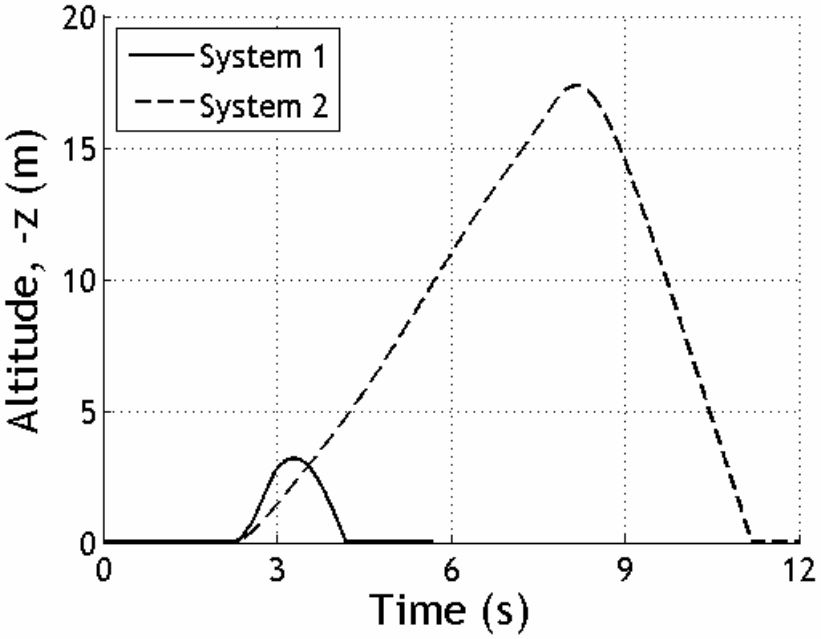

Figure 6.3: Altitude versus time

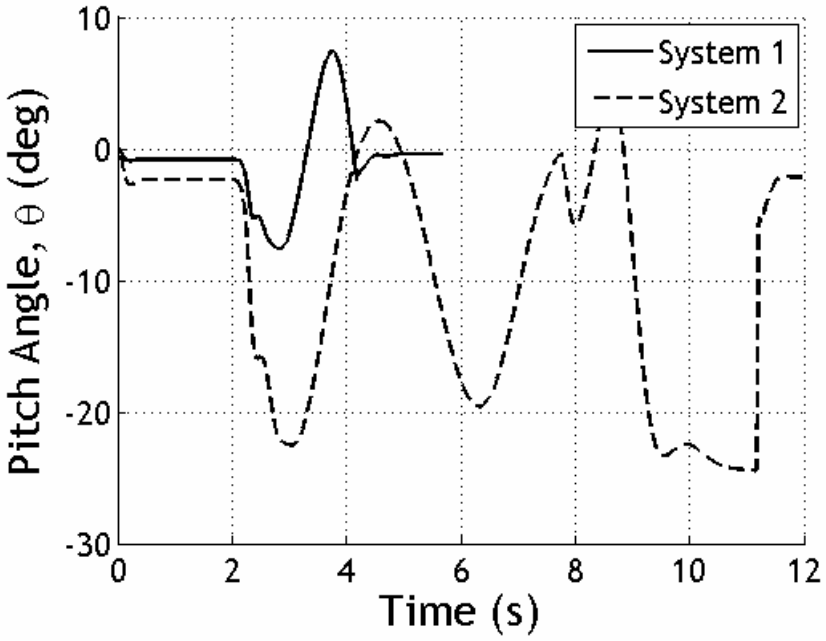

Figure 6.4: Pitch angle versus time

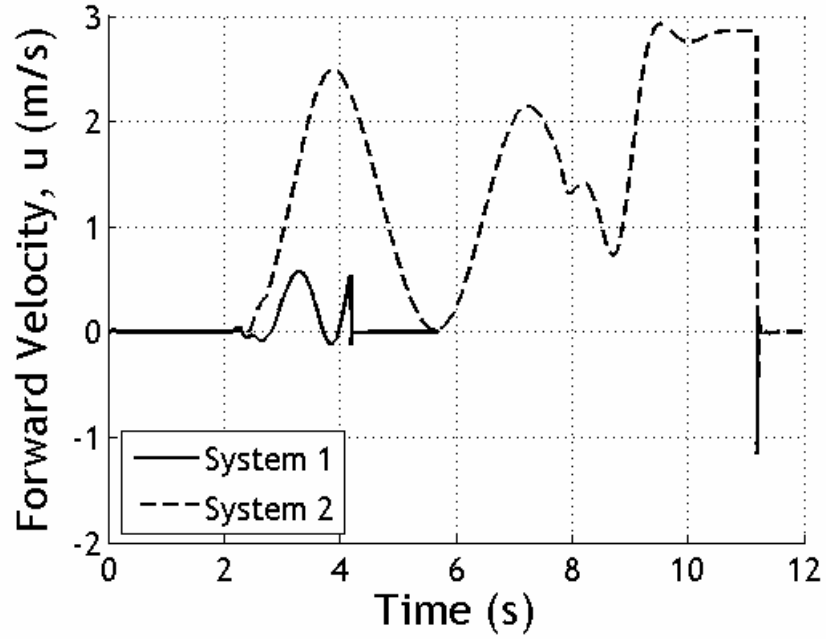

Figure 6.5: Forward velocity versus time

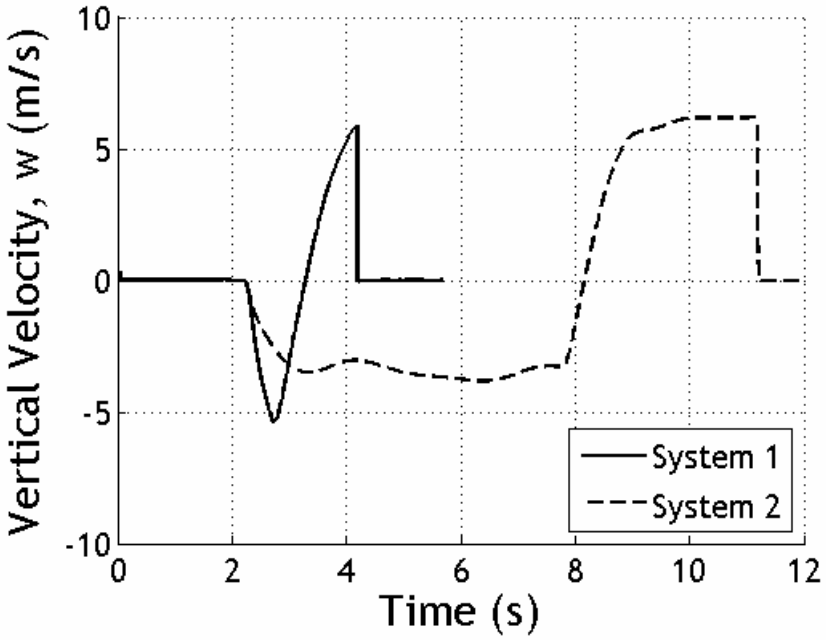

Figure 6.6: Vertical velocity versus time

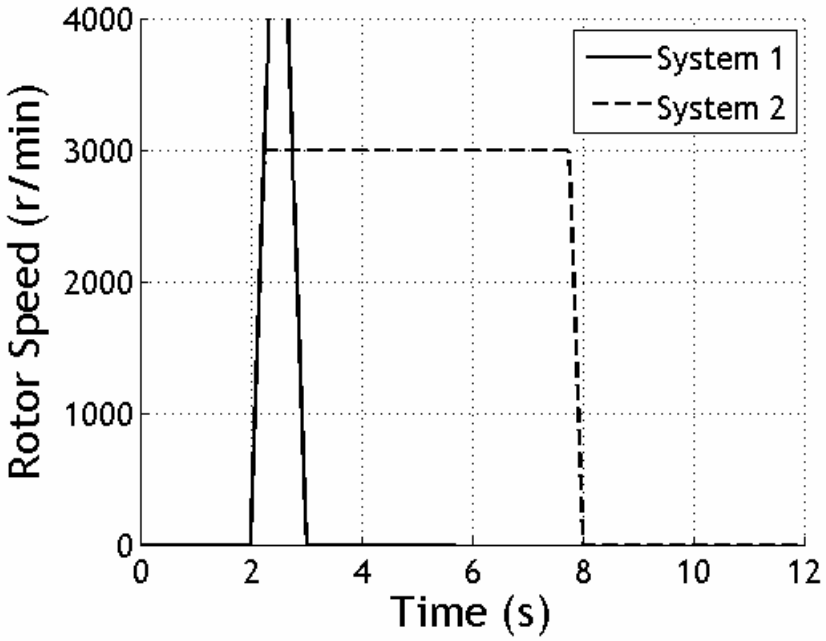

Figure 6.7: Rotor speed versus time

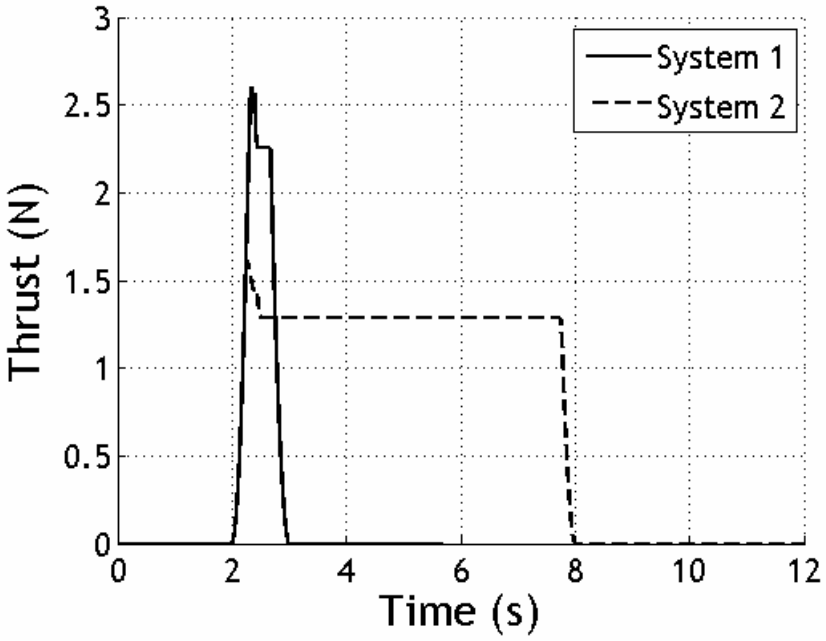

Figure 6.8: Thrust versus time

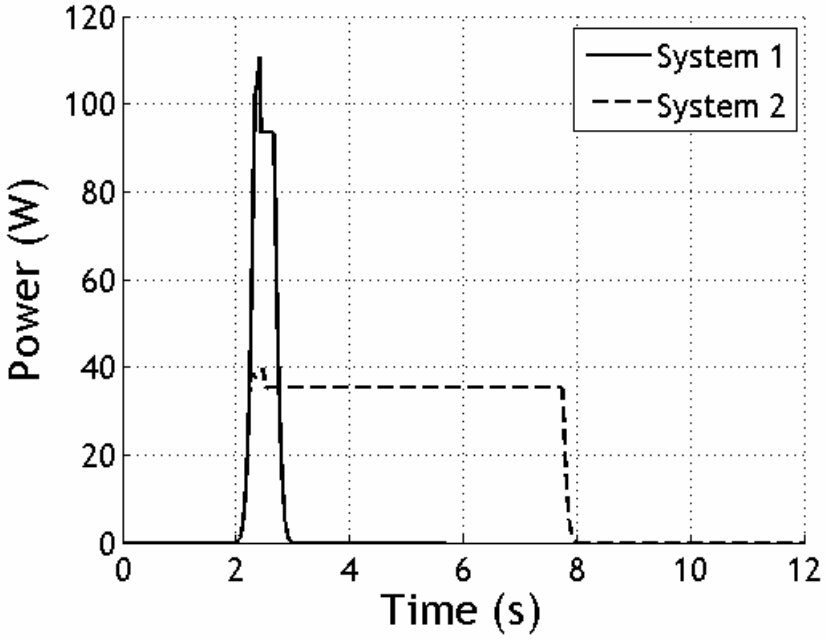

Figure 6.9: Power versus time

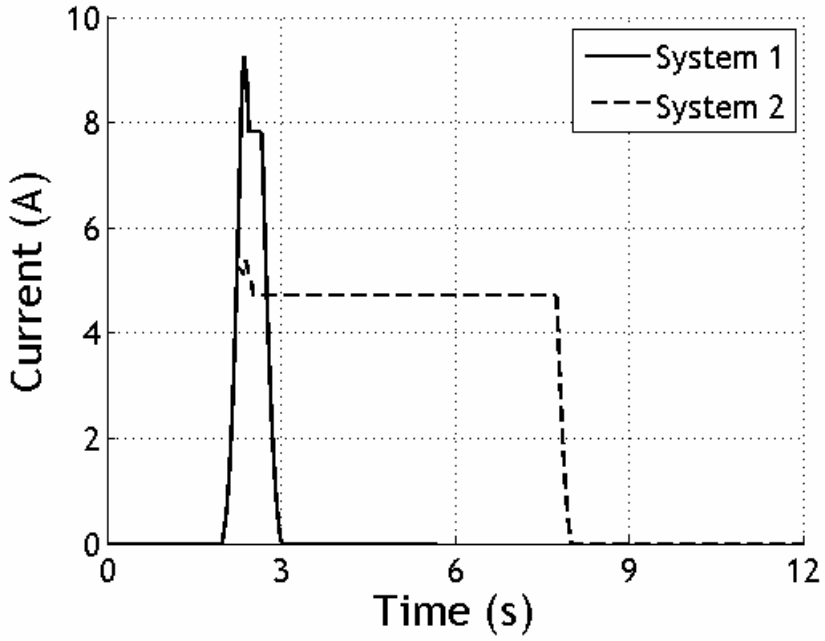

Figure 6.10: Current versus time

6.2 Flight Performance Trade Studies

As demonstrated by the two example trajectories, the dynamics and flight performance of the Hopping Rotochute are highly dependent on the mass properties, battery size, rotor speed profile, as well as the internal mass location and weight. To better understand how these key parameters influence the flight performance, trade studies were conducted that varied these parameters and the results are summarized below. For all the trade studies, the vehicle was allowed to come to rest on the ground at its equilibrium orientation before the rotor system was activated. The rotor system was then powered for a specified amount of time (pulse width) at a given rotor speed similar to the profile of the example trajectories. The slope of the upward and downward part of

the rotor speed curve, shown in Figure 6.11, is 12,000 r/min/s and -12,000 r/min/s as is characteristic for this system.

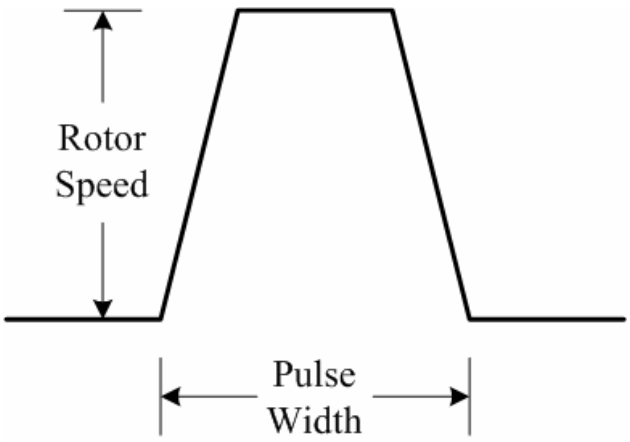

Figure 6.11: Rotor speed profile

For the first trade studies, time simulations were performed with different sized batteries while varying the internal mass (IM) weight and radial location (offset) as well as the rotor speed. The rotor system was powered for 1 s (pulse width = 1 s) with maximum speeds which varied from 2000 to 4000 r/min in 100 r/min increments. The internal mass was varied radially for point P along $\vec{I}_B$ in 1 cm increments for 0 to 6 cm with an IM mass which varied from 0 to 10 g in 2 g increments. The total mass of the system using a 250 mAh battery and the internal mass weights previously described varied from 78.3 to 88.3 g. The total mass center location along $\vec{I}_B$ varied from 0 to 0.68 cm depending on the internal mass weight and location. The resulting curves from this trade study associated with the 250 mAh battery system are given in Figures 6.12 through 6.16. Figure 6.12 presents the range achieved by a single hop as a function of internal

mass offset and rotor speed. As shown, the single hop range is increased as the internal mass weight and offset is increased. The increased IM mass (m_{IM}) and radial offset distance (d_{IM}) allows the body to settle at a higher initial launch pitch angle, shown in Figure 6.13, and also creates a larger pitching moment once airborne due to the increased moment arm between the thrust vector and center of mass of the system. Combined, these two parameters allow a slightly heavier Hopping Rotochute to achieve more range during a single hop. Figure 6.12 also demonstrates that the single hop range increases with rotor speed. The increased rotor speed creates more thrust, allowing the vehicle to reach greater altitudes while remaining airborne for an extended period of time. The maximum altitude as a function of internal mass offset and rotor speed is shown in Figure 6.14. As presented, the maximum altitude varies greatly with rotor speed while the internal mass offset has little effect. The Hopping Rotochute achieves a maximum altitude of 3.78, 3.68, 3.56, 3.44, 3.30, and 3.16 m with a rotor speed of 4000 r/min associated with the 0, 2, 4, 6, 8, and 10 g internal mass with no offset respectively. Figure 6.15 shows the total number of hops that can be achieved using a 250 mAh battery system as a function of rotor speed. As expected, more energy is consumed during flights with higher rotor speeds which reduce the number of hops. The total range that can be achieved by the Hopping Rotochute with a 250 mAh battery is again calculated by multiplying the number of hops by the range of a single hop. The total range as a function of internal mass offset and rotor speed is shown in Figure 6.16. The total range increases as the IM weight and offset are increased. The total range also increases with rotor speed up to a maximum before slightly decreasing as the rotor speed is further increased. At these high rotor speeds, the range of a single hop increases, but more

power is consumed which results in a decrease in the number of total hops and a smaller total range. The maximum total range of this system with an IM mass of 2, 4, 6, 8, and 10 g at a 6 cm IM offset occurs at rotor speeds of 3500, 3600, 3700, and 3800 r/min with total range values of 108, 203, 288, 369, and 435 m respectively.

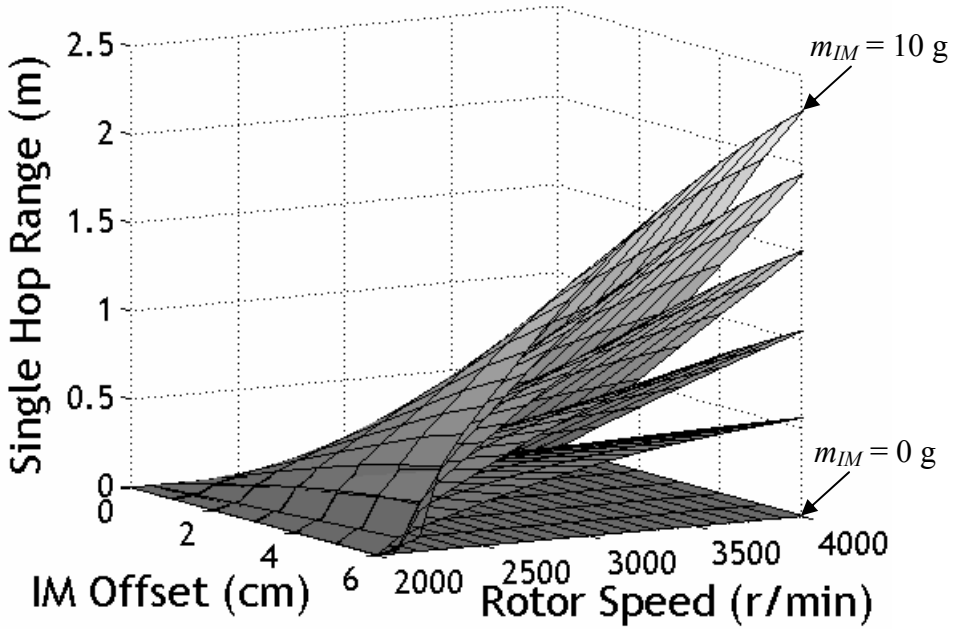

Figure 6.12: Single hop range versus internal mass (IM) offset versus rotor speed using 250 mAh battery

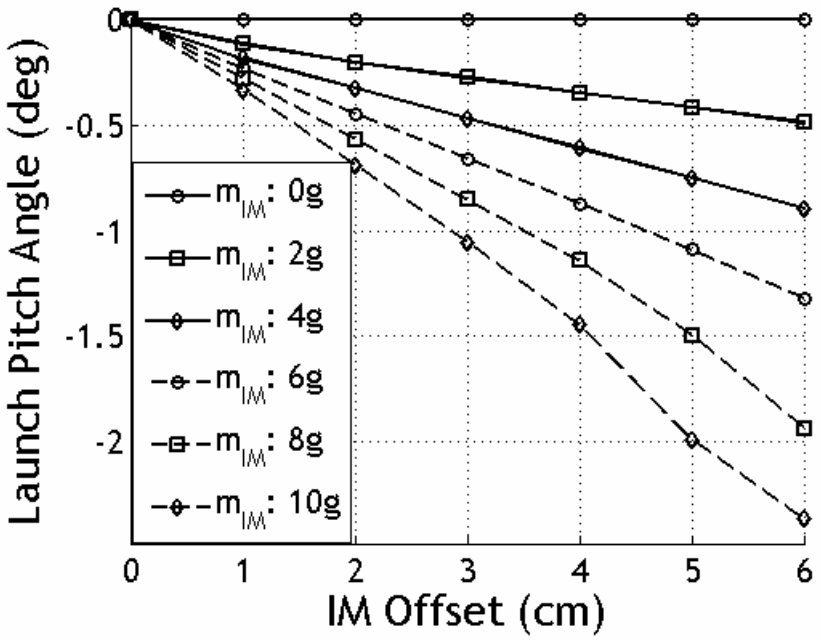

Figure 6.13: Launch pitch angle versus internal mass (IM) offset using 250 mAh battery

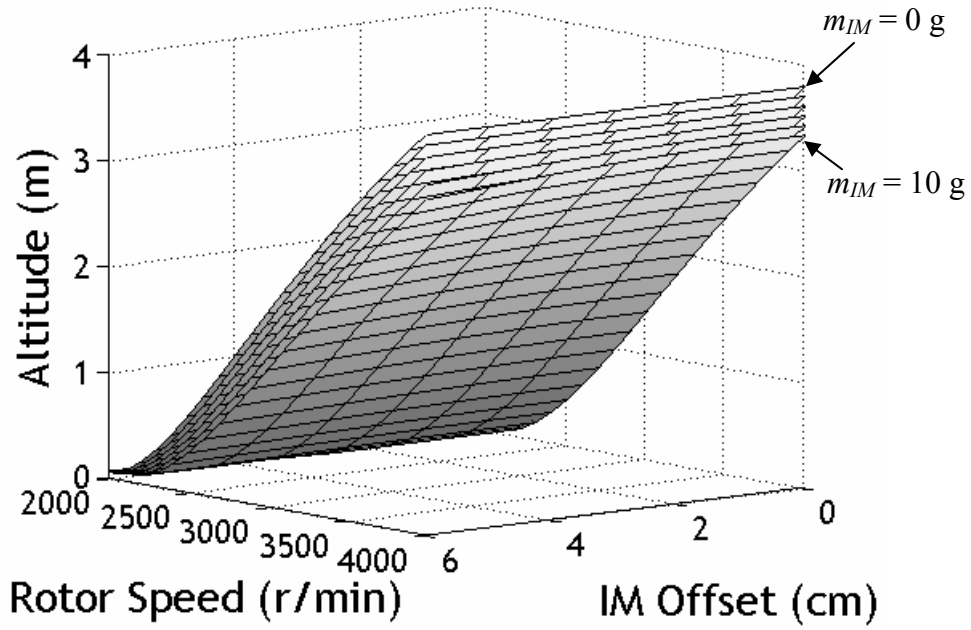

Figure 6.14: Maximum altitude versus internal mass (IM) offset versus rotor speed using 250 mAh battery

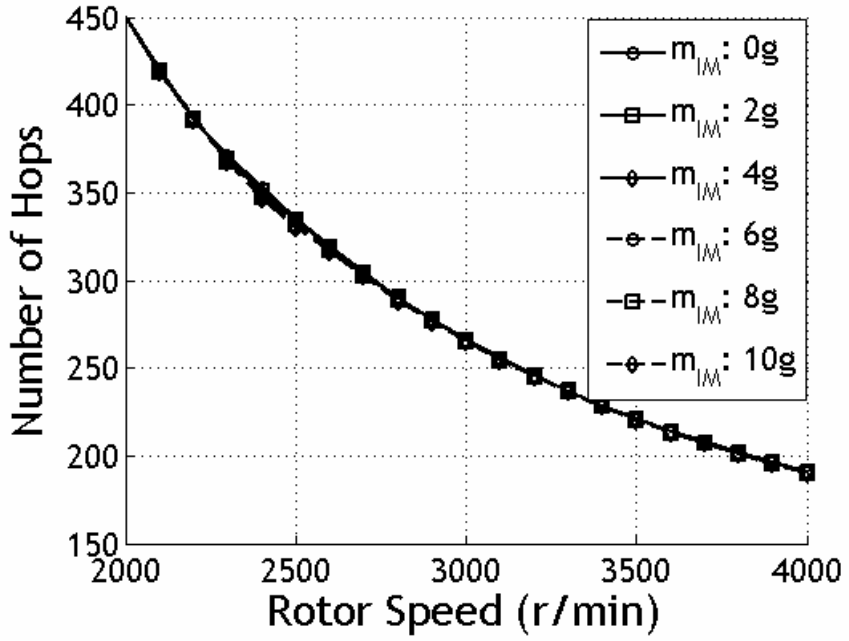

Figure 6.15: Number of hops versus rotor speed using 250 mAh battery

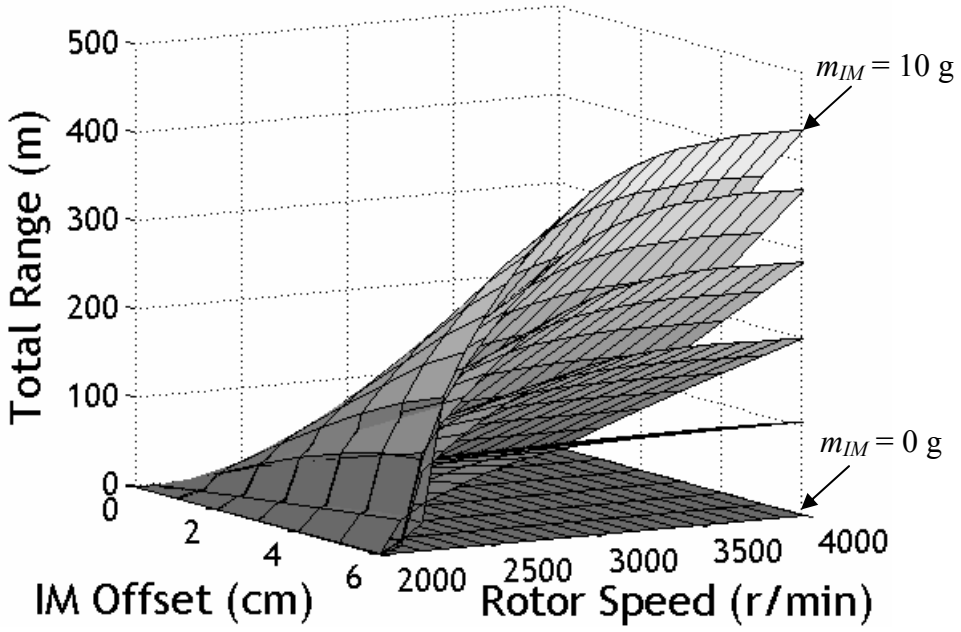

Figure 6.16: Total range versus internal mass (IM) offset versus rotor speed using 250 mAh battery

Similar flight performance trends occur when the Hopping Rotochute is equipped with a battery of greater capacity. As shown in Figure 6.17, batteries with a greater capacity allow the vehicle to achieve more hops when powered for 1 s. The increased number of hops allows the system with a greater capacity to achieve a greater total range. Figure 6.18 shows the total achievable range using a 300 mAh battery as a function of internal mass offset and rotor speed. As with the 250 mAh battery, the total range increases with as the IM weight, IM offset, and rotor speed is increased. Using a 300 mAh battery, a total range of 112, 213, 305, 393, and 468 m can be achieved with a 2, 4, 6, 8, and 10 g internal mass at an offset of 6 cm and a rotor speed of 4000 r/min respectively. These values are about 7% higher than those achieved by the 250 mAh battery system even though the battery capacity increased by 20%. The reason for this is the fact that the 300 mAh battery weighs 44% more than the 250 mAh battery, creating a heavier system which achieves less altitude. The maximum altitudes, shown in Figure 6.19, increase with higher rotor speed and less internal mass, but are smaller than that achieved by the 250 mAh battery system.

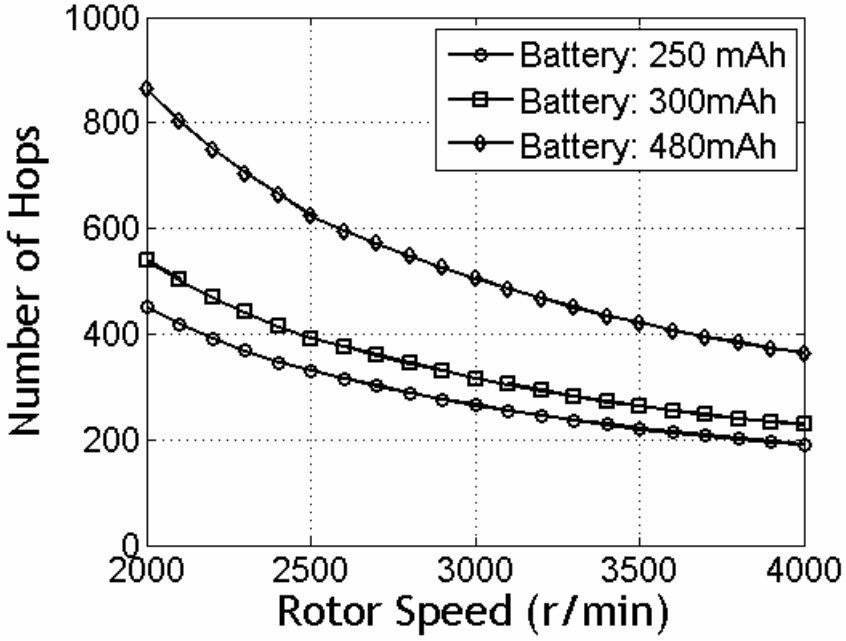

Figure 6.17: Number of hops versus rotor speed using 250, 300, 480 mAh battery

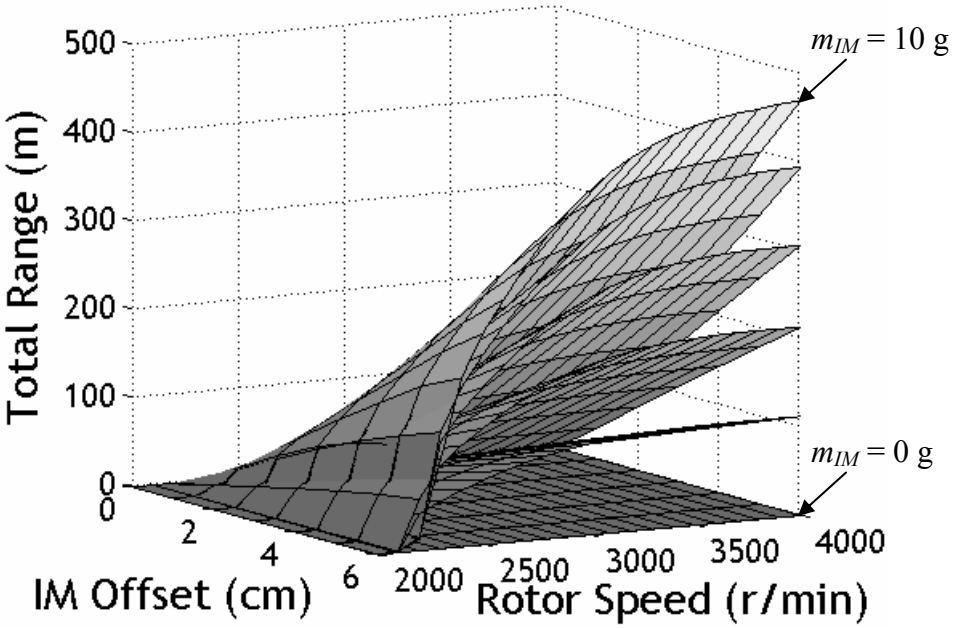

Figure 6.18: Total range versus internal mass (IM) offset versus rotor speed using 300 mAh battery

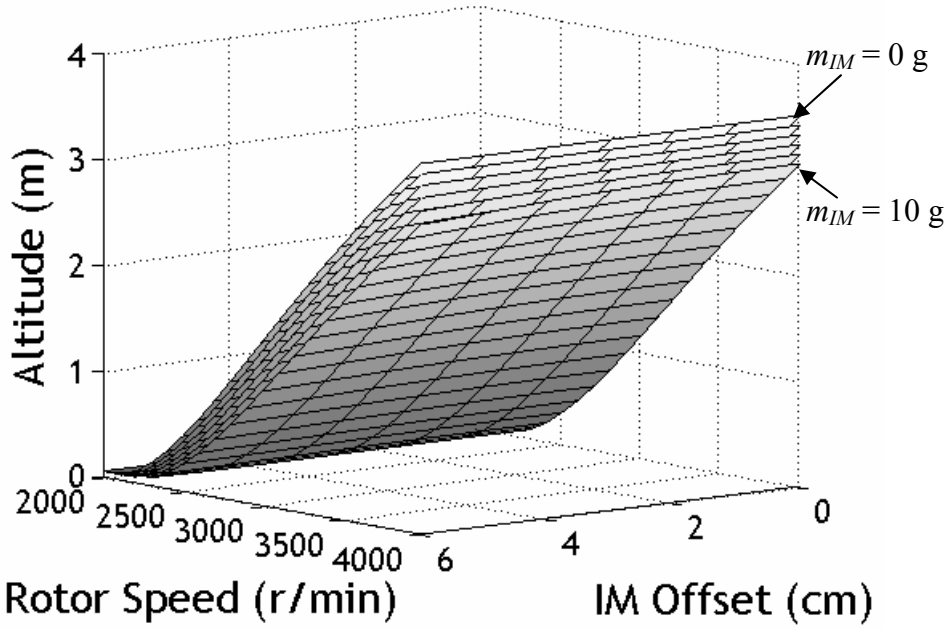

Figure 6.19: Maximum altitude versus internal mass (IM) offset versus rotor speed using 300 mAh battery

The 480 mAh battery has a greater capacity per weight than the 250 and 300 mAh batteries, which allows the vehicle to attain a greater total range. The total range as a function of internal mass offset and rotor speed is given in Figure 6.20. A Hopping Rotochute equipped with a battery of this size is able to achieve a total range of 161, 310, 444, 571, and 683 m with a rotor speed of 4000 r/min and an internal mass offset of 6 cm with IM masses of 2, 4, 6, 8, and 10 g respectively. As expected the increased weight of the battery allows the vehicle to attain less altitude before the power is ceased as presented in Figure 6.21.

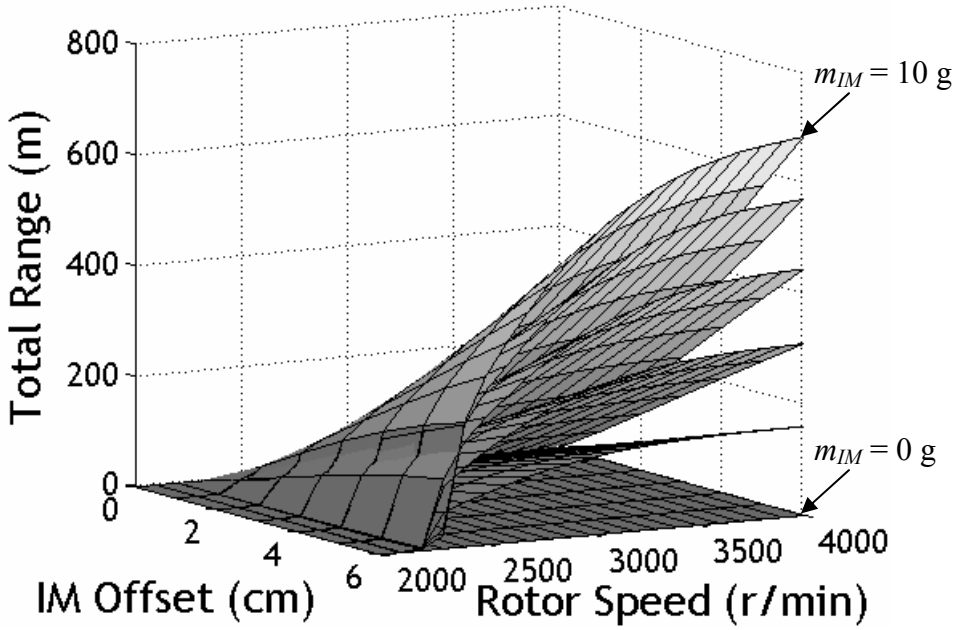

Figure 6.20: Total range versus internal mass (IM) offset versus rotor speed using 480 mAh battery

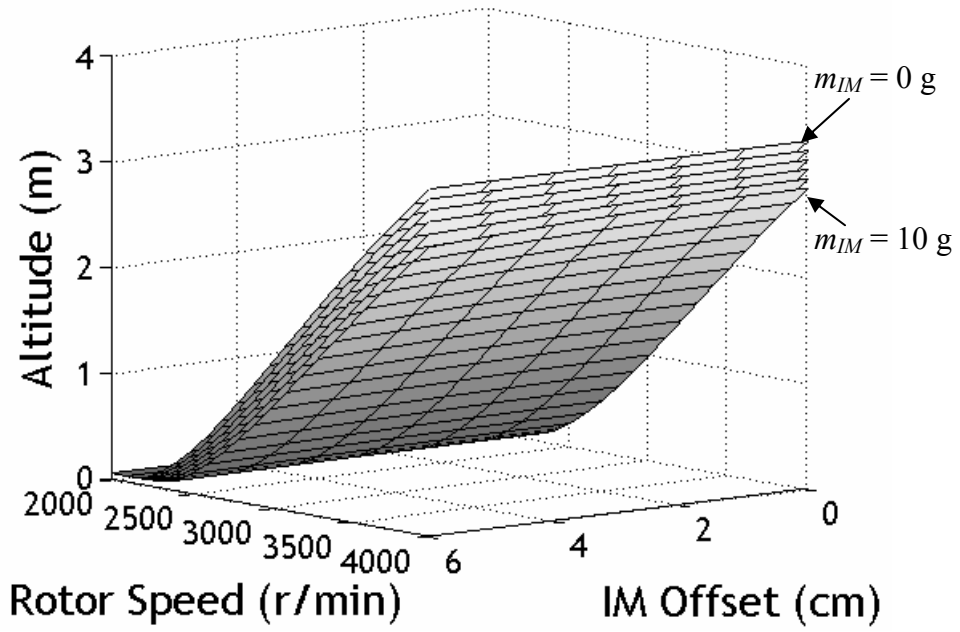

Figure 6.21: Maximum altitude versus internal mass (IM) offset versus rotor speed using 480 mAh battery

As with all micro air vehicles, the total mass of the Hopping Rotochute influences the flight performance of the vehicle. To better understand the effects of this parameter, the Hopping Rotochute mass and internal mass weight were reduced proportionally for a given internal mass offset so the mass center remained the same as the total weight decreased. The total mass of the vehicle used in this trade study are 60, 70, 80, 90, and 100 % of those from the 250 mAh battery system with an internal mass of 6 g. This amounts to system masses of 50.6, 59, 67.4, 75.9, and 84.3 g respectively. The internal mass offset was again set to 0 through 6 cm in 1 cm increments from point *P* which amounts to system mass center locations along $\bar{I}_B$ of 0, 0.07, 0.14, 0.21, 0.28, 0.36, and 0.43 cm. The results of this trade study are presented in Figures 6.22 and 6.23. Figure 6.22 plots the total range as a function of internal mass offset and rotor speed. As shown, the maximum total range for the 60, 70, 80, 90, and 100 % mass vehicles occurs with a 6 cm IM offset at a rotor speed of 2300, 2600, 3000, 3400, and 3600 r/min respectively. The total range achieved at these rotor speeds are 378, 348, 323, 303, and 288 m. Hence, decreasing the total mass by 10, 20, 30, and 40 % increase the total range by 5, 12, 21, and 31% respectively. Once again, these optimum values occur due to the fact that the range of a single hop increases and the number of hops decreases as the rotor speed is increased. The optimum occurs when the product of these two values are maximized. The maximum achieved altitude as a function of internal mass offset and rotor speed is shown in Figure 6.23. Greater altitudes are achieved with lighter systems with smaller internal mass offsets and larger rotor speeds as shown in Figure 6.23. As demonstrated, decreasing the total weight of the Hopping Rotochute allows better flight performance by increasing the total range and maximum altitude.

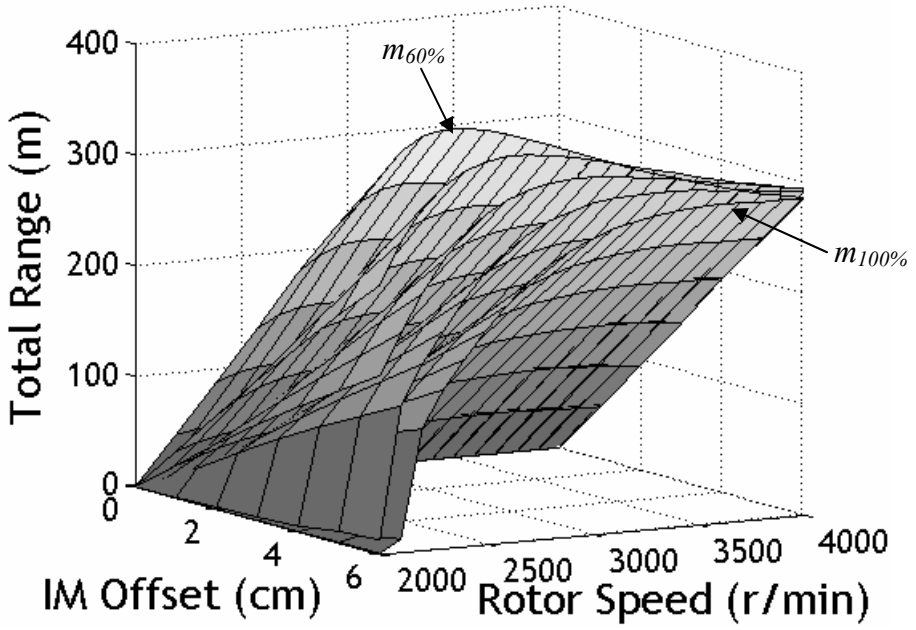

Figure 6.22: Total range versus internal mass (IM) offset versus rotor speed using 250 mAh battery

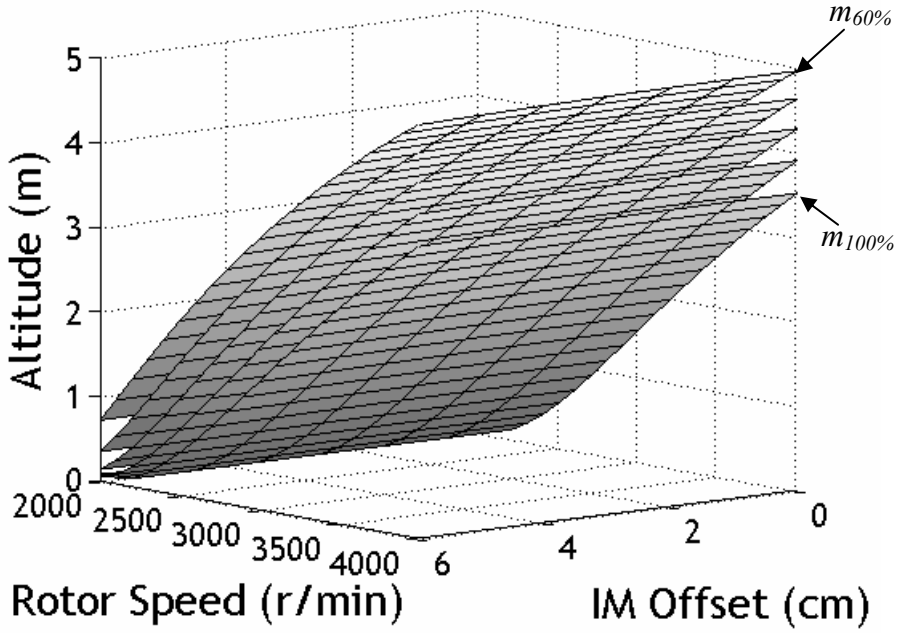

Figure 6.23: Maximum altitude versus internal mass (IM) offset versus rotor speed using 250 mAh battery

The trade studies presented above are based on powering the rotor system for 1 s at various rotor speeds. As the second example trajectory demonstrated, greater range and altitude can be achieved if the rotor system is activated for a longer period of time (pulse width). To show the effects of this parameter, another trade study was performed which varied the pulse width and rotor speed for a 250 mAh battery system with IM masses of 2, 4, 6, 8, and 10 g located at an offset of 6 cm along $\bar{I}_B$ from point *P*. The results of this trade study are shown in Figures 6.24 through 6.26. As shown in Figure 6.24, the number of hops exponentially decreases as the pulse width increases. The number of hops as well as the dynamics of the different weighted systems affects the total range as shown in Figure 6.25. Notice that the total range peaks at a pulse width of 2 s and a rotor speed of 2600 r/min. Increasing the rotor speed and pulse width from this peak tends to decrease the total range although smaller amplitude peaks occur when the pulse width is 5 and 8 s. The peaks and troughs that occur as the pulse width is varied are caused by the dynamics of the system. As shown by the second example trajectory, the rotor lag causes the slope of the range versus time curve to vary (see Figure 6.2). The peaks in the total range curve of Figure 6.25 occur when the power is ceased while the slope is steep, as demonstrated by point A in Figure 6.2. The troughs occur when the power is shut off while the slope of the range versus time curve is small, point B in Figure 6.2. The maximum altitude as a function of pulse width and rotor speed is shown in Figure 6.26. As one would expect, the maximum altitude increases as the rotor speed and pulse width increases.

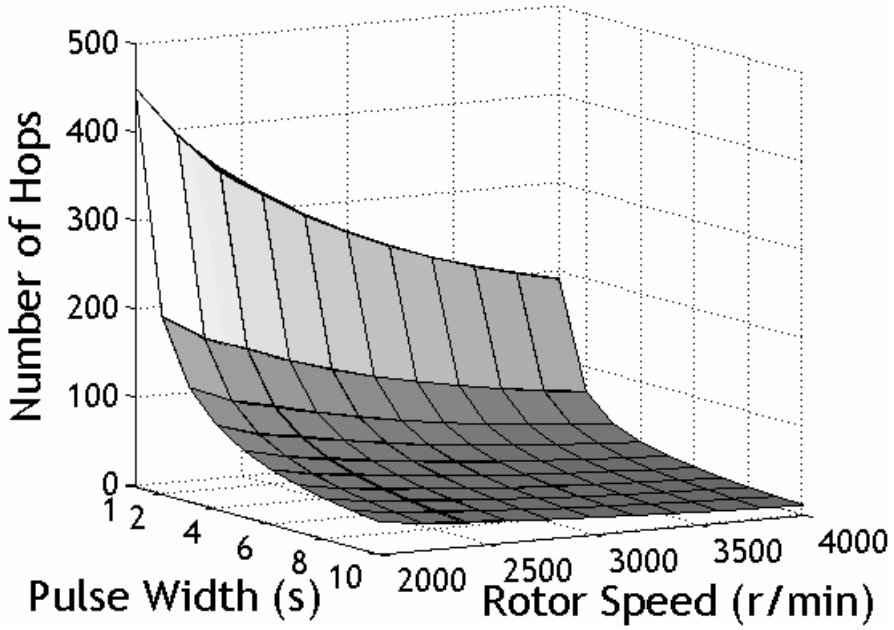

Figure 6.24: Number of hops versus pulse width versus rotor speed using 250 mAh battery

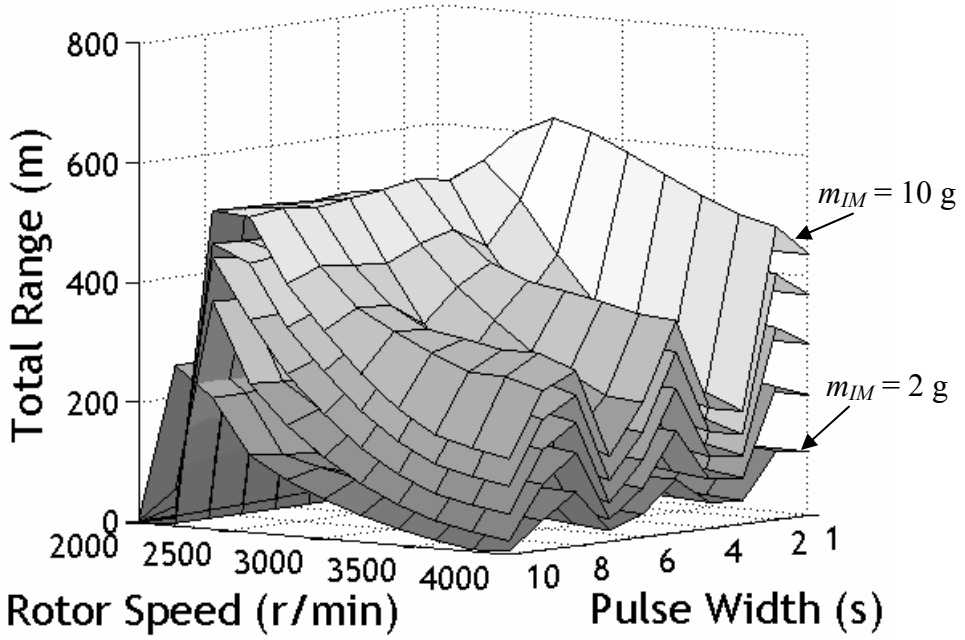

Figure 6.25: Total range versus pulse width versus rotor speed using 250 mAh battery

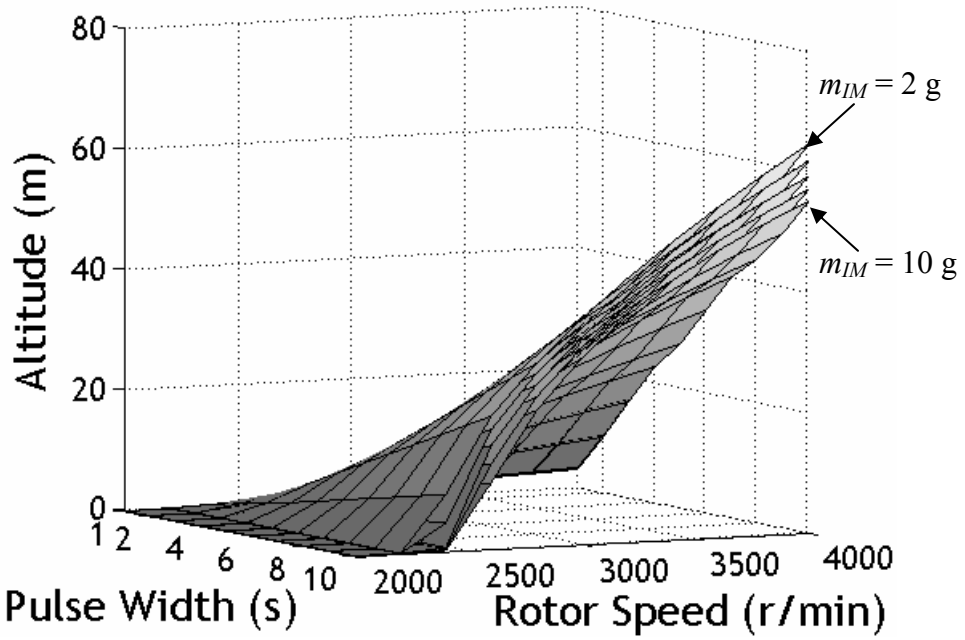

Figure 6.26: Maximum altitude versus pulse width versus rotor speed using 250 mAh battery

Figure 6.27 plots the total range as a function of altitude for the systems using the IM masses of 2, 4, 6, 8, and 10 g while powered for 2 s. As shown, the maximum total range associated with each IM mass peaks at around 2 m of altitude and decreases as the altitude increases. The reason for this is attributed to the dynamics of the system and the point at which the power is ceased as previously described. Based on these findings, a hop strategy consisting of many small hops would results in a greater total range as opposed to fewer large hops. Note that similar trends occur when the pulse width is increased, with greater altitudes being attained.

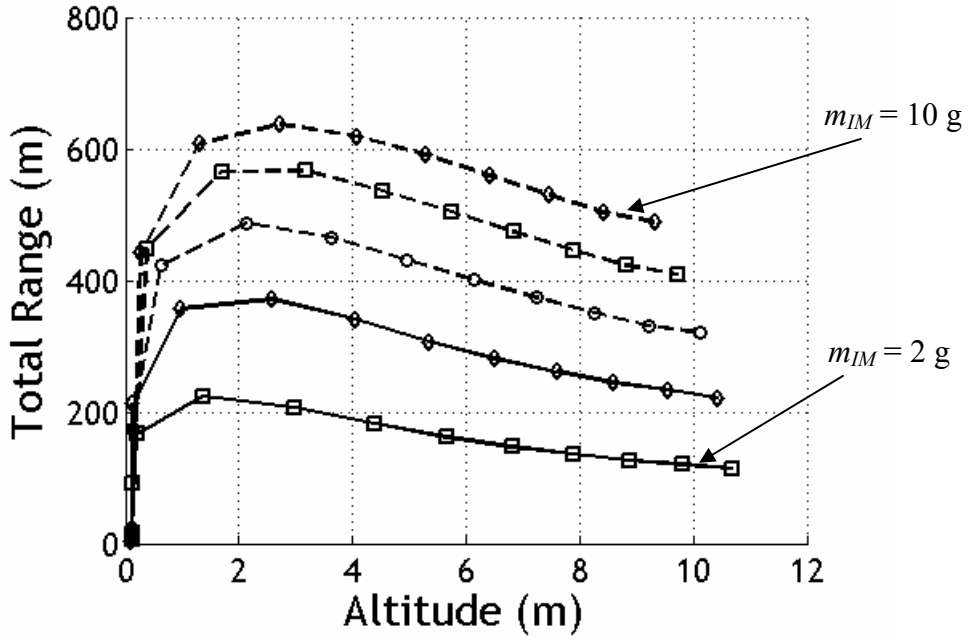

Figure 6.27: Total range versus maximum altitude with 2 s pulse width using 250 mAh battery

6.3 Atmospheric Wind Trade Studies

In order to robustly traverse complex terrain, a cage was built around the rotor system to protect the rotating components. Unfortunately, this structure and the base of the vehicle create additional drag which impedes the motion of the vehicle while airborne. In order to determine how well the Hopping Rotochute performs with horizontal atmospheric winds acting upon it, simulation based trade studies were performed to predict the wind sensitivity of the vehicle. For the first wind trade study, atmospheric winds of various speeds were applied to a Hopping Rotochute with a 250 mAh battery and an internal mass of 2, 4, 6, 8, and 10 g located 6 cm along $\vec{I}_B$ from point *P*. The rotor system was powered for 1 s up to 4000 r/min. The wind speeds (V_{MW})

were varied along the $\bar{I}_I$ axis from 1.5 m/s (head wind) to -1.5 m/s (tail wind) in increments of 0.2 m/s. Figure 6.28 shows the results of this trade study. As shown, with a greater head wind, the vehicle achieves less range and at some point actually lands behind where it initially started. The head winds with a magnitude of 0, 0.33, 0.59, 0.82, 1.02, and 1.20 m/s allow a vehicle with an internal mass of 0, 2, 4, 6, 8, and 10 g to land in the same position as it began respectively. Figure 6.28 also shows that tail winds of greater magnitude allow the vehicle to achieve more range.

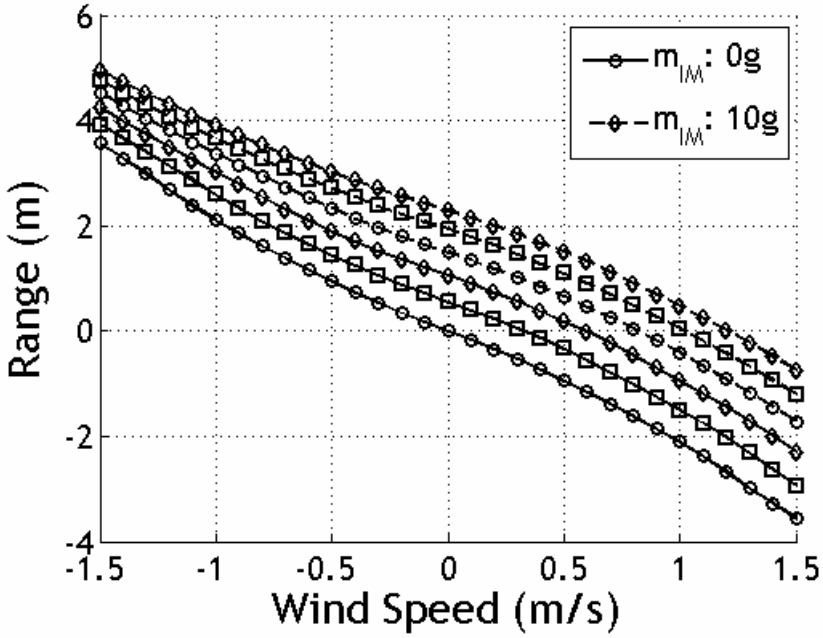

Figure 6.28: Range versus wind speed

To show the effects of varying horizontal wind directions, the Hopping Rotochute with a 250 mAh battery and a 10 g internal mass at 6 cm offset along $\bar{I}_B$ was simulated with wind speeds (V_{MW}) that varied between 0.25 and 1.5 m/s in 0.25 m/s increments at

azimuthal angles (ψ_{MW}) from 0 to 350 deg in 10 deg increments. Again, the rotor system was powered for 1 s up to a rotor speed of 4000 r/min. The results of this analysis are given in Figure 6.29, where the inner ring and outer ring are associated with wind speeds of 0.25 and 1.5 m/s respectively. As shown, the wind dispersion plot for a given wind magnitude is elliptical in nature with higher winds giving higher dispersion radii. Also note that wind speeds above 1.25 m/s allow the vehicle to land behind where it started as suggested by Figure 6.28.

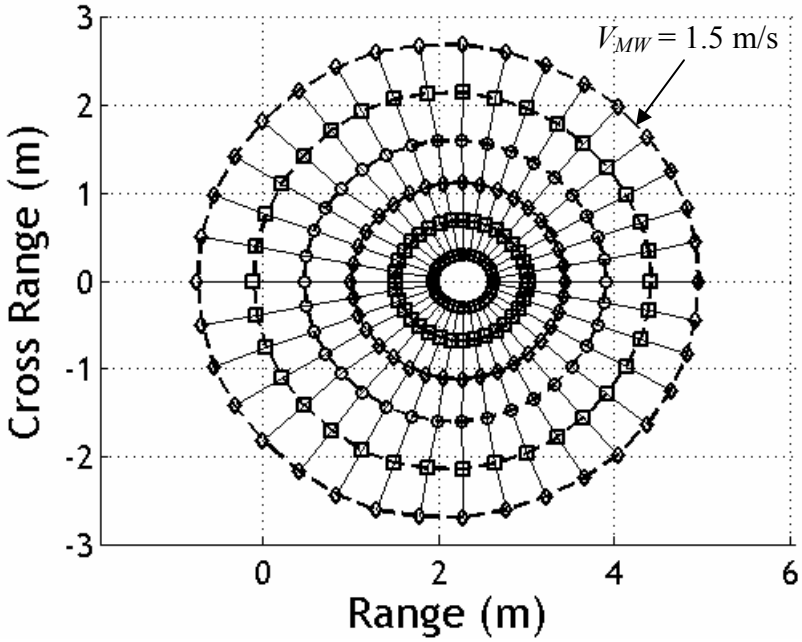

Figure 6.29: Wind dispersion

6.4 Trajectory Shaping

An additional benefit realizable by the Hopping Rotochute is the ability to shape the trajectory once the vehicle is airborne. This feature is achievable by using the rotor

speed and internal mass location as inputs to control the direction of travel. Similar work involving a mass center shifting mechanism to steer a micro air vehicle has showed that directional control is possible [36-39]. This feature could potentially allow the vehicle to fly over or around complicated objects with overhangs.

To demonstrate the trajectory shaping capabilities of the Hopping Rotochute, the dynamic model was employed to simulate the shaped motion. The resulting motions of two such shaped trajectories are shown in Figure 6.30. For both simulations, the goal was to fly around a 10 m diameter cylinder that is 5 m high using a 6 g internal mass located 6 cm from the pivot point *S*. During the first trajectory, shown with the solid line, the internal mass is allowed to rotate around the internal perimeter of the base about the $\vec{K}_B$ axis by an angle ψ_{IM} from the $\vec{I}_B$ axis. As shown in Figure 6.30, the Hopping Rotochute is able to fly around the back side of the cylinder using the rotor speed and IM azimuth angle time histories presented in Figures 6.31 and 6.32, respectively. The second trajectory, denoted by the dashed line, hops over the cylinder by employing an internal mass which can rotate about the $\vec{J}_B$ axis by an angle θ_{IM} from the $\vec{I}_B$ axis. As shown in Figure 6.30, the vehicle initially reaches an altitude of about 4 m before the internal mass is pitched forward allowing the vehicle to fly over the cylinder. The rotor speed and internal mass pitch angle time histories for this trajectory are also shown in Figures 6.31 and 6.32, respectively. Note that the type of internal mass movement during the second trajectory is not possible with the Hopping Rotochute prototype, but is included here to demonstrate the trajectory shaping capabilities and help motivate future designs.

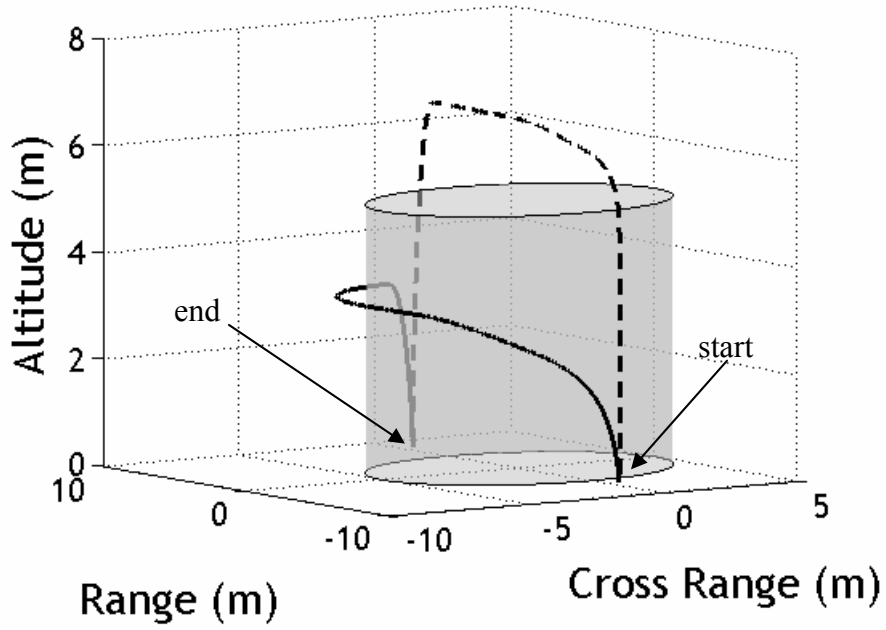

Figure 6.30: Altitude versus cross range versus range during trajectory shaping

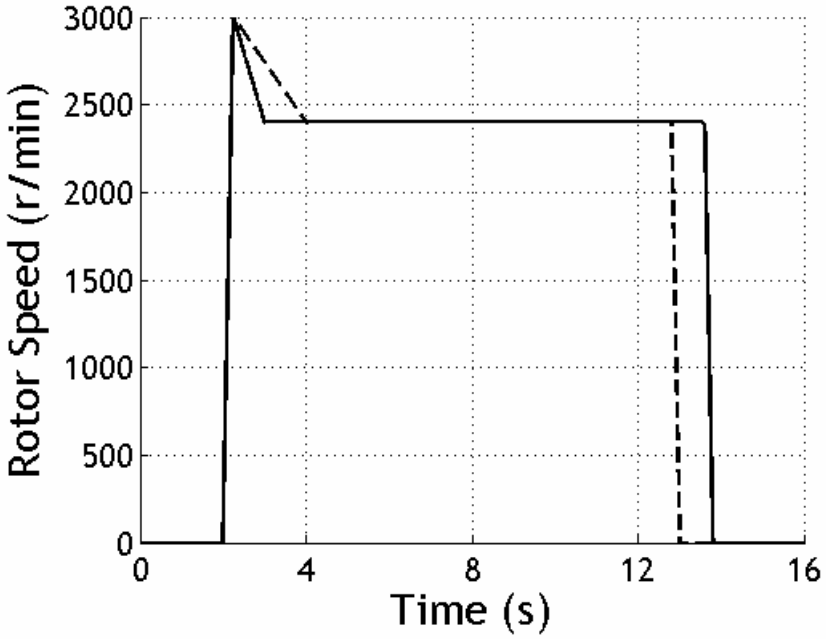

Figure 6.31: Rotor speed versus time during trajectory shaping

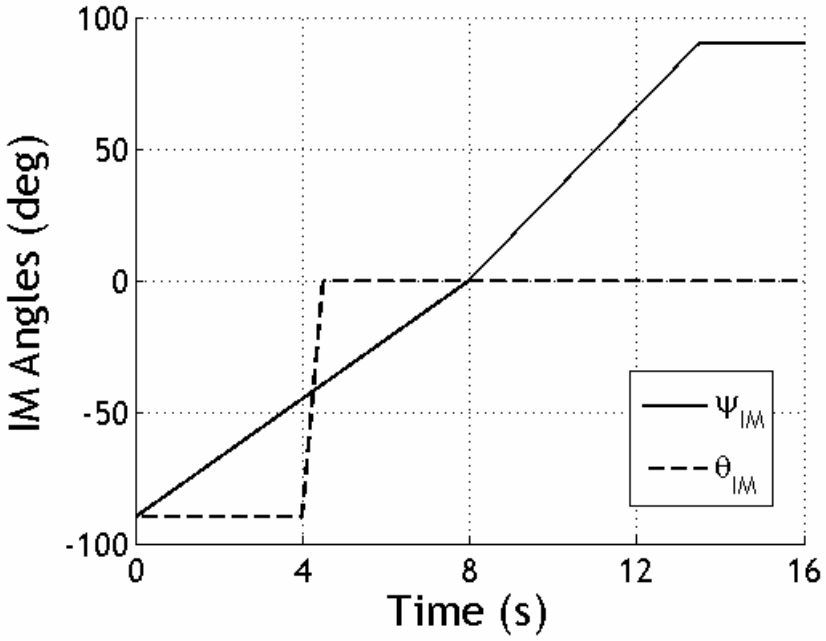

Figure 6.32: Internal mass (IM) angles versus time during trajectory shaping

CHAPTER 7

CONCLUSIONS AND FUTURE WORK

7.1 Conclusions

The design, fabrication, and testing of a unique hybrid micro vehicle was presented in this thesis as well as an analytical study of the flight performance. The development of the Hopping Rotochute focused on creating a robot that robustly traverses rugged and/or cluttered environments such as caves and damaged buildings which are difficult for conventional air and ground vehicles to navigate through while minimizing energy consumption over extended periods of time. The design of the vehicle was driven by these mission requirements and the following system requirements:

1. The vehicle must be made as small, lightweight, and simple as possible using off-the-shelf components
2. The vehicle must possess some means of directional control
3. The vehicle must be able to passively upright itself no matter which orientation it lands
4. The vehicle must be able to carry small payload (at least 10 g) without it incurring any damage as the robot travels
5. The vehicle must be able to jump at least 2 m high
6. The vehicle must be able to achieve a range of at least 200 m
7. The vehicle should posses the ability to shape a trajectory when airborne

To satisfy these requirements, several conceptual designs were proposed and a prototype was fabricated based on the idea of mounting a rotor system on a body with a low mass center and egg-like shape. The rotor system provides the necessary lift to allow

the powered vehicle to hop over obstacles while the body properties permit the device to passively upright itself once in ground contact. A movable internal mass, which can rotate around the internal perimeter of the body, was incorporated into the design to provide a means for directional control. The Hopping Rotochute prototype was tested in a number of different environments which demonstrated that all design and system requirements were satisfied.

A dynamic model of the Hopping Rotochute was also developed to predict the dynamic behavior and flight performance of the vehicle. Experimental techniques were used to determine the unknown parameters of the dynamic model. A comparison was made between the vehicle's motion measured using a 12 camera motion capture system and the simulation results to assess the validity of the experimentally-tuned dynamic model. Measured and predicted motions during ground contact and flight agree favorably with the main differences being the horizontal distance traveled during ground impact and the achieved attitude during flight. These differences are mainly attributed to imperfections incurred during the fabrication of the device, unaccounted for nonlinear spring and damper constants, and un-modeled rotor dynamics during flight.

Through the employment of the validated dynamic simulation model, example trajectories and trade studies showed that the key parameters influencing flight performance include the total system weight, rotor speed profile, internal mass weight and location, as well as battery capacity. In general, the total achievable range of the device can be increased by incorporating a larger internal mass at an increased radial offset. Minimizing the weight of the total system also increases the total range as does using a battery with a high capacity per weight ratio. The total range of the vehicle can

be optimized based on maximizing the product of the number of hops and the range of a single hop of a given system. The maximum total range is also dependent on the pulse width and the dynamics of the system. Due to the relatively large coefficient of drag associated with the body, moderate atmospheric winds can offset the range achieved during a single hop. By using the internal mass as a directional control mechanism during flight, the trajectory of the Hopping Rotochute can be shaped to maneuver the vehicle around large, intricate objects.

7.2 Recommended Future Work

Although the Hopping Rotochute prototype developed in this dissertation met all the mission and system requirements, the design of the vehicle is not optimal. The incorporation of available off-the-shelf components strongly influenced the overall size, weight, and performance of the device. The recommended work, presented below, outlines some ideas and methods that could be used to improve the design and functionality of the Hopping Rotochute.

The rotor system is a key component influencing the size and jumping capabilities of the Hopping Rotochute. To improve these characteristics, trade studies could be performed using the dynamic model with the incorporation of a combined blade element-momentum theory [42-46]. Parameters such as the blade twist, taper, pitch, radius, chord, and airfoil section as well as the number of blades could be varied to evaluate the resulting flight performance. Based on these results, a smaller rotor system capable of improved jumping capabilities may be possible.

Improvements to the drive system should also be carried out. By using a rapid prototyping machine, a custom transmission could be produced that is lighter, smaller,

and more efficient than the one currently used. In addition, the incorporation of a brushless DC electric motor would increase the efficiency of the drive system and permit greater power at a given power plant weight as compared to that of the brushed motor. The employment of two such motors may allow for a simpler drive system design while making the trimming process easier.

In order to allow for hovering capabilities, the mechanism driving the movement internal mass should be revised. Using a small DC motor in combination with a servo, such as that shown in Figure 2.1 b), would allow the device to hover and have a means for directional control. Otherwise, a mechanism consisting of two servos could be employed to "pan and tilt" the internal mass within the internal cavity of the vehicle's base. In addition, the development and implementation of a customized printed circuit board (PCB) could be used to control the internal mass while replacing the receiver and electronic speed controller. The resulting PCB would most likely be smaller and lighter than that of the off-the-shelf electronic components combined.

The main body of the Hopping Rotochute could also be improved. Designing a cap for the base, just under the rotor system, may help reduce the download inflicted on the body. In addition, creating a smaller base (core) could minimize the effects of download while decreasing the weight. At the extreme, the core could be eliminated while having the propulsion system supported by members attached to the cage. Although these design changes could drastically reduce the area under the rotor system, the surface area for the damping material (cushion) would be reduced, allowing the device to oscillate for longer when in ground contact. The electronics would also be less protected, being more vulnerable to failure during collisions.

To more accurately predict the flight dynamics and performance of the Hopping Rotochute, future work should be done to refine the dynamic model. In particular, the aerodynamic coefficients of the body should be experimentally obtained using wind tunnel tests. By mounting the Hopping Rotochute on a sting balance or load cell, these aerodynamic coefficients could be determined by measuring the force, air velocity, and air density during angle-of-attack sweeps. In addition, the rotor system aerodynamic characteristics could be more accurately determined using a similar procedure. The soft contact model could be generalized to allow rugged terrain to be modeled and the response of the vehicle on this terrain could be simulated. Using this improved dynamic model, trade studies similar to the ones presented in this thesis could be performed to further optimize the flight performance.

Other future work could involve the incorporation of a small wireless camera to transmit images to an operator. Using a video display, the user could assess the easy-of-use and controllability of the device when out of line-of-sight. The camera could be mounted on the internal mass bar and act as the internal mass. This would allow the operator to pan the camera while allowing him or her to control the direction of travel.

The most exciting future work would be the development of an autonomous Hopping Rotochute. This milestone, however, involves overcoming many issues concerning the development of a small microcontroller, the integration of sensors, and the design and implementation of control and obstacle avoidance algorithms. A recommended first step towards this achievement is to employ the VICON motion capture system in combination with the computer the motion capture system software is installed on and a radio transmitter. The motion capture system would act as a “sensor”

and used to measure the states of the vehicle as well as the position of the internal mass in real time. The computer would provide the required computational power to determine the desired path and the control inputs which would be determined from algorithms developed on an installed software package such as MATLAB. In addition, the software package is required to send the commands, in pulse width modulation (PWM) signal form, from the computer to a radio transmitter with a trainer feature. In trainer mode, the radio would transmit the PWM signals to the receiver mounted on the Hopping Rotochute. This method allows the same electrical components incorporated on the radio controlled device to be used without developing and implementing a separate autopilot. Furthermore, different control and obstacle avoidance algorithms could be easily tested to evaluate their effectiveness.

APPENDIX A

HOPPING ROTOCHUTE PROTOTYPE FABRICATION

The Hopping Rotochute prototype consists of many different components which were fabricated and/or purchased off-the-shelf. This appendix briefly outlines the procedures used to create the fabricated parts as well as the assembly process. The technical drawings of the fabricated components are given in Appendix B.

To build the main body of the Hopping Rotochute, a large block of EPP foam was first cut into a hemispherical shape with a radius of 11.43 cm using a specifically designed hot-wire cutter. Once this shape was cut out, another hot-wire cutter was used to trim the core to the desired height of 3.2 cm and an outside diameter of 12.7 cm (see Figure B.1). A hand held hot-wire cutter was then used to cut out an inner section of the core to accommodate the transmission mount, the battery, and finger clearance. The hand held wire-cutter was also used to cut small grooves on the bottom of the core to allow the cage's longitudinal carbon fiber strip to become flush with the bottom side of the core. The two "U" shaped fabricated mounting brackets, each consisting of a mounting bracket plate and two pins (see Figures B.2 and B.3), were adhered to this inside section of the core using LOCTITE Quick Set epoxy. Once the epoxy dried, three 0.5 × 3 × 800 mm longitudinal carbon fiber strips were adhered to the bottom of the core and trimmed to the appropriate length. The two 0.5 × 3 × 775 mm latitudinal carbon fiber strips were also cut to length and attached to the longitudinal carbon fiber strips by wrapping thread around each intersection and applying cyanoacrylate (CA) adhesive. The top of the longitudinal carbon fiber strips were secured to a star piece (see Figure B.4) fabricated

from aluminum shim stock of 0.64 mm thickness. A piece of 6.35 mm (¼ in) polyurethane foam was finally adhered to the bottom of the EPP core using 3M Super 77 spray adhesive and trimmed using a scissors.

The rotor system, transmission, and motor from an Air Hogs Reflex micro helicopter were incorporated into the design of the Hopping Rotochute prototype. In order to use this propulsion system, the Reflex's fuselage was first carefully cut into two halves and the components were extracted by simply unscrewing them from the landing gear and cutting off the associated electronics. The lower rotor shaft was extended using a fabricated hollow aluminum rod (see Figure B.5) while the upper shaft was lengthened by replacing the original 2 mm diameter carbon fiber rod with one 12.7 cm long. The transmission housing was attached to a fabricated transmission mount (see Figure B.6) using the same small screws supplied with the Reflex micro helicopter. The transmission mount was constructed out of 0.635 mm aluminum shim stock which was cut and drilled to provide clearance for the transmission housing, servo, and mounting bracket pins. The internal mass assembly was created by adhering the nylon pinion to one end of the internal mass bar (see Figure B.7) and securing the internal mass housing (see Figure B.8) at the other. Before the pinion was adhered to the internal mass bar, it was first drilled out to fit over the upper section of the transmission housing with enough clearance to provide smooth rotation while avoiding binding. A snap ring was placed on the upper section of the transmission housing to prevent the internal mass assembly from sliding off. The electronic speed controller and receiver were adhered to the motor mount using CA adhesive.

To assemble the Hopping Rotochute prototype, the battery is first fitted inside the designated pocket within the core of the body. The propulsion system is then routed inside the cage and the transmission mount is slid between the mounting brackets until the pins of the mounting bracket snap into the holes of the transmission mount. This simple method allows easy assembly/disassembly of the two systems while keeping the battery intact.

APPENDIX B

HOPPING ROTOCHUTE COMPONENT DRAWINGS

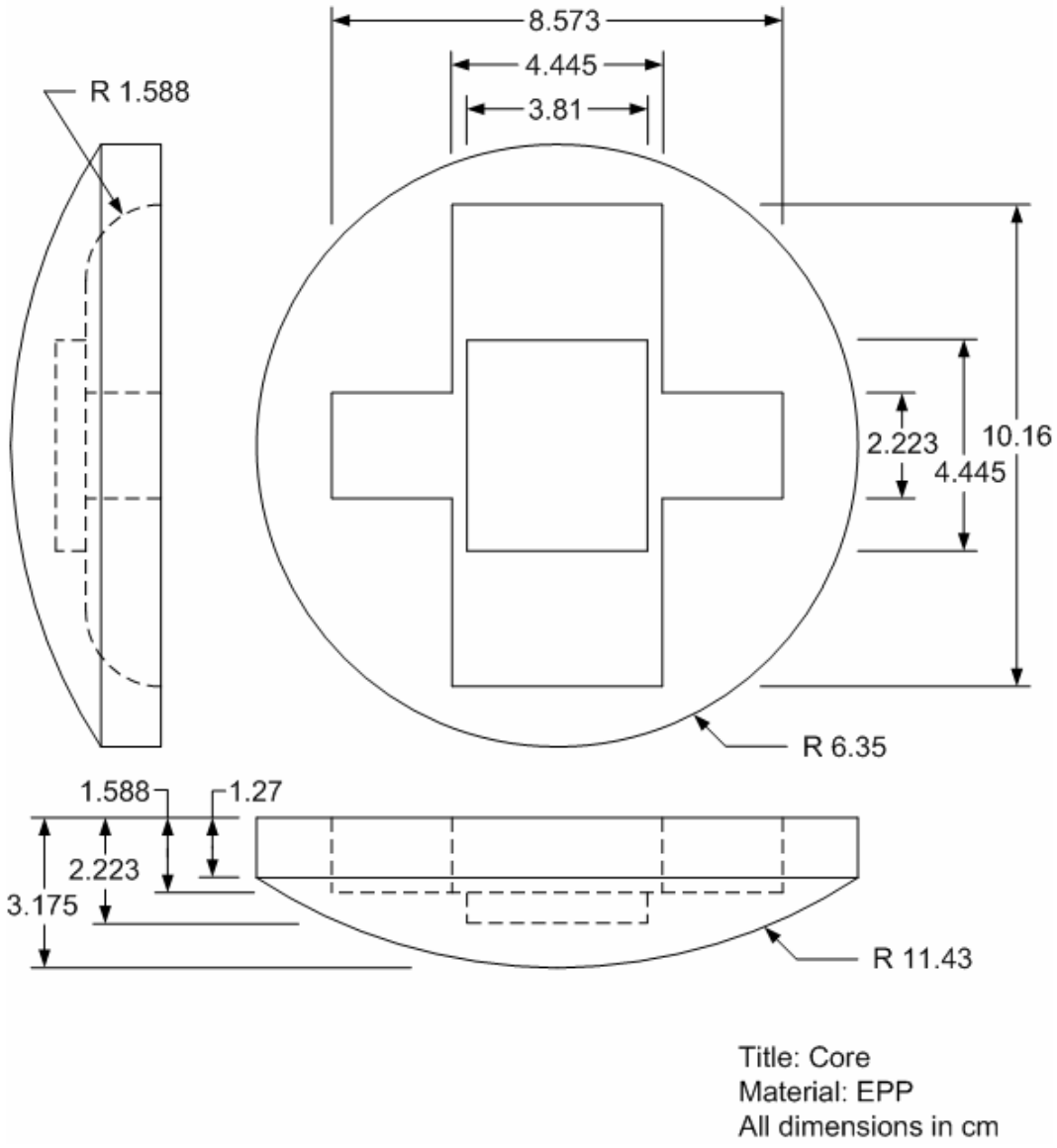

Figure B.1: Main body core

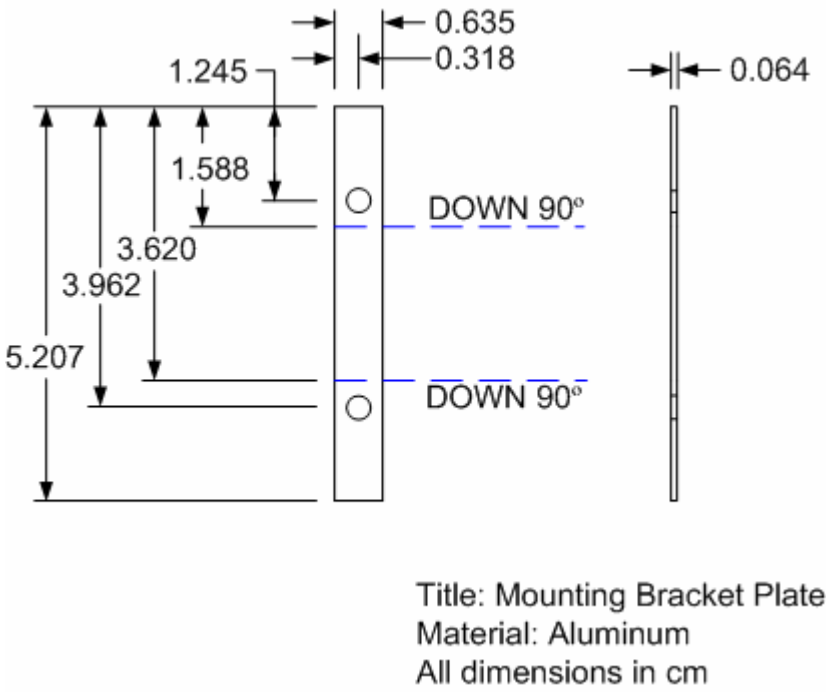

Figure B.2: Mounting bracket plate

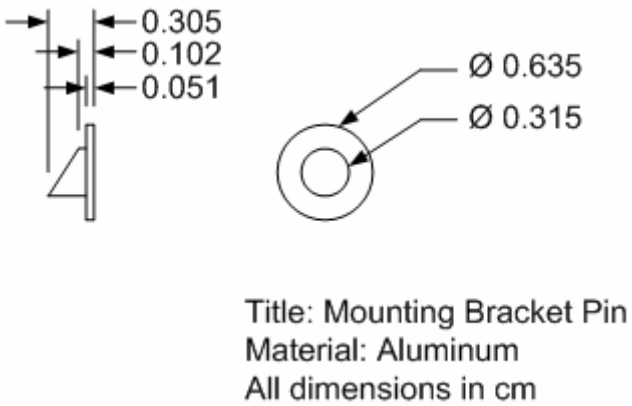

Figure B.3: Mounting bracket pin

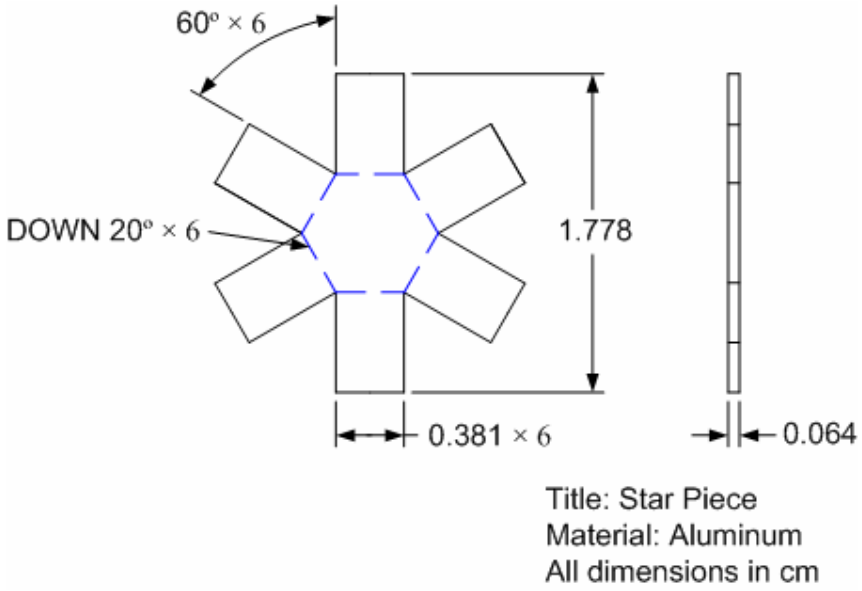

Figure B.4: Star piece

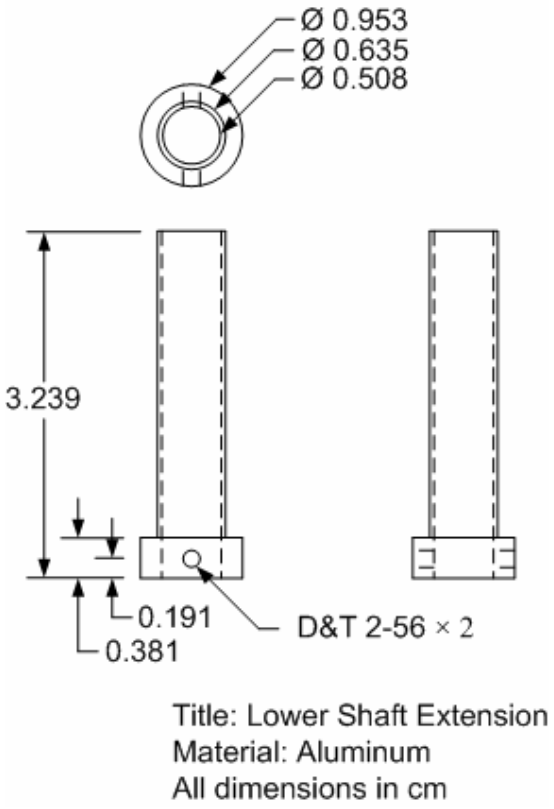

Figure B.5: Lower shaft extension

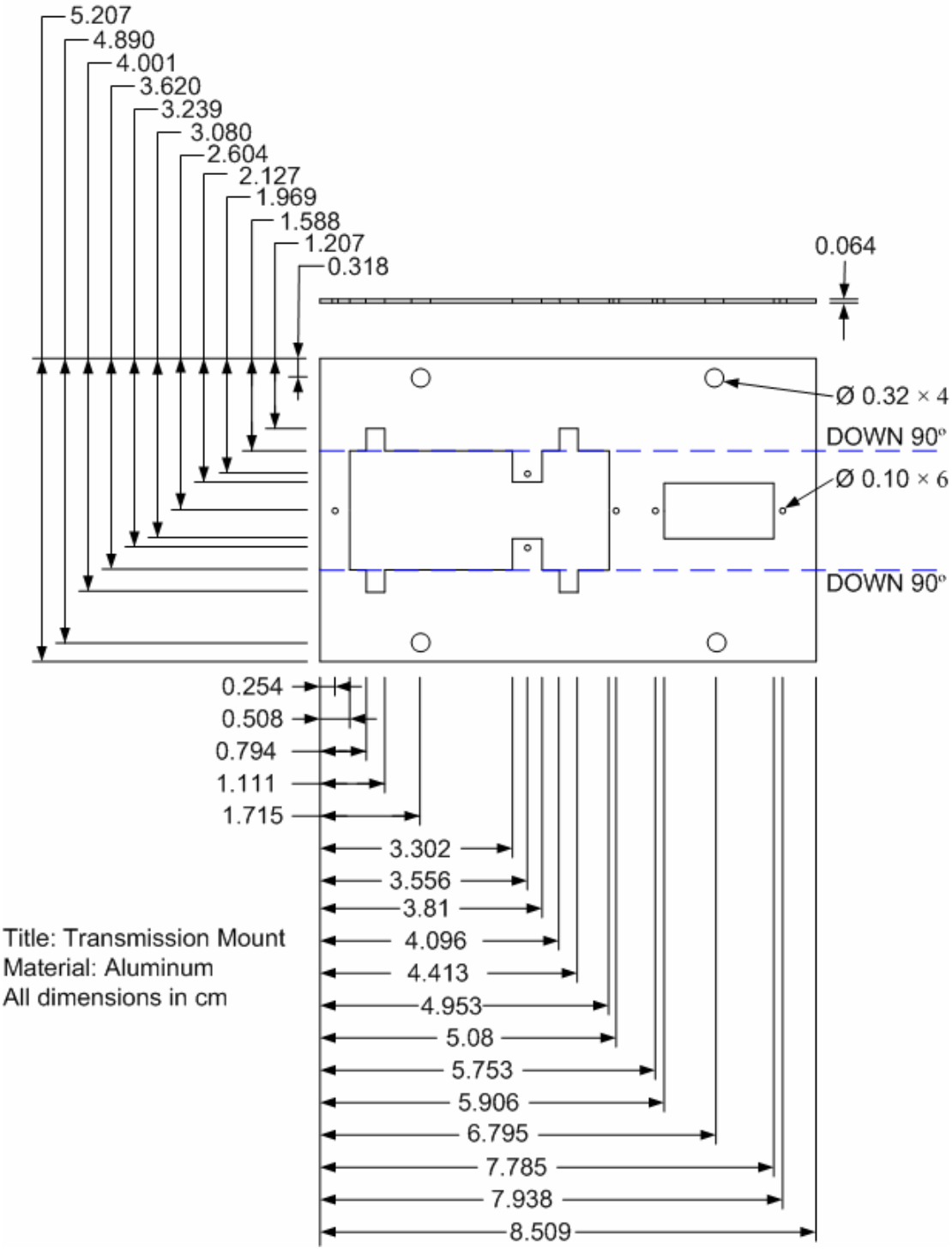

Figure B.6: Transmission mount

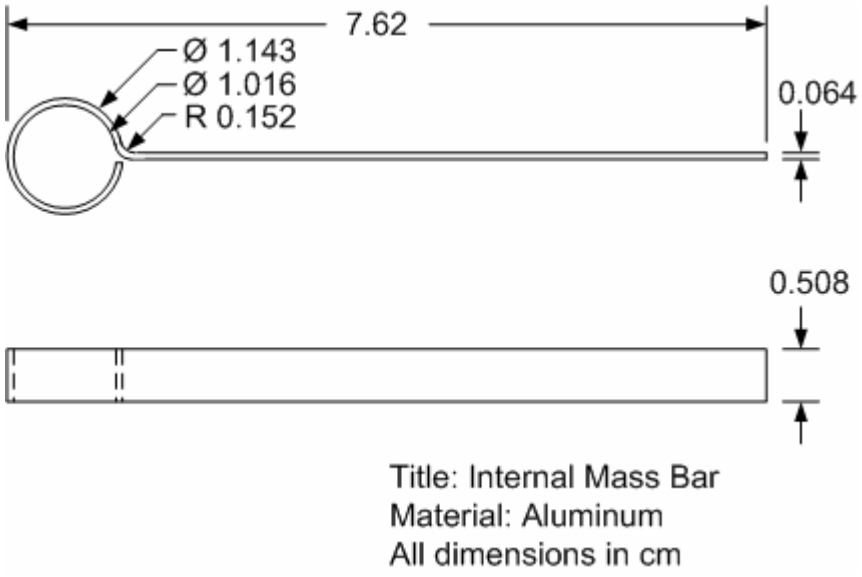

Figure B.7: Internal mass bar

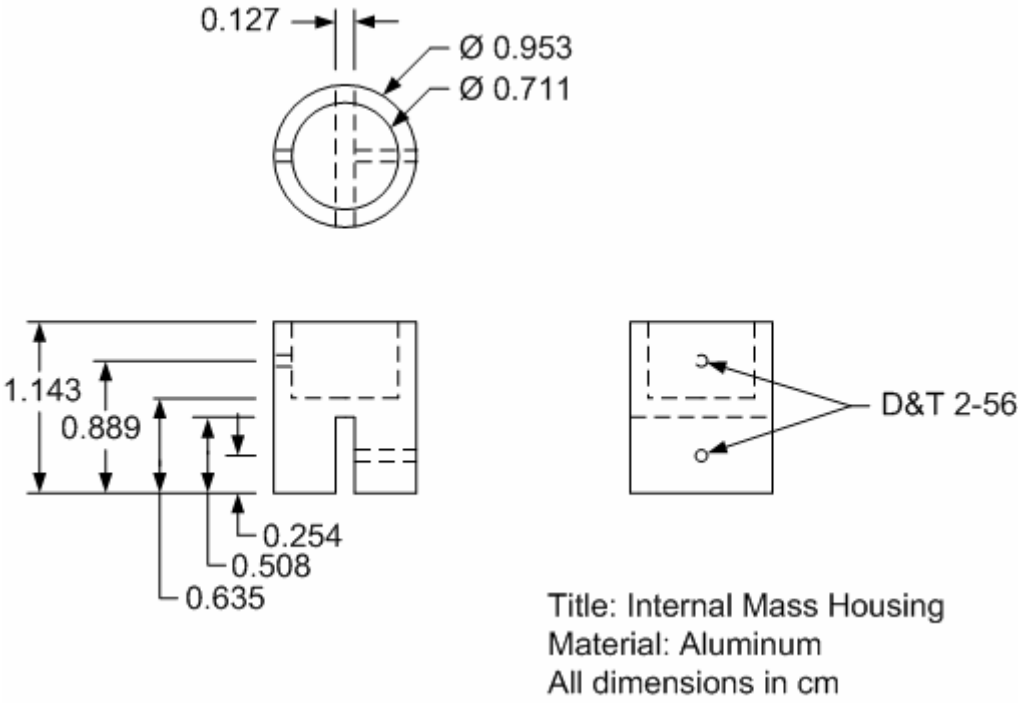

Figure B.8: Internal mass housing

REFERENCES

[1] Exponent Inc. "MARCbot." Exponent Inc. http://www.exponent.com/marcbot_product/ (accessed December 3, 2008).

[2] Recon Robotics. "Recon Scout." Recon Robotics. http://www.recon-scout.com/products/index.cfm (accessed December 4, 2008).

[3] Mishkin, A. H., Morrison, J. C., Nguyen, T. T., Stone, H. W., Cooper, B. K., and Wilcox, B. H. "Experiences with Operations and Autonomy of the Mars Pathfinder Microrover." in *Proceedings of the IEEE Aerospace Conference*, vol. 2, March 1998, pp. 337 – 351.

[4] Estier, T., Crausaz, Y., Merminod, B., Lauria, M., Piguet, R., and Siegwart, R. "An Innovative Space Rover with Extended Climbing Abilities." in *Proceedings of the ASCE Space and Robotics Conference*, 2000, pp. 333 – 339.

[5] iRobot Corporation. "iRobot PackBot." iRobot Corporation. http://www.irobot.com/sp.cfm?pageid=171 (accessed December 2, 2008).

[6] Yamauchi, B. "Daredevil: Ultra-Wideband Radar Sensing for Small UGVs." in *Proceedings of the SPIE Unmanned Systems Technology IX*, vol. 6561, April 2007.

[7] Foster-Miller Inc. – QinetiQ North America. "Products and services." Foster-Miller Inc. http://www.foster-miller.com/lemming.htm (accessed December 3, 2008).

[8] Boston Dynamics. "LittleDog." Boston Dynamics. http://www.bostondynamics.com/content/sec.php?section=LittleDog (accessed December 3, 2008).

[9] Greenmeier, L. "DARPA Pushes Machine Learning with Legged LittleDog Robot." *Scientific American*, Apr. 15, 2008.

[10] Saranli, U., Buehler, M., and Koditschek, D. "RHex – A Simple and Highly Mobile Hexapod Robot." *The International Journal of Robotics Research*, vol. 20, no. 7 (2001): pp. 616 – 631.

[11] Altendorfer, R., Moore, N., Komsuoglu, H., Buehler, M., Brown, H. B., McMordie, D., Saranli, U., Full, R., and Koditschek, D. E. "RHex: A Biologically Inspired Hexapod Runner." *Autonomous Robots*, vol. 11, (2001): pp. 201 – 213.

[12] Quinn, R. D., Offi, J. T., Kingsley, D. A., Ritzmann, R. E. "Improved Mobility through Abstracted Biological Principles." in *Proceedings of the IEEE/RSJ International Conference on Intelligent Robots and Systems*, Lausanne, Switzerland, October 2002, pp. 2652 – 2657.

[13] Grasmeyer, J. and Keennon, M. "Development of the Black Widow Micro Air Vehicle." in *Proceedings of the 39th AIAA Aerospace Sciences Meeting and Exhibit*, no. AIAA-2001-0127, Reno, NV, 2001.

[14] Defense Update. "Black Widow Micro UAV." Defense Update. http://www.defense-update.com/products/b/black-widow.htm (accessed December 4, 2008).

[15] Defense Update. "Class I UAVs." Defense Update. http://www.defense-update.com/products/h/honeywell-mav.htm (accessed December 4, 2008).

[16] Adaptive Flight. "Hornet UAS." Adaptive Flight. http://www.adaptiveflight.com (accessed December 4, 2008).

[17] Pornsin-Sirirak, T. N., Tai, Y., Ho, C., and Keennon, M. "Microbat: A Palm-Sized Electrically Powered Ornithopter." in *Proceedings of the NASA/JPL Workshop on Biomorphic Robotics,* 2001.

[18] Raibert, M. H. "Legged Robots." *Communications of the ACM*, vol. 29, no. 6 (1986): pp. 499 – 514.

[19] Iida, F., Dravid, R., and Paul, C. "Design and Control of a Pendulum Driven Hopping Robot." in *Proceedings of the IEEE/RSJ International Conference on Intelligent Robots and Systems*, Lausanne, Switzerland, October 2002, pp. 2141 – 2146.

[20] Brown, B. and Zeglin, G. "The Bow Leg Hopping Robot." in *Proceedings of the IEEE International Conference on Robotics and Automation*, Leuven, Belgium, May 1998, pp. 781 – 786.

[21] Okubo, H., Nakano, E., and Handa, M. "Design of a Jumping Machine using Self-energizing Spring." in *Proceedings of the IEEE/RSJ International Conference on Intelligent Robots and Systems*, vol. 1, November 1996, pp. 186 – 191.

[22] Fiorini, P. and Burdick, J. "The Development of Hopping Capabilities for Small Robots." *Autonomous Robots,* vol. 14, no. 2-3 (2003): pp. 239 – 254.

[23] Center for Biologically Inspired Robotics Research. "Mini-Whegs™ Robots." Case Western Reserve University. http://biorobots.cwru.edu/projects/whegs/miniwhegs.html (accessed March 23, 2009).

[24] Morrey, J. M., Lambrecht, B., Horchler, A. D., Ritzmann, R. E., and Quinn R. D. "Highly Mobile and Robust Small Quadruped Robots." in *Proceedings of the IEEE/RSJ International Conference on Intelligent Robots and Systems*, vol. 1, Las Vegas, NV, October 2003, pp. 82 – 87.

[25] Horchler, A. D., Quinn, R. D., Lambrecht, B., and Morrey, J. M. "Highly Mobile Robots that Run and Jump." U.S. Patent 7 249 640 B2, July 31, 2007.

[26] Center for Distributed Robotics. "UMN Scout." University of Minnesota. http://distrob.cs.umn.edu/scout.php (accessed March 23, 2009).

[27] Stoeter, S. A., Rybski, P. E., Gini, M., and Papanikolopoulos, N. "Autonomous Stair-Hopping with Scout Robots." in *Proceedings of the IEEE/RSJ International Conference on Intelligent Robots and Systems*, vol. 1, Lausanne, Switzerland, October 2002, pp. 721 – 726.

[28] Drenner, A., Burt, I., Dahlin, T., Kratochvil, B., McMillen, C., Nelson, B., Papanikolopoulos, N., Rybski, P., Stubbs, K., Waletzko, D., and Yesin, K. "Mobility Enhancements to the Scout Robot Platform." in *Proceedings of the IEEE International Conference on Robotics and Automation*, Washington D.C., May 2002, pp. 1069 – 1074.

[29] Armour, R., Paskins, K., Bowyer, A., Vincent, J., and Megill, W. "Jumping Robots: A Biomimetic Solution to Locomotion across Rough Terrain." *Bioinspiration and Biomimetics*, vol. 2, (2007): pp. 65 – 82.

[30] Sugiyama, Y. and Hirai, S. “Crawling and Jumping by a Deformable Robot.” *The International Journal of Robotics Research*, vol. 25, no. 5-6 (May-June 2006): pp. 603 – 620.

[31] Weiss, P. “Hop…Hop…Hopbots!: Designers of Small, Mobile Robots takes Cues from Grasshoppers and Frogs.” *Science News*, vol. 159, no. 6 (2001): pp. 88 – 90.

[32] Spletzer, B. L., Fischer, G. J., Marron, L. C., Martinez, M. A., Kuehl, M. A., and Feddema, J. T. “Hopping Robot.” U.S. Patent 6 247 546 B1, June 19, 2001.

[33] Kikuchi, F., Ota, Y., and Hirose, S. “Basic Performance Experiments for Jumping Quadruped.” in *Proceedings of the IEEE/RSJ International Conference on Intelligent Robots and Systems*, Las Vegas, NV, October 2003, pp. 3378 – 3383.

[34] Tanaka, T. and Hirose, S. “Development of Leg-Wheel Hybrid Quadruped – Airhopper.” in *Proceedings of the IEEE/RSJ International Conference on Intelligent Robots and Systems*, Nice, France, September 2008, pp. 3890 – 3895.

[35] Hayashi, R. and Tsujio, S. “High-Performance Jumping Movements by Pendulum-Type Jumping Machines.” in *Proceedings of the 2001 IEEE/RSJ International Conference on Robots and Systems*, Maui, HI, November 2001, pp. 722 – 727.

[36] Bermes, C., Leutenegger, S., Bouabdallah, S., Schafroth, D., and Siegwart, R. “New Design of the Steering Mechanism for a Mini Coaxial Helicopter.” in *Proceedings of the IEEE/RSJ International Conference on Intelligent Robots and Systems*, Nice, France, September 2008, pp. 1236 – 1241.

[37] Bouabdallah, S., Caprari, G., and Siegwart, R. “Design and Control of an Indoor Coaxial Helicopter.” in *Proceedings of the IEEE International Conference Intelligent Robots and Systems*, Beijing, China, 2006.

[38] Bermes, C., Sartori, K., Schafroth, D., Bouabdallah, S., and Siegwart, R. “Control of a Coaxial Helicopter with Center of Gravity Steering.” in *Proceedings of the International Conference on Simulation, Modeling, and Programming for Autonomous Robot*, Venice, Italy, November 2008, pp. 492 – 500.

[39] Wang, W., Song, G., Nonami, K., Hirata, M., and Miyazawa, O. “Autonomous Control for Micro-Flying Robot and Small Wireless Helicopter X.R.B.” in *Proceedings of the IEEE International Conference on Intelligent Robots and Systems*, Beijing, China, 2006.

[40] Rogers, J. and Costello, M. "Control Authority of a Projectile Equipped with a Controllable Internal Translating Mass." *Journal of Guidance, Control, and Dynamics*, vol. 31, no. 5 (September – October 2008): pp. 1323 – 1333.

[41] Beyer, E. and Costello, M. "Design and Testing of a Hybrid Micro Vehicle – The Hopping Rotochute." *IEEE/ASME Transactions on Mechatronics*, submitted for publication.

[42] Leishman, J. G. *Principles of Helicopter Aerodynamics*. New York, NY: Cambridge University Press, 2006.

[43] Prouty, R. W. *Helicopter Performance, Stability, and Control*. Boston, MA: PWS Engineering, 1986.

[44] Johnson, W. *Helicopter Theory*. Princeton, NJ: Princeton University Press, 1980.

[45] Gessow, A. and Myers, G. C. *Aerodynamics of the Helicopter*. New York, NY: F. Unger Publishing Company, 1967.

[46] Stepniewski, W. Z. and Keys, C. N. *Rotary-Wing Aerodynamics*. New York, NY: Dover Publications, 1984.

[47] Srinivasan, G. R. and Baeder, J. D. "TURNS: A Free-Wake Euler-Navier-Stokes Numerical Method for Helicopter Rotors." *AIAA Journal*, vol. 31, no. 5 (1993): pp. 959 – 962.

[48] Chan, W. M., Meakin, R. L., and Potsdam, M. A. "CHSSSI Software for Geometrically Complex Unsteady Aerodynamic Applications." in *39th AIAA Aerospace Sciences Meeting and Exhibit*, no. AIAA-2001-0539, Reno, NV, January 2001.

[49] Roberts, T. W. and Murman, E. M. "Solution Method for a Hovering Helicopter Rotor using the Euler Equations." in *23rd AIAA Aerospace Sciences Meeting*, no. AIAA-85-0436, Reno, NV, January 1985.

[50] Sankar, L. N., Wake, B. E., and Lekoudis, S. G. "Solution of the Unsteady Euler Equations for Fixed and Rotor Wing Configurations." *Journal of Aircraft*, vol. 23, no. 4 (1986): pp. 283 – 289.

[51] Conlisk, A. T. "Modern Helicopter Rotor Aerodynamics." *Progress in Aerospace Sciences*, vol. 37, no. 5 (July 2001): pp. 419 – 476.

[52] Knight, M. and Hefner, R. A. "Static Thrust of the Lifting Airscrew." NACA-TN-626, 1937.

[53] Phelps, A. E. and Mineck, R. E. "Aerodynamic Characteristics of a Counter-Rotating, Coaxial, Hingeless, Rotor Helicopter Model with Auxiliary Propulsion." NASA-TM-78705, May 1978.

[54] Felker, F. P, "Performance and Loads Data from a Wind Tunnel Test of a Full-Scale, Coaxial, Hingeless Rotor Helicopter." NASA-TM-81329, October 1981.

[55] Coleman, C. P. "A Survey of Theoretical and Experimental Coaxial Rotor Aerodynamic Research." NASA Technical Paper 3675, 1997.

[56] Koratkar, N. A. and Chopra, I. "Wind Tunnel Testing of a Mach-Scaled Rotor Model with Trailing-Edge Flaps." *Smart Materials and Structures*, vol. 10, (2001): pp. 1 – 14.

[57] Young, L. A., Aiken, E. W., Johnson, J. L., Demblewski, R., Andrews, J., and Klem, J. "New Concepts and Perspectives on Micro-Rotorcraft and Small Autonomous Rotary-Wing Vehicles." in *20th AIAA Applied Aerodynamics Conference*, no. AIAA-2002-2816, St. Louis, MO, June 2002.

[58] Bohorquez, F. and Pines, D. "Hover Performance of Rotor Blades at Low Reynolds Numbers for Rotary Wing Micro Air Vehicles." in *2nd AIAA "Unmanned Unlimited" Systems, Technologies, and Operations Meeting*, no. AIAA-2003-6655, San Diego, CA, September 2003.

[59] Beyer, E. and Costello, M. "Measured and Simulated Motion of a Hopping Rotochute." *Journal of Guidance, Control, and Dynamics*, accepted for publication, 2009.

[60] Etkin, B. *Dynamics of Atmospheric Flight*. New York, NY: Wiley, 1972.

[61] Etkin, B. and Reid, L. D. *Dynamics of Flight: Stability and Control*. 3rd ed. New York, NY: Wiley, 1995.

[62] Stengel, R. F. *Flight Dynamics*. Princeton, NJ: Princeton University Press, 2004.

[63] Cook, M. V. *Flight Dynamics Principles*. London: Arnold, 1997.

[64] Zipfel, P. H. *Modeling and Simulation of Aerospace Vehicle Dynamics*. Reston, VA: American Institute of Aeronautics and Astronautics, 2000.

[65] Phillips, W. F. *Mechanics of Flight*. Hoboken, NJ: Wiley, 2004.

[66] Hull, D. G. *Fundamentals of Airplane Flight Mechanics*. Berlin: Springer, 2007.

[67] Schmidt, L. V. *Introduction to Aircraft Flight Dynamics*. Reston, VA: American Institute of Aeronautics and Astronautics, 1998.

[68] Padfield, G. D. *Helicopter Flight Dynamics: The Theory and Application of Flying Qualities and Simulation Modeling*. Washington, DC: American Institute of Aeronautics and Astronautics, 1996.

[69] Saunders, G. H. *Dynamics of Helicopter Flight*. New York, NY: Wiley, 1975.

[70] Bramwell, A. R. S. *Helicopter Dynamics*. New York, NY: Wiley, 1976.

[71] Payne, P. R. *Helicopter Dynamics and Aerodynamics*. New York, NY: Macmillan, 1959.

[72] Beyer, E. and Costello, M. "Flight Dynamics and Control Authority of Flap-Controlled Open Boxes." *Journal of Guidance, Control, and Dynamics*, vol. 30, no. 3 (May-June 2007): pp. 827 – 834.

[73] Slegers, N., Beyer, E., and Costello, M. "Use of Variable Incidence Angle for Glide Slope Control of Autonomous Parafoils." *Journal of Guidance, Control, and Dynamics*, vol. 31, no. 3 (May-June 2008): pp. 585 – 596.

[74] Chandgadkar, S., Costello, M., Dano, B., Liburdy, J., and Pence, D. "Performance of a Smart Direct Fire Projectile using a Ram Air Control Mechanism." *Journal of Dynamic Systems, Measurement, and Control*, vol. 124, no. 4 (December 2002): pp. 606 – 612.

[75] Goyal, S., Pinson, E., and Sinden, F. "Simulation of Dynamics of Interacting Rigid Bodies Including Friction I: General Problem and Contact Model." *Engineering with Computers*, vol. 10, (1994): pp. 162 – 174.

[76] Goyal, S., Pinson, E., and Sinden, F. "Simulation of Dynamics of Interacting Rigid Bodies Including Friction II: System Design and Implementation." *Engineering with Computers*, vol. 10, (1994): pp. 175-195.

[77] Routh, E. J. *Dynamics of a System of Rigid Bodies*. 7th ed. New York, NY: Dover, 1960.

[78] Goldsmith, W. *Impact: The Theory and Physical Behavior of Colliding Solids*. London, UK: Edward Arnold, 1960.

[79] Ingleton, A. W. "A Problem in Linear Inequalities." in *Proceedings of the London Mathematical Society*, vol. 3, no. 16, 1966, pp. 516 – 536.

[80] Cottle, R. W. "On a Problem in Linear Inequalities." *Journal of the London Mathematical Society*, vol. 43, (1968): pp. 378 – 384.

[81] Lotstedt, P. "Numerical Solution of the Time-Dependent Contact and Friction Problems in Rigid Body Mechanics." *SIAM Journal of Scientific Statistical Computing*, vol. 5, no. 2 (June 1984): pp. 370 – 393.

[82] Keller, J. B. "Impact with Friction." *Journal of Applied Mechanics*, vol. 53, (1986): pp. 1 – 4.

[83] Wang, Y. "Dynamic Analysis and Simulation of Mechanical Systems with Intermittent Constraints." PhD Thesis, Carnegie Mellon University, Pittsburg, PA, May 1989.

[84] Baraff, D. "Analytical Methods for Dynamic Simulation of Non-Penetrating Rigid Bodies." *Computer Graphics*, vol. 23, no. 3 (July 1989): pp. 223 – 232.

[85] Mirtich, B. and Canny, J. "Impulse-Based Simulation of Rigid Bodies." in *Proceedings of the 1995 Symposium of Interactive 3D Graphics*, Monterey, CA, 1995, pp. 181 – 189.

[86] Trinkle, J. C. and Pang, J. "Dynamic Multi-Rigid-Body Systems with Concurrent Distributed Contacts." in *Proceedings of the 1997 IEEE International Conference on Robotics and Automation*, vol. 3, Albuquerque, NM, April 1997, pp. 2276 – 2281.

[87] Joukhadar, A. and Laugier, C. "Dynamic Modeling of Rigid and Deformable Objects for Robotic Tasks: Motions, Deformations, and Collisions." in *Proceedings of the International Conference ORIA*, Marseille, France, December 1994.

[88] Joukhadar, A. and Laugier, C. "Dynamic Modeling and its Robotic Applications (The RobotΦ System)." in *Proceedings of the 1995 IEEE International Conference on Robotics and Automation*, vol. 3, May 1995, pp. 2684 – 2689.

[89] Marhefka, W. and Orin, D. E. "Simulation of Contact using a Nonlinear Damping Model." in *Proceedings of the 1996 IEEE International Conference on Robotics and Automation*, vol. 2, April 1996, pp. 1662 – 1668.

[90] LaFarge, R. A. and Lewis, C. "Contact Force Modeling between Non-Convex Objects using a Nonlinear Damping Model." in *Proceedings of the International ADAMS User Conference*, Ann Arbor, MI, 1998.

[91] Tenaglia, C. A., Orin, D. E., LaFarge, R. A., and Lewis, C. "Toward Development of a Generalized Contact Algorithm for Polyhedral Objects." in *Proceedings of the 1999 IEEE International Conference on Robotics and Automation*, vol. 4, Detroit, MI, May 1999, pp. 2887 – 2892.

[92] VICON. "Vicon Products." VICON Motion Systems Limited. http://www.vicon.com/products/ (accessed January 25, 2009).

[93] Qualisys. "Optical Motion Capture – Accurate Tracking of any Kind of Motion." Qualisys Motion Capture Systems. http://www.qualisys.com/ (accessed April 1, 2009).

[94] Motion Analysis. "Products." Motion Analysis Corporation. http://www.motion analysis.com/html/products.html (accessed April 1, 2009).

[95] VICON Motion Systems Limited. "VICON System Reference." Oxford, UK, 2007.

[96] Kyle, J. and Costello, M. "Comparison of Measured and Simulated Motion of a Scaled Dragline Excavation System." *Mathematical and Computer Modelling*, vol. 44, no. 9-10 (2006): pp. 816 – 833.

[97] Zordan, V., Macchietto, A., Medin, J., Soriano, M., Wu, C., Metoyer, R., and Rose, R. "Anticipation from Example." in *Proceedings of the 2007 ACM Symposium on Virtual Reality Software and Technology*, Newport Beach, CA, 2007, pp. 81 – 84.

[98] Egret, C. I., Vincent, O., Weber, J., Dujardin, F. H., and Chollet, D. "Analysis of 3D Kinematics Concerning Three Different Clubs in Golf Swing." *International Journal of Sports Medicine*, vol. 24, no. 6 (2003): pp. 465 – 469.

[99] Frank, A., McGrew, J. S., Valenti, M., Levine, D., and How, J. "Hover, Transition, and Level Flight Control Design for a Single-Propeller Indoor Airplane." in *Proceedings of the AIAA Guidance, Navigation, and Control Conference and Exhibit*, Myrtle Beach, SC, August 2007.

[100] How, J. P., Bethke, B., Frank, A., Dale, D., and Vian, J. "Real-Time Indoor Autonomous Vehicle Test Environment." *IEEE Control Systems Magazine*, vol. 28, no. 2 (April 2008): pp. 51 – 61.

[101] How, J. P., Teo, J., and Michini, B. "Adaptive Flight Control Experiments using RAVEN." in *Proceedings of the 14th Yale Workshop on Adaptive and Learning Systems*, New Haven, CT, June 2008, pp. 205 – 210.

[102] Beyer, E. and Costello, M. "Performance of a Hopping Rotochute." *International Journal of Micro Air Vehicles*, accepted for publication, 2009.

VITA

ERIC W. BEYER

BEYER was born in Silverton, Oregon and attended public schools in Mount Angel, Oregon. He received a B.S. and an M.S. in Mechanical Engineering from Oregon State University, Corvallis, Oregon in 2003 and 2006 respectively. In Fall of 2006, he entered the School of Aerospace Engineering at the Georgia Institute of Technology to pursue a Ph.D. degree. His interests include the design, dynamics, and controls of unique micro air vehicles.